

Biomimetic, Polymeric Transistor-based Biosensor Technology

Jim Chih-Min Cheng



Electrical Engineering and Computer Sciences
University of California at Berkeley

Technical Report No. UCB/EECS-2009-171

<http://www.eecs.berkeley.edu/Pubs/TechRpts/2009/EECS-2009-171.html>

December 15, 2009

Copyright © 2009, by the author(s).
All rights reserved.

Permission to make digital or hard copies of all or part of this work for personal or classroom use is granted without fee provided that copies are not made or distributed for profit or commercial advantage and that copies bear this notice and the full citation on the first page. To copy otherwise, to republish, to post on servers or to redistribute to lists, requires prior specific permission.

Biomimetic, Polymeric Transistor-Based Biosensor Technology

by

Jim Chih-Min Cheng

A dissertation submitted in partial satisfaction of the

requirements for the degree of

Doctor of Philosophy

in

Engineering-Electrical Engineering and Computer Sciences

in the

Graduate Division

of the

University of California, Berkeley

Committee in charge:

Professor Albert P. Pisano, Chair

Professor Ming C. Wu

Professor Liwei Lin

Fall 2009

Biomimetic, Polymeric Transistor-Based Biosensor Technology

Copyright © 2009
by
Jim Chih-Min Cheng

Abstract

Biomimetic, Polymeric Transistor-Based Biosensor Technology

by

Jim Chih-Min Cheng

Doctor of Philosophy in Engineering-Electrical Engineering and Computer Sciences

University of California, Berkeley

Professor Albert P. Pisano, Chair

The goal of this research is the creation of robust, flexible, polymer sensors and circuits fabricated partially from the low cost biopolymer, chitosan, the deacetylated form of chitin which is the second most abundant polysaccharide in nature. Chitin is found in crustaceans, insects, bacteria and fungi. The sensors will detect diatomic gases and DNA to more complex macro molecules (e.g. exotoxins) in a fluidic or dry environment. Polymer-nanoparticle (e.g. Ge) hybrid films allow for development of robust polymer thin-film transistors and, with optimization of the hybrid film, sensitive photodetectors. These transistors may be developed into gas or chemical sensors through functionalization of the polymer active layer or dielectric with proteins specific to a target analyte. This technology will enable the development of integrated polymer sensors and electronics which are low-cost, robust and highly versatile due to the replacement of semiconductor, dielectric and possibly metal layers with polymers and minimal thermal budget.

To my parents and sister,
who have continuously given me support and inspired me
to strive to new heights and never give up.

Contents

List of Figures	iv
List of Tables	ix
1 Introduction	1
1.1 Surface Microfluidic Systems	1
1.2 Current State-of-the-Art Assays	2
1.2.1 Impact of IPSMS	4
1.3 Polymer-Nanoparticle Thin-Film Transistor	5
1.4 Current State-of-the-Art	6
1.4.1 Organic Semiconductors	6
1.4.2 Nanoparticle devices	7
1.4.3 Nanocomposite devices	8
1.5 Optical fluorescence sensing	9
1.5.1 Enzyme-Linked ImmunoSorbent Assay (ELISA)	9
1.5.2 Current detection methods	9
1.6 Organization of Thesis	10
2 Chitosan Photolithography	12
2.1 Background	12
2.2 Process	14
2.3 Results and Discussion	16
2.4 Conclusion	24
3 Polymer Nanocomposite	25
3.1 Background	25
3.1.1 Gas Phase Synthesis	26
3.1.2 Chemical Synthesis	27
3.1.3 Supercritical Fluid Synthesis	30
3.2 Germanium Nanoparticle Synthesis	31
3.2.1 Synthesis Method I - Gas Phase Synthesis	32
3.2.2 Synthesis Method II - Batch Chemical Synthesis	37

3.2.3	Initial Synthesis Protocol	39
3.2.4	1-Pentene Protocol	51
3.2.5	ODE post-functionalization protocol	54
3.3	Discussion and Conclusion	61
4	Polymer Nanocomposite Thin-Film Transistor (PNTFT)	64
4.1	Background	64
4.2	Operation of the PNTFT	65
4.3	Thin-Film Transistor Base	68
4.4	Active layer Deposition and Treatment	71
4.5	Discussion and Conclusion	73
5	Future Work	74
	Bibliography	76
A	Immobilization of Enzymes in Chitosan	83
A.1	Introduction	83
A.2	Experiments	84
A.2.1	Chitosan solution preparation	84
A.2.2	Single Layer Fabrication Process	85
A.2.3	Multi- Layer Fabrication Process	86
A.2.4	Sample Imaging and Metrology	87
A.3	Results and Discussion	87
A.3.1	Single layer	87
A.3.2	Multi-layer	88
A.4	Conclusion	89
B	Supplemental Data	90
B.1	Nanoparticle Data	90
B.1.1	X-ray Absorption Spectra (XAS)	90
B.1.2	Post-functionalization TEM	92
B.1.3	UV/VIS spectrum	93
B.1.4	General properties of nanoparticles	93
B.1.5	Cadmium Sulfide (CdS) Nanoparticles in Chitosan	94

List of Figures

1.1	System overview of IPSMS. DNA from the unpurified sample is transported across the BLM by selective transport porins (Preparation-Component 1). Surface electrophoresis is used to transport samples around the chip and to perform separation of DNA into distinct bands (Separation-Component 2). The PNTFT, using optical transduction or electromechanical transduction, measures the analyte concentration or activity level (Detection-Component 3).	2
1.2	Real-time Polymerase Chain Reaction (PCR) analysis system built by Cepheid, Inc.	3
1.3	Agilent 7100 Capillary Electrophoresis System built by Agilent Technologies, Inc.) [1].	4
1.4	The PNTFT and its two modes of operation as a sensor in the IPSMS. Mode 1: Optically Sensitive (PNTFT-OS). Mode 2: Electromechanically Sensitive (PNTFT-EMS).	6
1.5	High resolution cross-section Scanning Electron Microscope (SEM) image of the channel of a lead selenide (PbSe) nanoparticle transistor [2].	7
1.6	Cadmium selenide quantum dots of various diameter fluorescing under UV light [3].	9
1.7	Compact laser-induced fluorescence detector made by Picometrics, Inc. [4]	10
2.1	Characterization of chitosan hydrogel solution. a). Viscosity of chitosan hydrogel solution as the concentration of chitosan is increased. b). pH of chitosan hydrogel solution with varying concentration of chitosan. c). Chitosan hydrogel † solution contact angle on bare silicon and silicon with native oxide. †solvent was 150 mL of 2:1 buffered acetic acid.	13
2.2	Chitosan photolithography process utilizing a PMMA barrier layer for protection against swelling issues. Includes an optional XeF ₂ plasma Si etch for the release of chitosan structures.	15

2.3	Characterization of chitosan thin-films. a) Chitosan spin curves for chitosan concentrations varying between 1 g (0.66 % w/v) to 6 g (4.0 % w/v) dissolved (n = 6) b). Surface roughness (R_a - center-line roughness) of 3 g (2.0 % w/v) chitosan films between spun using spin speeds between 3,000 - 4,000 rpm (n = 3). c). Stress-temperature curve for 6 g (4.0 % w/v) chitosan film ($T = 3.4 \mu\text{m}$), where tensile stress is positive d). SEM image of a cross section of a $2.56 \mu\text{m}$ chitosan film on silicon with native oxide taken with sample at 80° tilt.	17
2.4	Patterning of a double-folded flexure MEMS resonator in chitosan ($T = 2 \mu\text{m}$) to demonstrate high-resolution patterning ability. Images show the resonator structure and magnified views of the comb structure after a) photoresist development, b) anisotropic oxygen ion etching and c) photoresist and PMMA strip. Image d) is a SEM image of the resonator structure at a 50° tilt and some magnified views of the comb structure (Note: structure unreleased).	20
2.5	Photolithographically-patterned chitosan features. a) SEM of matched comb structure at a 50° tilt. b) SEM of $2 \mu\text{m}$ wide lines with $4 \mu\text{m}$ pitch. c) SEM of serpentine spring structures. d) SEM of sawtooth structure. Note: All patterns in a $2 \mu\text{m}$ thick chitosan layer.	22
2.6	FTIR characterization of chitosan before and after processing. a) Normalized Fourier-transform infrared absorption spectrograph for the chitosan film layer before microprocessing. b) Normalized Fourier-transform infrared absorption spectrograph for the chitosan film layer after microprocessing. c) Normalized Fourier-transform infrared absorption spectrographs for the chitosan film layer after XeF_2 release etch. d) Partially released chitosan cantilever on silicon $240 \times 25 \times 2 \mu\text{m}$. Chitosan serves as a sufficient structural material to support itself.	23
3.1	Gas phase synthesis setup employed by DRDC Suffield group in Canada [5].	27
3.2	A typical Schlenk line and flask setup for chemical synthesis of nanoparticles under inert conditions [6].	28
3.3	Phase diagram showing the supercritical fluid (SCF) region [7].	30
3.4	Representative TEM images of Ge NCs with mean diameters of a) $3.1 \pm 0.4 \text{ nm}$, b) $4.0 \pm 0.6 \text{ nm}$, c) $7.0 \pm 1.6 \text{ nm}$, d) $9.7 \pm 2.0 \text{ nm}$, and e) $11.1 \pm 3.6 \text{ nm}$ synthesized at 700°C from 25, 35, 45, 55, and $65 \mu\text{L}$ of tetrapropylgermane per 100 mL of toluene, respectively. [8]	33

3.5	X-ray photoelectron spectroscopy (XPS) spectrum of the 10 nm germanium nanoparticles provided by University of Colorado, deposited onto a test die with silicon and aluminum on the surface. Oxygen plasma was used to etch away the carbon contaminant on the nanoparticles. As can be seen from the spectrum, the germanium 3d peak was split into two with the larger intensity peak at higher binding energy. A high resolution scan of the 3d peak showed that the crystals were 65 % germanium dioxide and 35 % germanium.	34
3.6	Germanium nanoparticles from University of Colorado agglomerated and embedded in a carbon coating.	36
3.7	Reaction kinetics of germanium nanoparticle synthesis	41
3.8	TEM image of the 7 nm germanium nanoparticles synthesized.	42
3.9	SAXS setup at Beamline 7.3.3, ALS, LBNL.	43
3.10	a) SAXS spectrum of the 3 nm germanium nanoparticles b) Peak fit for the 3 nm germanium nanoparticles c) Size distribution of the 3 nm germanium nanoparticles	44
3.11	a) SAXS spectrum of the 7 nm germanium nanoparticles b) Peak fit for the 7 nm germanium nanoparticles c) Size distribution of the 7 nm germanium nanoparticles	45
3.12	WAXS setup at Beamline 7.3.3, ALS, LBNL. The detector situated right above the sample can be seen above right, while the computer set-up used for data collection and interpretation of the raw data can be seen in the image above right.	46
3.13	WAXS (more specifically x-ray diffraction) spectrum of the 7 nm germanium nanoparticles after a) 6 days in ambient and b) after 22 days in ambient. c) WAXS spectrum of oxidized 3 nm germanium nanocrystals. These nanocrystals were kept 22 days in ambient before being oxidized by removal of their ligand coats by ion bombardment (from an ion gun) and oxygen plasma treatment.	47
3.14	XPS survey spectrum of the 7 nm germanium nanoparticles.	48
3.15	High resolution spectrum of the 3d peak of the 7 nm germanium nanoparticles.	49
3.16	Sputter profile of the 7 nm germanium nanoparticles to determine the thickness of the germanium dioxide shell.	50
3.17	TEM image of 8 nm germanium nanoparticles synthesized using 1-pentene.	52
3.18	XPS spectrum of 8 nm germanium nanoparticles synthesized using 1-pentene.	53
3.19	High resolution XPS spectrum of the 3d peak of 8 nm germanium nanoparticles synthesized using 1-pentene.	54

3.20	TEM image of the 5 nm germanium nanoparticles with ODE ligand coat synthesized through new hydrogermylation protocol stored under ambient conditions twelve hours after synthesis.	56
3.21	XPS survey spectrum of 5 nm germanium nanoparticles with ODE ligand coat synthesized through new hydrogermylation protocol stored under N ₂ twelve hours after synthesis.	57
3.22	XPS spectrum of 5 nm germanium nanoparticles with ODE ligand coat synthesized through new hydrogermylation protocol stored under ambient conditions twelve hours after synthesis.	59
3.23	High resolution XPS spectrum of the 3d (above left) and 2p ^{3/2} (above right) peaks of the 5 nm germanium nanoparticles with ODE ligand coat stored under N ₂ twelve hours after synthesis.	61
3.24	High resolution XPS spectrum of the 3d (above left) peak of the 5 nm germanium nanoparticles with ODE ligand coat stored under ambient conditions twelve hours after synthesis. The sputter profile of the nanoparticles for determination of the oxide and ligand coat thickness (above right).	62
4.1	The PNTFT operating as a highly sensitive phototransistor.	65
4.2	Model of the optical setup for the PNTFT sensor integrated into the IPSMS.	66
4.3	A larger view of how the optical detection mechanism is to operate.	67
4.4	The PNTFT operating in an electromechanical mode for highly sensitive detection of specific analytes.	68
4.5	Fabricated TFT base with aluminum source, drain and gate and a silicon carbide dielectric.	69
4.6	Drain current vs Gate bias curves to test just the amorphous silicon carbide dielectric films and the the effect of hydrogen anneals. The leakage up to a 0.5 V bias and 5 V bias was ascertained utilizing transistor bases with source and drain electrodes 64 μm long. The gate length for these tests was 4 μm.	70
4.7	Schematic of TFT test platform with encapsulated germanium nanoparticles deposited as the active layer.	72
A.1	(A) Single layer chitosan-protein patterning, and (B) Multi-layer chitosan-protein patterning.	85
A.2	Patterned chitosan structures with immobilized β-Galactosidase treated with fluorescein di-β-D-Galactosidase (FDG) viewed under a fluorescent microscope.	87

A.3	Multi-layer stack of patterned chitosan with immobilized enzymes in the bottom layer taken at 5x (above left) and closer up at 20x (above right) magnification. Images taken with fluorescent microscope with FITC filter set where bright white fluorescing features are in the bottom layer with immobilized enzymes and the lower intensity, autofluorescing features are in the top layer. Note: Auto-leveling applied to images for purposes of clarity.	88
B.1	XAS (pre-edge, XANES, EXAFS regions for 7 nm Ge particles) . . .	91
B.2	XANES and pre-edge regions for 3 and 7 nm particles. 3 nm particles blue-shifted in plot.	91
B.3	TEM images of the post-functionalization ODE Ge nanoparticles. . .	92
B.4	UV/VIS spectrum of the 7 nm germanium nanoparticles synthesized using the initial protocol.	93
B.5	Approximately 10 nm CdS nanoparticles bonded into a chitosan film.	95

List of Tables

3.1	Chemical Properties of Synthesis Precursors and Solvents [9]	38
3.2	Germanium WAXS peaks	46
3.3	Chemical Properties of 1-Pentene [9]	51
3.4	Photoelectron lines for Ge and chemical shifts due to bonding with other elements [10]	60
A.1	Potential biosensor applications and their respective enzyme/substrate combinations [11]	84
A.2	Selected oxygen plasma etch rates. All etch rates were determined by measuring film thicknesses before and after a 30 sec etch.	86
B.1	General size, area and volume properties of nanoparticles. Assumption of atomic diameter of 5Å.	94

Acknowledgments

I would first of all like to express my sincerest appreciation and gratitude for the guidance and support given by my research advisor, Professor Albert P. Pisano. It has been a long, arduous trek through the jungles of UC system, mountainous LBNL and desertous South Bay (including our junior institutional cousin called Stanford), in search of the treasure called Doctorate of Philosophy. I was allowed to be captain of the expedition, though without Al as my stalwart and trusty navigator, I would never have been able to make it to this point. With beginnings in signal processing, I was given the opportunity to explore MEMS/NEMS, chemistry, materials and biology during my time at Berkeley. Thank you Al for providing me the flexibility and wisdom to go where many electrical engineers have not gone before.

Next, my thanks goes out to Thomas (Trey) H. Cauley III, mechanical engineer extraordinaire and research partner on the Integrated Polymeric Surface Microfluidic System (IPSMS) project. I am privileged to not only call him a labmate but also one of my best friends and together we have swept away many of the barriers between electrical and mechanical engineering and biology. From the initial trips down to South Bay to check out equipment for the Biomimetic Infrared Nanosystems (BIRN) project to the long nights of proposal writing for IPSMS to sharing a desk at the end of this wild ride through the PhD due to renovations to the lab, thanks for working alongside with me and looking forward to future adventures once we are done here at Cal.

In addition, I would like to thank Steven K. Volkman, chemist, friend and nanoparticle guru. Friends from the Electrical Engineering Graduate Student Association, we have had lots of fun both in and out of lab during these past several years. Whether it be our long, informative discussions (to which I thank Naomi for her utmost patience on several occasions waiting for her husband and I to finish our winding discussions) or fruitful imaging sessions, thanks for all your help and wish you all the luck in your future research.

Helen S. Kim - grant administrator, “the real boss” and master chef. A very strict banker, but also one of the nicest people I know. From formatting and checking our proposals to organizing the wonderful parties in the lab, Helen has made life in the Pisano group all the more colorful, brighter and fun.

Finally, I would like to thank my parents, sister and girlfriend for their continuous support and their unlimited patience.

Chapter 1

Introduction

1.1 Surface Microfluidic Systems

Chemical/gas detection and biological analysis are inefficient, complex, time-consuming tasks that have significant impact on healthcare, national security, and advancements in science. The current state-of-the-art involves multi-step procedures depending on the desired assay where integration between steps is difficult, if not impossible. The typical laboratory assay consists of the following stages:

1. Sample collection (e.g. aerosol, liquid, surface swabs)
2. Separation and purification (e.g. lysis, centrifugation, filtration, electrophoresis)
3. Detection (e.g. fluorescence, ultraviolet-visible (UV/VIS) spectrum analysis, qualitative changes)

This procedure can have considerable sample loss, high power consumption, and can take several hours to several days to complete. Numerous attempts have been made to miniaturize the complete process to lab-on-a-chip devices; however, those methods typically rely on multi-step fabrication processes, complex fluidic interconnect, large ancillary devices, and off-chip optical detection. While these systems may be attractive for reduced sample volume, decreased assay time, or a number of other reasons; they often neglect the key factors preventing their wide spread use. This has led to our development of an Integrated Polymeric Surface Microfluidic System (IPSMS). The goal of IPSMS is to evolve the current body of on-chip assays to a form factor that is better suited for field deployment. By integrating multiple layers of selectivity into a single device, the false positive rate should be significantly reduced over previous research that demonstrated single layers of selectivity.

IPSMS can be separated into several assay stages - Preparation, Separation, Detection and Extraction. To accomplish this, there are three main components in the system:

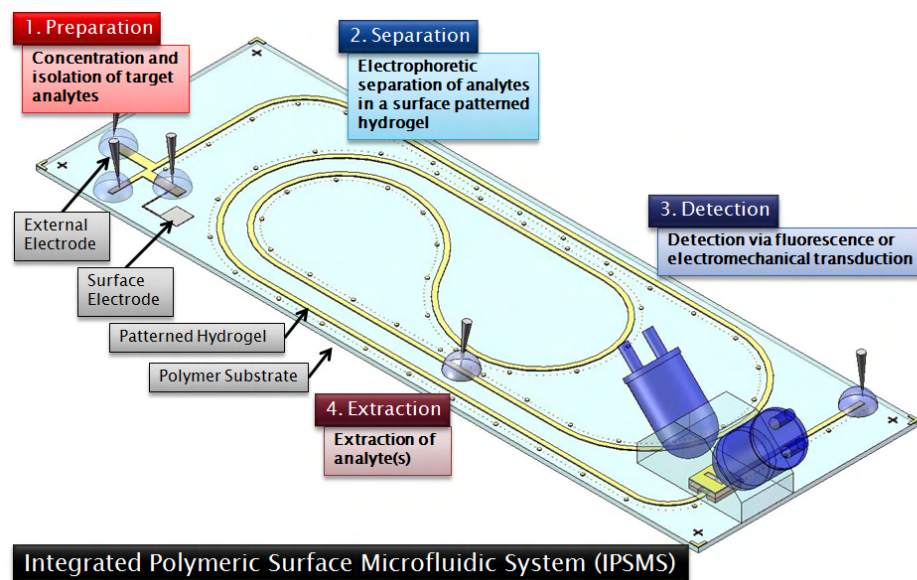


Figure 1.1: System overview of IPSMS. DNA from the unpurified sample is transported across the BLM by selective transport porins (Preparation-Component 1). Surface electrophoresis is used to transport samples around the chip and to perform separation of DNA into distinct bands (Separation-Component 2). The PNTFT, using optical transduction or electromechanical transduction, measures the analyte concentration or activity level (Detection-Component 3).

1. a hydrogel-supported, functionalized bilayer lipid membrane (BLM) for selective filtration, concentration, and/or sensing of a target analyte from an unpurified sample,
2. a patterned, thin-film of hydrogel for surface electrophoresis and electrophoretic transport on the surface of the chip, and
3. integrated, polymer-nanoparticle thin-film transistors (PNTFT) optimized for quantification of low-intensity fluorescent or electromechanical signals.

1.2 Current State-of-the-Art Assays

Chemical and biological detection is currently accomplished using either 1) simple, self-contained detection systems; or 2) laboratory-based analysis. Self-contained systems typically involve very simple detection schemes and are often subject to a high false positive rate when the analyte is difficult to discern from the background. Laboratory-based sample analysis is required for complex analysis and is the primary tool used when precise determination and detection is required. For example,



Figure 1.2: Real-time Polymerase Chain Reaction (PCR) analysis system built by Cepheid, Inc.

the Centers for Disease Control (CDC) uses manual assays to monitor food-borne pathogens.

Laboratory assays rely on a number of macro-scale processes such as centrifugation, gel electrophoresis, capillary exchange columns, polymerase chain reactions, robotic fluid handling systems, and environmental control systems. The cost of maintaining a laboratory with all the required equipment, reagents, and staff is considerable. In addition, depending on the target assay the equipment and reagent requirements can vary dramatically.

Self-contained systems are a lower cost alternative to laboratory analysis; however, successful systems are typically restricted to very simple assays that have very selective single stage detection. A great deal of research has targeted the development of lab-on-a-chip systems and has made significant advances. Currently, the factors limiting wide-spread deployment involve fabrication, packaging (fluidic interconnect), and ancillary equipment. The goal of this research is to mitigate these limiting factors by simplifying the fabrication process, eliminating the need for fluidic interconnect, performing detection on-chip, and greatly reducing the need for high-power, high-cost ancillary equipment.

The IPSMS presents several innovations to solve the multiple problems with chemical/gas detection and biological analysis techniques today. These innovations are:

1. Integration of preparation, separation and detection steps on a miniaturized lab-on-a-chip platform. This results in minimal ancillary equipment as all steps are performed on chip.



Figure 1.3: Agilent 7100 Capillary Electrophoresis System built by Agilent Technologies, Inc.) [1].

2. Delivery of the sample unprepared (can be a raw sample) and in droplet form. Therefore the system has no fluidic interconnect. This is possible due to the BLM performing active filtration of the sample and concentrating the analyte of interest into the hydrogel below.
3. All sample transport on chip is performed through surface electrophoresis (SE) and removing the need for pumps.
4. On-chip detection through PNTFT sensors potentially allowing higher resolution, more sensitivity and removal of bulky detection equipment.
5. Minimal false positives due to multiple levels of selectivity and much higher sensitivity starting from the BLM to the PNTFT sensors.
6. Simplified, bulk microfabrication of polymers with no sealing / bonding issues.
7. Faster response times due to integration of processes to a single chip and scaling.
8. Lower system costs due to minimal ancillary equipment and polymeric nature of the system.

1.2.1 Impact of IPSMS

Fast, reliable detection and identification of biological threats as well as biological materials required for engineering of pharmaceuticals and synthetic organisms are some of the greatest challenges in biotechnology today. A considerable hurdle to achieving this goal is the amount of diagnostic equipment and preparation equipment required to complete the task. A common concept to solve this problem is

lab-on-a-chip. Much research and effort has been placed into creating such an efficient, miniaturized setup; however, more problems are created in the requirement of microfluidic interfaces. In fact, reliable “plumbing” has seriously hindered both the macro- and micro-versions of these systems. The result has been long analysis times (a full day or more just for electrophoresis) and substantial amount of false positive results.

IPSMS deals with both problems of extraneous equipment and microfluidic interfaces through the innovation of surface microfluidics. We utilize and extend the concept of electrophoresis to drive fluids in patterned hydrogels on a chip. Utilizing bi-layer lipid membranes and their proven ability for selective filtration, the system can take raw, unprepared samples and select only analytes of interest for further separation in gel and identification. With microscale, surface gel electrophoresis, higher voltages and thus faster electrophoresis can occur, without compromising accuracy when compared to bulk gel electrophoresis. Finally, direct electro-optical or electro-proteomic sensing by novel, polymer-nanoparticle transistors result in fast, sensitive identification of analytes and their concentration - all with minimal extraneous equipment (mainly just a voltage supply and appropriate analog/digital readout equipment) and no microfluidic interfaces to and from the chip. Being fabricated on a polymeric substrate, the cost of the system is substantially reduced and robustness increased. The entire system can be disposable for simple, standalone use for detection of pathogens at busy centers like airports, detection as well as identification of required genes/plasmids in synthetic biology labs and fast, efficient separation and concentration of chemicals for pharmaceuticals.

1.3 Polymer-Nanoparticle Thin-Film Transistor

The typical laboratory assay’s third main stage is for detection. In order to achieve this, highly sensitive sensors and complex optics are normally utilized. The result is a platform which is high in cost and bulky. Popular detection mechanisms used today include fluorescence identification, UV/VIS spectrum analysis and qualitative analysis. For IPSMS, a sensor low in cost, sensitive and directly fabricated under or placed in direct proximity to the channel to remove the need for complex optics was required. To accomplish this, an innovative approach of printable sensors was used. To achieve high sensitivity, a phototransistor platform was selected. For low cost and printability, organics and semiconductor nanoparticles were explored. A third requirement was robustness due to exposure to ambient environments. This led to the choice of a germanium nanoparticle nanocomposite active layer on a low-temperature back-gated thin-film transistor base, resulting in a phototransistor for detection of fluorescence of analytes and their tags in the surface-printed channels of the IPSMS system.

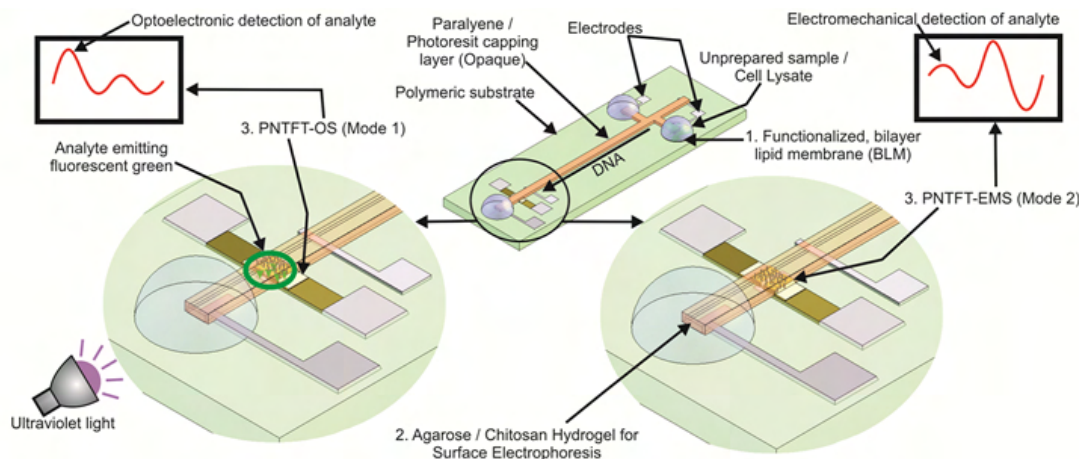


Figure 1.4: The PNTFT and its two modes of operation as a sensor in the IPSMS. Mode 1: Optically Sensitive (PNTFT-OS). Mode 2: Electromechanically Sensitive (PNTFT-EMS).

1.4 Current State-of-the-Art

1.4.1 Organic Semiconductors

The large-scale interest into the development of low-cost electronics has resulted in widespread research into a class of organic molecules called organic semiconductors. These organic molecules can be deposited into films and have a π -conjugate systems. Unpaired electrons and π -electrons can be used for current flow in these films resulting in semiconductor performance. While literature has shown that organic semiconductor films can achieve performance on par with amorphous silicon with mobilities between $1-10 \frac{cm^2}{V \cdot s}$, these films are highly oxidizing and unstable in ambient environments which have oxygen and moisture. As a result, costly encapsulation processes are required which do not always provide sufficient protection for the films. Also, organic devices such as organic transistors cannot be utilized or fabricated in ambient environments. Semiconductor nanoparticles like TiO_2 are often added to the organic semiconductor framework to enhance electrical performance since organics are poor electron carriers and help increase robustness of the overall material. While the electrical performance is enhanced, robustness still does not increase to a level where the film is robust in ambient atmospheres. However, these organics offer the promise of spin-processing and printing, dramatically lowering cost and waste during manufacturing which is sufficient reason for further research in this field to produce more robust, but still high performing organic semiconductors.

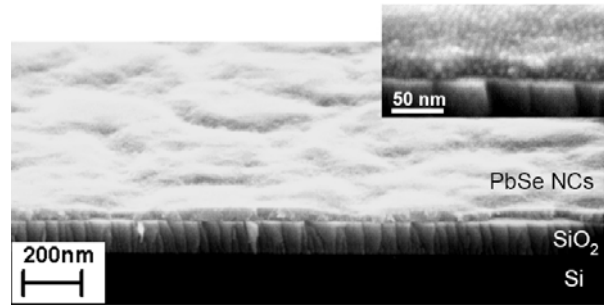


Figure 1.5: High resolution cross-section Scanning Electron Microscope (SEM) image of the channel of a lead selenide (PbSe) nanoparticle transistor [2].

1.4.2 Nanoparticle devices

With the realization that a substantial amount of research would be required before organic semiconductors will reach levels of robustness and performance rivaling alternatives such as amorphous silicon, a new thrust was generated to develop devices utilizing semiconductor nanoparticles with little to no organics. The goals that lead to the development of organic electronics were the same, including low-cost, low-temperature processing on multiple substrates. The problem and advantage of semiconductor nanoparticles lies with quantum confinement. While this quantum property of the nanoparticle can give them enhanced optical properties from varying emission and absorption wavelengths to an avalanche-type mechanism resulting from the input of only one photon, the nanoparticles also act as “carrier sinks,” to prevent carrier transfer between particles. In order to allow for carrier transfer between the particles, Talapin *et al.* found it was necessary to reduce the particle radius and interparticle spacing below that of the exciton Bohr-radius of the particle. While few semiconductors have large exciton Bohr radii, Talapin *et al.* utilized PbSe since it was one of the few with a large radii greater than 20 nm and could be controllably synthesized. This led to their development of a PbSe thin-film transistor where hydrazine was used in part to prevent the particles from oxidizing and dope them. Performance was further improved by annealing the transistors and thus removing the hydrazine. Overall performance of the transistor was on par of that of α -Si TFT with mobilities between 1-10 $\frac{cm^2}{V \cdot s}$, like the best organic transistors. The transistors were solution processable as well. However, there were several major setbacks to these devices. The first, was the use of highly toxic chemicals such as hydrazine, lead and selenium for fabrication of the transistors. The second, was the robustness of the device. The devices needed to be tested in a non-oxidizing ambient since the hydrazine did not do a suitable job of passivating the particles. Also, in order to shift the doping, the hydrazine was actively removed which opened up the highly oxidizable Se sites on the nanoparticles. The third, was the fact that the particles were not well

immobilized on the TFT base. While van der Waals forces could hold the particles in place, the particles could possibly shift in location due to electromigration and other forces resulting in drift in performance of the transistor over time. Therefore, while promising, using a primarily nanoparticle approach had several setbacks as well [2].

1.4.3 Nanocomposite devices

To achieve a robust, printable, low-cost optical sensor with mobilities equal to that of α -Si, one can refer to the IBM PbSe TFT, but go with the opposite approach of completely retaining the organic scaffold to protect the particles in ambient atmosphere. The scaffold also needed to be highly robust and stable. Due to the presence of the scaffold, a semiconductor with an even larger exciton Bohr radius would be preferred. Also, the semiconductor would need an appropriate bandgap energy such that it would be able to absorb the correct bands of light used in fluorescence. Finally, the bulk semiconductor properties would need to be on par or better than α -Si. Keeping the above in mind, germanium was chosen. Germanium has a large exciton-Bohr radius of ~ 25 nm. With a bandgap of 0.67 eV and a reduction of the nanoparticle diameter to 10 nm, the bandgap is increased to ~ 1.0 eV which is a good match for absorbing visible light from fluorescence. What remains to allow usage of the particles are thiol functional groups and a chitosan scaffold to both protect the particles from oxidation and arrange the particles into a robust film for usage in the active layer of the transistor. With the active layer deposited on a low temperature processed TFT base with aluminum source, drain and gate and α -SiC dielectric, the transistor can be fabricated on a variety of plastic substrates which would be compatible with the rest of the IPSMS device. The metal for the source, drain and gate can also be printed using gold nanoparticles based on a process by Park et. al and an organic dielectric could be used instead of the α -SiC [12]. The α -SiC does give the advantage of being much more robust under a variety of environments including ionic buffer solutions and is a high-k dielectric with ϵ_r of 9. The disadvantage of the α -SiC is the need to be deposited under high-vacuum requiring all transistor fabrication to occur first during IPSMS processing. No examples of either germanium nanoparticle transistors or fully-passivated, robust organic-nanoparticle transistors in general exist in literature. The only published examples of nanoparticle-based work are from Talapin *et al.* on PbSe-based transistors and these are not fully stabilized by organics. These transistors are also for optical and electromechanical sensing, which has not yet been demonstrated either.

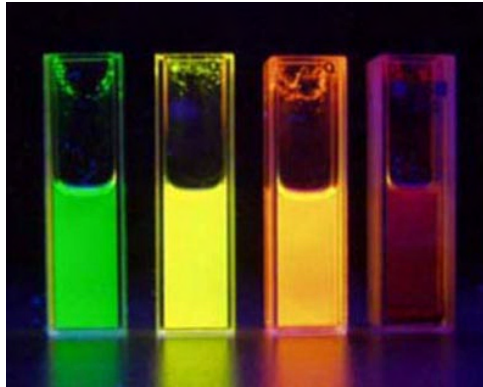


Figure 1.6: Cadmium selenide quantum dots of various diameter fluorescing under UV light [3].

1.5 Optical fluorescence sensing

1.5.1 Enzyme-Linked ImmunoSorbent Assay (ELISA)

One of the foremost methods of identifying unknown targets is through the use of antibodies that tag the unknown antigen and then the antibody-antigen pair are linked with a fluorescent protein allowing for the optical identification and quantification of the target molecule. This method is known as Enzyme-Linked ImmunoSorbent Assay (ELISA). IPSMS utilizes an ELISA-like process and also the same fluorescent reporter proteins which normally fluoresce green (509 nm), yellow (527 nm) and red (615 nm). The detector needs to be sensitive to these wavelengths. Normally a complementary metal-oxide semiconductor (CMOS) photodiode or phototransistor is used in the detector for detecting the fluorescent light. The idea of using nanoparticles for the detector comes from quantum-confined semiconductor nanoparticles, also known as quantum dots, being used in place of the fluorescent tags due to their higher fluorescence and lifetime. Quantum dots vary the wavelength of light based on the radius of the particle. The smaller the radius, the shorter the wavelength of light. The quantum dots can absorb all wavelengths of light shorter than its emission wavelength. Similarly, the nanoparticles used in the PNTFT absorbs all wavelengths shorter than its emission wavelength, but rather than re-emit the absorbed energy as light, the excitons formed are used in generation of free electrons and holes to act as charge carriers in the transistor.

1.5.2 Current detection methods

Current detection methods use fairly complex optics for quantitative analysis of samples [13–16]. While the detector normally uses CMOS-based technology from



Figure 1.7: Compact laser-induced fluorescence detector made by Picometrics, Inc. [4]

photodiodes and phototransistors to charge-coupled devices (CCDs), in order to excite the fluorescent tags sufficiently for detection, a laser with complex optics to direct and align the beam to the sample is required. Spectral filters to differentiate between the different wavelengths are also normally required. If qualitative analysis is all that is necessary, one can normally visually detect the fluorescence and in the case of low fluorescence, use a microscope to detect the events. Unfortunately, this results in these methods either being cheap and non-selective or highly expensive and selective. There are no intermediate options and all methods require large amounts of equipment overhead except LED-based fluorescence set-ups. Unfortunately those methods also place limitations on analyte type that can be detected. Therefore the PNTFT, which can use particles of various diameter to allow for specificity in wavelength detection and due to its placement in close proximity to the channel, can allow for a LED-based detection set-up results in reduced equipment overhead and lower overall cost.

1.6 Organization of Thesis

This thesis is divided into five chapters including the introduction. The second chapter, Chitosan Photolithography, covers the process developed to allow for patterning of the biomaterial chitosan using bulk microfabrication techniques. The process allows for the usage of multiple substrates while being flexible enough to be used for other polymers, especially hydrogels. The third chapter covers the development of a Polymer Nanocomposite for use as the active layer of a thin-film transistor. This includes development of a synthesis method for germanium nanoparticles and functionalization of the nanoparticles to enhance their electronic properties and stabilize them in oxidizing ambient environments. Throughout this section and the remainder of the dissertation, nanoparticle and nanocrystal will be used interchangeably should the particle in question both be nanoscale and crystalline in structure (as opposed

to amorphous). The fourth chapter discusses the incorporation of the nanocomposite into the thin-film transistor base to develop the PNTFT. Finally, the fifth chapter, Future Work, summarizes the research performed on the development of the PNTFT and future directions for which this technology could be applied.

Chapter 2

Chitosan Photolithography

2.1 Background

Chitosan is the partially deacetylated derivative of chitin, the second most naturally abundant polysaccharide on the planet to cellulose. Chitosan's biocompatibility and anti-inflammatory properties make it suitable for use in sutures, as a pharmaceutical additive, drug delivery agent, hydrogel-base for contact lenses, as a coating in prosthetics and implants, and can be used as a flocculant in wastewater treatment [17]. However, for all of chitosan's numerous applications, its potential is severely hampered by lack of material development at the micro- and nanoscale. Nature primarily utilizes the scaffolding nature of polysaccharides, weaving proteins and other biomolecules into the matrix to form the intricate bodies and hard shells of insects and crustaceans, utilizing a bottom-up approach at the micro- and nano-level.

Research into chitosan and chitin has existed since before the 1960s, though it was not until recently (ca. 1990) that chitosan's potential for incorporation into microdevices was studied. Chitosan has many potential microscale applications, mainly due to its various medical properties from being biocompatible to enhancing immunoreponse to aid in healing. Its hydrogel and floccating properties which make it ideal for treatment of wastewater has also shown potential for sensors detecting heavy metal ions [13]. Recently, research has also demonstrated high potential for chitosan in the formation of quantum dots and nanoparticles which can be directly applied towards fluorescent tagging of specific molecules like DNA and making the dots themselves biocompatible [14, 15]. Films of these chitosan-semiconductor quantum dots have also been created resulting in many potential optical applications including LEDs and photodetectors once suitable structures can be patterned into the films [16, 18]. Chitosan also demonstrates possible applications as an IR transducer. Chitosan and chitin both share very similar infrared (IR) absorbance spectrums, both having strong, narrow band absorbance near 3 and 9 μm (matching IR emitted by forest fires and mammals). This fact, combined with the usage of chitin in construction of the sensilla, IR

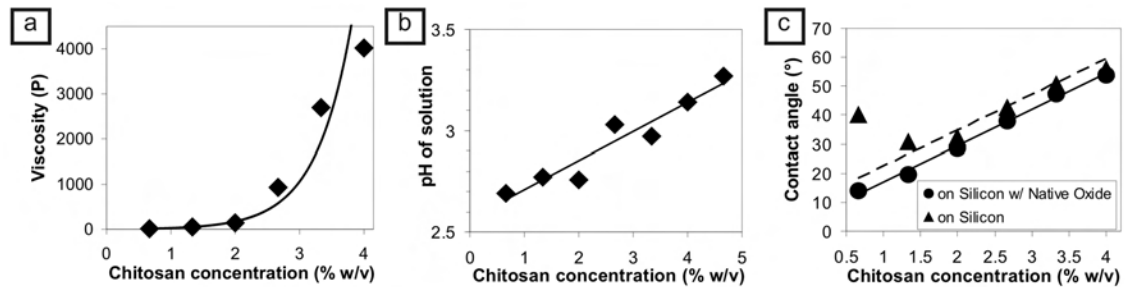


Figure 2.1: Characterization of chitosan hydrogel solution. a). Viscosity of chitosan hydrogel solution as the concentration of chitosan is increased. b). pH of chitosan hydrogel solution with varying concentration of chitosan. c). Chitosan hydrogel † solution contact angle on bare silicon and silicon with native oxide. †solvent was 150 mL of 2:1 buffered acetic acid.

sensitive microstructures of *Melanophila acuminata*, a pyrophilous (fire-loving) beetle, as well as several other pyrophilous beetles, has led several researchers to believe that the polysaccharide plays a key role in the detection of IR and could be used to create a biomimetic counterpart [19, 20]. Polymers are already garnering interest as IR absorbers and actuators in IR devices [21]. Chitosan’s bioscaffolding property has garnered attention for microscale biodevices with some research already being performed in this field [22–27]. With the numerous enzyme-substrate combinations already identified to be compatible with chitosan, multiple forms of these devices are possible with ability to microfabricate chitosan structures [11].

Advances in microprocessing technologies can open many interesting possibilities for the material. Thus, chitosan must be made into an ‘engineering material’ - capable of being microprocessed and fabricated into patterned films - before proper characterization and incorporation of the material into a micro-sensor platform can be accomplished. Several examples exist of work to make chitosan into an ‘engineering material.’ Acetylation of the chitosan can be controlled in a bath of 5% v/v acetic anhydride solution in methanol allowing fabrication to be performed with the more compatible chitosan form should chitin be the preferred resultant material [28]. Soft lithography where a pre-formed mold or stamp is used, such as in nanoimprinting, has potential biological applications [29]. However, due to (a) poor mold/stamp alignment necessary for various biological functionalizations [30], (b) requirement for uniform surfaces and (c) poor feature definition without usage of material modifying plasticizers [31], a better alternative is necessary. Rapid prototyping of chitosan, advantageous in simplicity and speed, has been attempted though is mainly limited to macroscale patterning due to limitations on feature sizes, fidelity and uniformity [32]. Electrodeposition can be used due to the cationic property of chitosan, but again has limited applications due to the requirement of a conductive substrate [33]. Re-

cently, a photocrosslinkable version of chitosan was developed and photolithography performed with features sizes of $\sim 100\ \mu\text{m}$ [34]. This method, as well as the other examples mentioned, requires patterning the chitosan while fully hydrated. This can result in swelling problems and reduced chemical robustness because of chitosan's hydrogel nature. For the photocrosslinkable chitosan, the swelling primarily introduces limitations on resolution while the crosslinker reduces the available functional units of the chitosan available for scaffolding purposes. In this thesis the development of 1) chitosan solutions safe for incorporation into normal IC processing, 2) a spin-casting process for these solutions and 3) a "dry" photolithographic patterning process that prevents swelling problems will be presented.

2.2 Process

For development of a microfabrication process, chitosan solutions of varying viscosity, created by dissolving between 1-6 g of medium molecular weight (MMW) grade chitosan (average molecular weight of 250 kDa, from Sigma-Aldrich) into 150 mL of glacial acetic acid buffered by deionized water (HAc : DI H₂O = 1 : 2 solution; chitosan concentrations between 0.66 % w/v to 4.0 % w/v). Higher chitosan concentrations were not utilized since it was found viscosities higher than 4.0 % w/v were very difficult to purify, test and process. These high concentration chitosan solutions would quickly clog membrane filters with 30 μm pores and once filtered, due to the high surface tension of the solution, degassing the solutions to form smooth, defect free films required more than an hour in ambient. The chitosan solutions were created by adding chitosan slowly to the buffered acetic acid solution while stirring and heating at 40°C to promote dissolution. The solution was continuously stirred and heated until all the chitosan was dissolved resulting in a yellow, viscous solution. Removal of particulates was accomplished using vacuum filtration down to 5 μm . Due to the medium to high viscosities of the hydrogels, membrane filters of 5 μm pore size were found to be the best balance between time required to filter the solutions and removal of the majority of the particulates. The particulates themselves were mostly small quantities of dust which made their way into the solution during processing. Filters of smaller pore size can be applied at this step based on purity requirements of the application. The stresses were measured for several spin-cast films deposited from 4.0 % w/v chitosan solution. For biaxial modulus and CTE measurement of the film, the two substrates used were silicon and aluminum.

Deposition of thin-films of the chitosan was achieved through spin-casting the chitosan solutions using a (Headway) Photoresist Manual Spinner as shown in step 1 in Figure 2.2. These films were baked at 90°C for five minutes to evaporate away the solvent, partially neutralizing the film. As the remaining acidity here does not interfere with the patterning of the chitosan structures, pH neutral or basic solutions utilized in later processing steps serve a dual function of further neutralizing the films. This

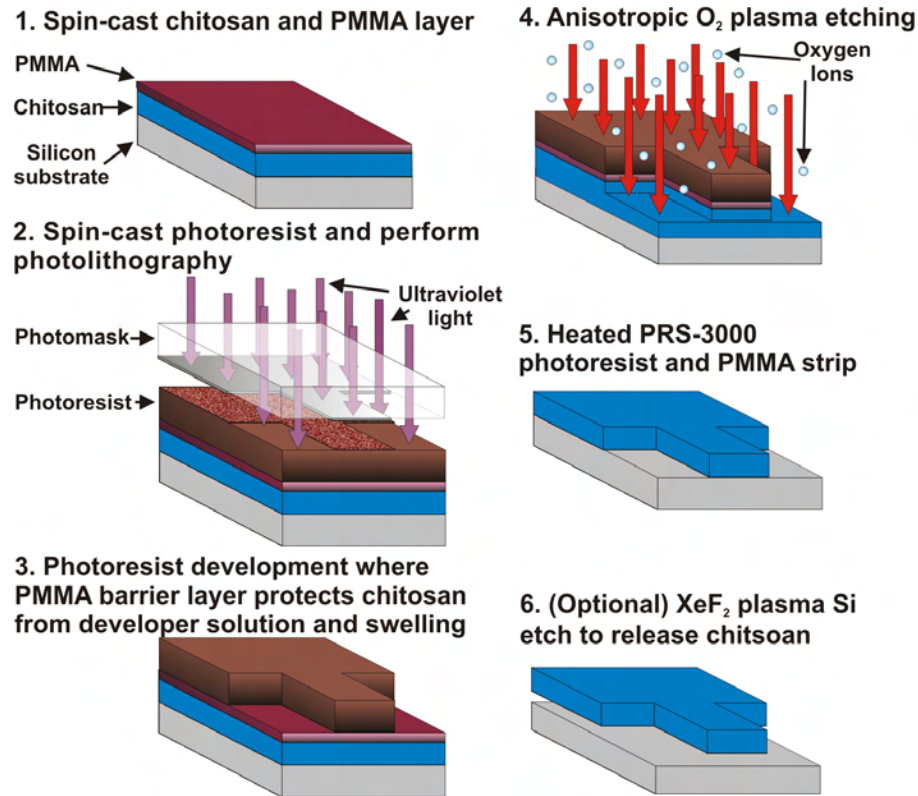


Figure 2.2: Chitosan photolithography process utilizing a PMMA barrier layer for protection against swelling issues. Includes an optional XeF₂ plasma Si etch for the release of chitosan structures.

removes the need for adding an extra neutralization step which in many cases could affect underlying devices due to the basic solutions used. A film of thickness 500 nm of 495 C5 poly(methyl methacrylate) (PMMA) (MicroChem) was also deposited using the manual resist spinner to act as the barrier layer to protect the chitosan from the photoresist developer. For photoresist deposition, predefined photoresist layer programs for the (SVG) photoresist spin-coat tracks were used. For up to 2-3 μm thick layers of chitosan, the 2 μm thick OCG 835 35CS G-Line program was selected (2 coats of G-line for chitosan layers $\sim 3 \mu\text{m}$ thick) and for thicker chitosan layers, the 10 μm thick (Rohm Haas) I-Line SPR-220 program was selected.

Exposure was performed using the (Karl Suss) MA6 Mask Aligner contact printer shown in step 2 in Figure 2.2. Exposure times were varied based on the lamp intensity, thickness of chitosan and photoresist. The photoresist was then developed with OCG 934 2:1 G-Line developer on the (SVG) developer track (step 3 in Figure 2.2). Due to the barrier layer, sufficient exposure of the photoresist to fully bring out features in the

photoresist can be performed. Also, development does not need to be meticulously, manually performed to prevent chitosan swelling.

For transferring the patterns to the chitosan, an anisotropic oxygen plasma reactive-ion etch in the (Plasma-Therm) PK-12 Reactive-Ion Etcher system was performed as shown in step 4 in Figure 2.2. This, combined with the anisotropic nature of the etch (from the applied DC bias in the system), resulted in good transfer of the photoresist pattern to the chitosan with limited pattern erosion even with overetching to account for non-uniformities in the film. All etching was performed at 40 mTorr with the substrate stabilized at 20°C via a water-cooled bottom electrode. The photoresist and PMMA was then stripped in a 75°C PRS-3000 bath (J. T. Baker) shown in step 5 in Figure 2.2. The wafer was then soaked and rinsed with deionized water to remove particulates. These steps acted to further neutralize the chitosan patterns. The wafers were then dried with nitrogen. As an optional step, a XeF₂ plasma silicon etch can be used to release the features should the chitosan be deposited on a silicon substrate as shown in step 6 of Figure 2.2.

2.3 Results and Discussion

Chitosan is soluble in weak acids due to a low pKa of approximately 6.5 and once in solution, protonation of the amino groups gives chitosan a cationic nature [35]. This leads to the formation of chitosan hydrogels that have been shown to swell in response to changes in pH and humidity [36]. This hydrogel nature is also conducive toward developing a microfabrication process for patterning the material. Additionally, as mentioned earlier, should chitin be the preferred resultant material, East *et al.* developed a method to acetylate chitosan [28].

Determination of several key chitosan hydrogel solution properties - pH, viscosity and contact angle - were performed. pH measurements were performed using a digital pH meter, dynamic viscosity using a concentric viscometer and contact angle using the (Kruss) contact angle analyzer system. To obtain approximate viscosity measurements and for simplicity of analysis, we assumed the chitosan solution was a Newtonian fluid and there was negligible friction on the bottom surface of the viscometer. A more thorough determination of the viscosity would require the use of non-Newtonian models. An approximate model was sufficient for the needs of these experiments so more advanced modeling was not performed. Increasing the chitosan concentration while keeping the solvent properties constant (pH of 2.33) resulted in increasing pH levels and viscosity. From Figure 2.1a, it can be seen that an exponential curve best fit the increasing viscosity measurements while pH increased linearly with chitosan concentration as seen in Figure 2.1b. This allowed for a large range of solution viscosities with a small to moderate change in pH minimizing hydrogel swelling due to pH changes for the various solutions. Chitosan solutions with 0.66% w/v chitosan concentration had three times less the viscosity of SU-8 2025 (MicroChem)

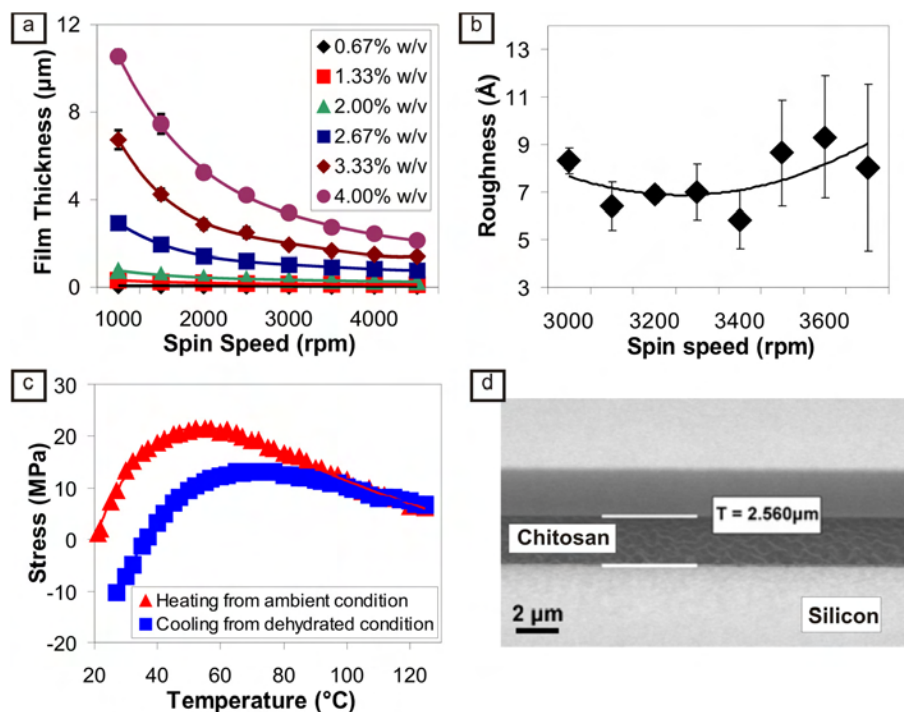


Figure 2.3: Characterization of chitosan thin-films. a) Chitosan spin curves for chitosan concentrations varying between 1 g (0.66% w/v) to 6 g (4.0% w/v) dissolved ($n = 6$) b). Surface roughness (R_a - center-line roughness) of 3 g (2.0% w/v) chitosan films between spun using spin speeds between 3,000 - 4,000 rpm ($n = 3$). c). Stress-temperature curve for 6 g (4.0% w/v) chitosan film ($T = 3.4 \mu\text{m}$), where tensile stress is positive d). SEM image of a cross section of a 2.56 μm chitosan film on silicon with native oxide taken with sample at 80 $^{\circ}$ tilt.

photoresist (36.9P) [37]. Chitosan solutions with 4% w/v chitosan concentration had approximately seventy times the viscosity of the SU-8 photoresist above. Such a large range of viscosities proved to be conducive towards creation of films of thickness between tens of nanometers to several microns. Due to the weak acidic nature of the solution and the fact no fast diffusers were utilized in solution processing, exposure of metal oxide semiconductor (MOS) devices fabricated on a silicon substrate to the solution was expected to have negligible effects. Also of importance was that films from the hydrogel, which still required neutralization, would simply be neutralized when exposed to more basic solutions throughout the course of the photolithography process.

Another important solution characteristic that helped determine how the chitosan solution would be spin-casted was the contact angle the hydrogel made with the substrate. Solutions with lower contact angle wetted the substrate surface better

resulting in a better spin. Higher contact angles resulted in greater hydrophobicity requiring larger amounts of hydrogel to be dispensed to sufficiently cover the substrate surface when spin-casted. However, higher contact angles also resulted in a thicker spin-casted film. The contact angles for various chitosan hydrogels with varying concentrations of chitosan on bare silicon and silicon with native oxide are shown in Figure 2.1c. While the contact angles increased linearly with increasing chitosan concentration, for even 4.0 % w/v solution, the contact angle remained below 90° for both substrate types resulting in overall hydrophilic wetting and allowing for adequate spinning of the hydrogels.

Deposition of thin-films of the chitosan was achieved through manual spin-casting as mentioned above. Experimentally, it was found that a spin-time of one minute provided sufficient time for 4 mL of the chitosan solutions to be spun across the 4 inch silicon wafers. Spin speeds ranged between 1000- 4500 rpm. The native oxide layer was kept on the wafers as it provided better wetting of the hydrogel to the wafer surface (as seen in Figure 2.1c) and it did not affect further processing steps. The resultant spin curves for the chitosan solutions prepared can be found in Figure 2.3a. Film thickness increased quadratically with increasing chitosan concentration while a decreasing power function was found to be the best fit to the spin curves themselves. A large range of film thicknesses (min: 44.1 ± 2.1 nm; max: 10.6 ± 0.4 μm) was thus achieved. The most uniform films were achieved with spin speeds between 2500- 3500 rpm. The optimum spin speed to use for a particular solution was highly correlated to its viscosity. Spin speeds closer to 3500 rpm were chosen for higher viscosity solutions when focus was on uniformity and surface roughness. The surface roughness of 2.0 % w/v chitosan film was near 1 nm for spin speeds between 3000- 3700 rpm. Therefore the films showed good local uniformity while general uniformity across the wafer was generally better than 20 %. For the smoothest films spun near 3000 rpm, the general uniformity was 10 % or better. A cross section of a 2.56 μm thick chitosan film, spun from a 4.0 % w/v chitosan solution, is shown in Figure 2.3d.

Stress in the film was an important issue, especially for applications such as IR sensing when using the material as the transduction layer. Stress was measured using the (KLA-Tencor) Flexus FLX-2320 Thin-Film Stress Measurement System. Utilizing the Stoney equation, modified to account for biaxial stress, the system computed the stress of the deposited film. The aforementioned equation was:

$$\sigma_f = \frac{E_f}{1 - \nu} \frac{h^2}{6Rt} \quad (2.1)$$

where σ_f is the stress in the deposited film, E_f the Young's modulus of the substrate, h the thickness of the substrate, ν the Poisson's ratio of the substrate, R the curvature of the film and substrate and t the thickness of the deposited film. Error when using the equation became significant when the deposited film became 5 % or greater than the thickness of the substrate. Also, the deposited film modulus should not exceed

the substrate modulus to a great extent for the equation to hold. The chitosan films' maximum modulus was less than 25 MPa, as shown in Figure 2.3c, while silicon had a modulus between 3-4 orders of magnitude higher. The deposited films were only several microns in thicknesses, much less than the 525 μm Si substrates they were deposited on. Therefore, usage of the Stoney equation in this case was valid allowing for relatively accurate stress measurements by the Flexus system.

The hydrogel nature of the chitosan film resulted in the film having the tendency to absorb ambient moisture in the environment. Accordingly, moisture in the ambient environment in the microlab was highly dependent on the temperature as the ambient conditions in the microlab were usually moderately controlled for better process control. In Figure 2.3c is shown the stress-temperature curve for a 3.4 μm thick chitosan film. The temperature was cycled between 21°C to 125°C. Since the film started from ambient conditions (rather than a totally dehydrated form), it could be seen that the film's intrinsic stress was relatively low. The stress increased in the film due to both a loss of moisture content and thermal expansion. However, during the cooling cycle, it was seen that the stress-temperature curve formed a hysteresis curve. Measurement of the same film after stabilization in ambient conditions for several hours resulted in the same stress-temperature curve. Therefore the loss of moisture was the likely reason behind the hysteresis aspect of the curve. Instead of the stress increasing or decreasing with a change in temperature, a maximum stress was achieved near 50°C for a film being heated from ambient conditions and 70°C for a film being cooled from a high temperature, dehydrated state. It was likely that the behavior was due to a trade-off between three film characteristics which varied with temperature: thermal expansion, loss of moisture and conformational changes in the chemical structure of the chitosan.

To extract the biaxial modulus and CTE, utilizing the Flexus system and above samples, the assumption was made that the film modulus and CTE were both independent of temperature. With these assumptions, the following approximation was used:

$$\frac{\partial \sigma_f}{\partial T} = \frac{E_f}{1 - \nu_f} (\alpha_s - \alpha_f) \quad (2.2)$$

where σ_f is the stress of the film, T the temperature of the film, E_f the Young's modulus of the film, ν_f the film's Poisson's ratio, α_s the CTE of the substrate and α_f the CTE of the film. The biaxial modulus of the film is $E_f/1 - \nu_f$. By determining the slopes of the stress-temperature curves of films on different substrates and interpolating between the data, both the biaxial modulus and CTE of the film could be determined. The CTE for a dehydrated chitosan film was determined to be 26.6 ppm/K while the biaxial modulus was 6.37 GPa. Assuming Poisson's ratio to be 0.45 like other polysaccharides and most resins, Young's modulus was determined to be 3.50 GPa. This was relatively similar to Young's modulus recorded by Domard

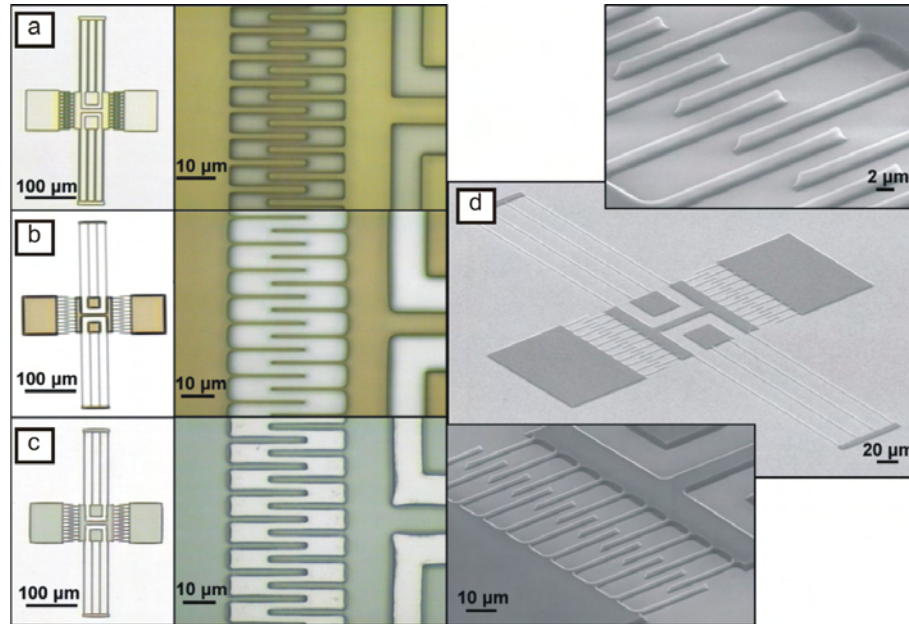


Figure 2.4: Patterning of a double-folded flexure MEMS resonator in chitosan ($T = 2 \mu\text{m}$) to demonstrate high-resolution patterning ability. Images show the resonator structure and magnified views of the comb structure after a) photoresist development, b) anisotropic oxygen ion etching and c) photoresist and PMMA strip. Image d) is a SEM image of the resonator structure at a 50° tilt and some magnified views of the comb structure (Note: structure unreleased).

& Domard of 3.62 GPa during their stress tests of dehydrated, mold-casted chitosan gels [35]. For films initially stabilized at ambient conditions for humidity (therefore the films contained some moisture content), the CTE was 45.4 ppm/K, biaxial modulus 248.7 MPa and Young's modulus was 136.8 MPa (assuming Poisson's ratio of 0.45).

It is important to note that the above measurements were sensitive to the ramping procedure used to obtain them. A ramp of $1.7^\circ\text{C}/\text{min}$ was used for these measurements. This was the fastest ramp that could be used while ensuring that the substrate and temperature both stabilized for the measurement. While the hope was that the film would retain a steady amount of moisture at the set temperature when starting from a stabilized ambient condition, this was unlikely to be the case as moisture was more likely to be evaporated from the films, especially at higher temperatures even if the reading did not take an extended period of time. This would result in an artificial increase in stress with each measurement so the second set of CTE measurements were likely underestimates of a film at ambient conditions. The biaxial modulus measurements, due to the artificial increase in stress, were likely overestimates of a film

at ambient conditions. However, they did provide a rough estimate for simulations of devices made from the material in ambient conditions.

Photolithography was chosen as the preferred method to pattern the chitosan films due to its ability to produce high resolution features and compatibility with numerous substrates and materials. Also, part of the goal was to develop a CMOS compatible patterning process. These goals ruled out the use of electrodeposition or mold-casting, currently used chitosan patterning processes at the micro- and macro-level. To achieve high resolutions (min. 1-2 μm features) without the inherent problems with wet etching - most prominently swelling of the chitosan films and chemical changes to the film primarily at the photoresist-chitosan interface - a dry photolithographic process for chitosan was developed. The dry photolithographic patterning of chitosan is a 5 step process as shown in Figure 2.2. The process utilizes a spin-casted PMMA barrier layer approximately 500 nm thick (deposited at a spin speed of 2500 rpm; ramp at 100 rpm/sec to final speed which is then held for ten seconds) to protect the chitosan chemically from photoresist developer and prevent swelling of the chitosan and thus any delamination of and eventual stress fractures in the photoresist from the swelling. The PMMA-chitosan stack was baked at 90°C for five minutes. Utilizing a PMMA barrier layer is useful due to its good selectivity to standard G and I-line photoresist developer and its ability to be stripped together with the photoresist in step 5 shown in Figure 2.2 saving an extra processing step and preventing chemical changes to the chitosan due to increased exposure to solvents. Standard development is used to develop the photoresist and an anisotropic oxygen plasma etch is used to transfer the pattern in the photoresist mask to the chitosan.

Test structures were fabricated in the chitosan films to test the limits of the process. Figure 2.4 above shows the fabrication of a double-folded flexure MEMS resonator in chitosan after photoresist development (Figure 2.2, step 3), anisotropic O₂ etching (Figure 2.2, step 4) and PMMA and photoresist strip (Figure 2.2, step 5). All the images in the figure were taken without filters and at the same illumination. As can clearly be seen from Figure 2.4, while the majority of the etch was vertical, some lateral mask erosion still occurred. The SEM images of Figure 2.4d show that the 2 μm width comb finger features were transferred well and that the fingers were indeed close to 2 μm in width at the finger base while closer to 1 μm in width at the top of the finger. The sloped sidewall resulted from sloped sidewalls in the photoresist mask. Resultant sidewall angle, measured from the SEM images, was between 60-70°. The difference in etch rates between the photoresist and chitosan in O₂ plasma also helped to increase the sidewall angle slightly by about 2° for 2 μm thick chitosan films. With plasma power at 70 W and a flow rate of 50 sccm, etch selectivity of photoresist to chitosan was found to be approximately 1:1.65. Also note the minor swelling apparent in Figure 2.4c since the image was taken after a deionized (DI) water rinse and N₂ dry. All other images were taken after at least one minute 90°C bake on a hot plate. Once the features are defined in the dry photolithography process,

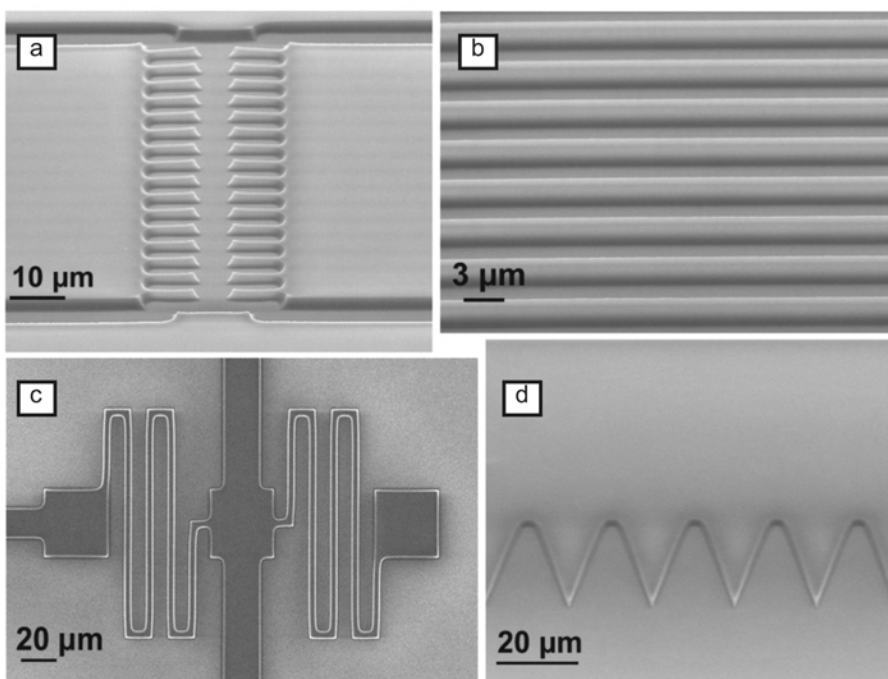


Figure 2.5: Photolithographically-patterned chitosan features. a) SEM of matched comb structure at a 50° tilt. b) SEM of $2\ \mu\text{m}$ wide lines with $4\ \mu\text{m}$ pitch. c) SEM of serpentine spring structures. d) SEM of sawtooth structure. Note: All patterns in a $2\ \mu\text{m}$ thick chitosan layer.

regardless of post-swelling, and the film is returned to its dry state, the original feature sizes are retained allowing as can be seen from the SEM images (film was completely dehydrated prior to imaging).

This allows for repeatable, controlled patterning of the film unlike current wet processes. A variety of other features were patterned from a test mask with single mask MEMS devices as shown in Figure 2.5. From the SEM images in Figure 2.5 it can be seen that even for $2\ \mu\text{m}$ wide lines with $4\ \mu\text{m}$ pitch, there is clear definition of features with trenches clear of chitosan. From Figure 2.5c, it is evident that at small resolutions close to $2\ \mu\text{m}$, there is some corner rounding, which, can also be seen in Figure 2.4a in the original resist masks. Therefore, it is likely that current resolutions are limited due to the use of contact printing and any scattering of light from the chitosan layer during UV exposure rather than limits in the O_2 plasma etch itself. To further decrease the resolutions using contact printing, it is likely that an anti-reflective coating (ARC) may be required or modification of the standard development programs used. The etch selectivity results in thicker chitosan layers requiring a thicker photoresist mask and therefore lower achievable resolutions. Features of sizes as small as $2\ \mu\text{m}$ are possible with chitosan film thicknesses less than

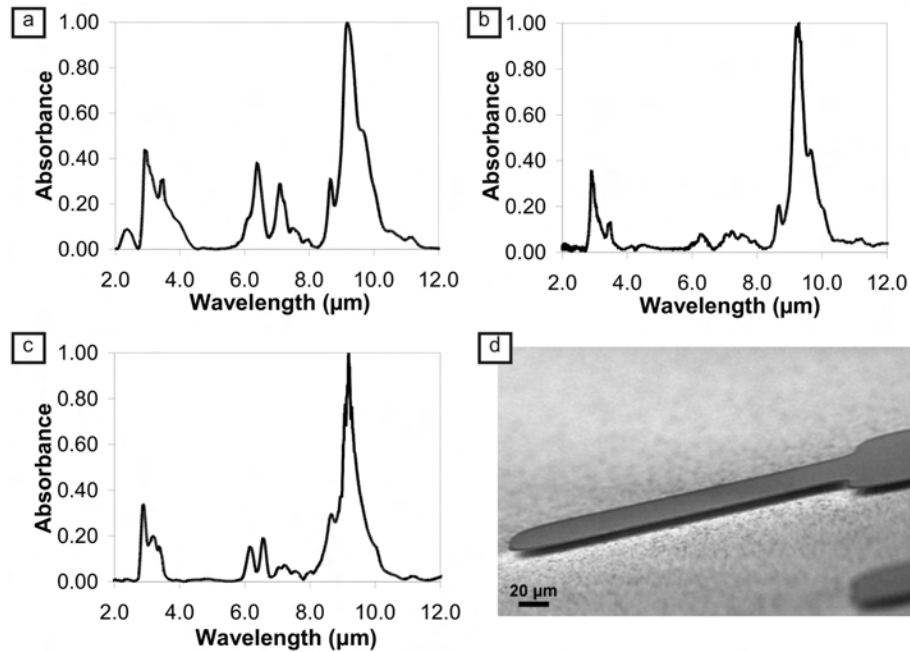


Figure 2.6: FTIR characterization of chitosan before and after processing. a) Normalized Fourier-transform infrared absorption spectrograph for the chitosan film layer before microprocessing. b) Normalized Fourier-transform infrared absorption spectrograph for the chitosan film layer after microprocessing. c) Normalized Fourier-transform infrared absorption spectrographs for the chitosan film layer after XeF_2 release etch. d) Partially released chitosan cantilever on silicon $240 \times 25 \times 2 \mu\text{m}$. Chitosan serves as a sufficient structural material to support itself.

$4 \mu\text{m}$. Resolutions for thicker chitosan films are limited by the sidewall slope which requires greater spacing between features and the features themselves to be of greater width.

To determine if the chemical nature of the chitosan films were not substantively altered by this photolithographic process, Fourier transform infrared (FTIR) absorbance spectrums were taken of the films both prior and after processing as shown in Figure 2.6. To a great extent, the spectrums showed characteristic peaks in the 3, 6, 7 and $9 \mu\text{m}$ bands, which implied that the films were chitosan and that the processing had minimal to no effect on the chemical characteristics of the film. An examination of Figure 2.6c shows the FTIR absorbance spectrum of the film after XeF_2 plasma etching and depicts minimal chemical changes to the film. To completely quantify the magnitude of the changes would require additional chemical analysis. A partially released chitosan cantilever $2 \mu\text{m}$ thick is shown in Figure 2.6d. To ensure proper release of the structures, the films need to be completely dehydrated prior to the release to prevent the formation of HF acid which could damage and etch the film. The XeF_2

release step, step 6 in Figure 2.2, is only required for released structures and is not inherently CMOS-compatible, unlike the other process steps. However, this release step is useful for the creation of chitin/chitosan microstructures for MEMS devices, the shown cantilever structure in Figure 2.6d being one of them. These chitosan films have also been found to retain functionality of amine groups, which has been explored in previous work involving the immobilization of β -D-galactosidase into these films [38].

2.4 Conclusion

Photolithographic methods for patterning chitosan are potentially the most flexible and precise methods for forming chitosan microstructures for future biomimetic/bio-inspired MEMS. This results from the simplicity of the method, high resolution, uniformity of films, possibility for multi-layer processing and scalability of the process due to use of bulk microfabrication techniques. The deposition and patterning process for photolithography developed in this research provides the ground work and a significant step toward the usage of chitosan in microdevices. The process allows for well-defined features on the order of a micron with the freedom to utilize a wide array of substrates. The process has been shown to cause only small chemical changes to chitosan and future work will include additional chitosan chemical analysis as well as process refinement. It also spurs the investigation into many alternative properties and uses for chitosan, especially those at the microscale. This photolithography-based method can still be optimized further including the use of less viscous solutions, which will provide comparable films to those of more viscous solutions through alteration of pH of the solvent, molecular weight and deacetylation factor of the chitosan, improved barrier layers and possibly anti-reflective layers for photolithography. The process was optimized for chitosan, but with little or no change, it can be applied to other hydrogels as well providing a straightforward, but very precise method for creation of micron-scale hydrogel structures. Additionally, due to the bulk fabrication methods adapted from CMOS processes, so long as the hydrogel itself is CMOS-compatible, the entire process can be adapted into a CMOS process provided the thermal budget remains below the sublimation or melting point of chitosan or other hydrogel itself.

Chapter 3

Polymer Nanocomposite

3.1 Background

As particles are reduced in size, a variety of interesting phenomena occur. These quantum effects arise from the larger surface area-to-volume ratio resulting in unique characteristics for these particles, especially as they drop below the exciton Bohr radius of their respective materials. These effects include desirable characteristics such as lower melting temperature and quantum confinement of carriers and undesirable characteristics such as rapid oxidation and low carrier mobility between particles. As a result, in the last fifteen years, much research has been performed on these particles to optimally synthesize them and utilize their characteristics. This section will explore research performed in this field for the development of nanocrystals (quantum dots - ie. 0D quantum boxes) and then delve into the synthesis methods used to form the nanocrystals used for the research of this thesis.

Multiple methods exist to synthesize nanoparticles of different sizes and geometry. These methods can be generalized into three general categories: 1) Gas Phase Synthesis, 2) Chemical (Liquid Phase) Synthesis and 3) Supercritical Fluid Synthesis. The first technique utilizes precursor gases that react and are quenched into a liquid where the particles are collected and if need be, functionalized. The second technique, liquid phase synthesis, utilizes a solvent, reactants and sometimes a catalyst to drive the reaction. The third technique, supercritical fluid synthesis, is very similar to liquid phase synthesis, however due to the use of supercritical fluids, solubility of reactants are often increased and due to functionalization prior to suspending the nanoparticles in the final solvent, a wide variety of solvents can be utilized for suspending the nanoparticles. Each technique has its benefits and disadvantages; a summary will explain more detail below.

3.1.1 Gas Phase Synthesis

Gas phase synthesis covers a variety of techniques which start with gas precursors to form nanoparticles. For the formation of germanium nanoparticles germane gas can be utilized while silicon nanoparticles often require silane gas. These gases are often purchased as a compressed gas, though can also be formed just prior to the reaction by evaporating/sublimating a liquid/solid, laser ablation or plasma etching. The gases are then fed into a reaction chamber. During this process the gases can be mixed and injected through a nozzle into the reaction chamber. This allows condensation to occur. Isobaric cooling (constant pressure) or isothermal compression (constant temperature) results in the gases to enter a supersaturated state. The thermodynamic equilibrium condition whereby the saturated vapor pressure P_0 is related with the absolute temperature T by the Clapeyron equation is:

$$\ln P_0 = A - \frac{B}{T} \quad (3.1)$$

where A and B are vapor dependant constants. Statistical fluctuation breaks this state and the reaction proceeds towards a lower energy state of equilibrium which causes the nucleation of the atoms into nanoparticle seeds, which can also be considered dispersed aggregates in a liquid environment [39]. To aid this nucleation, ultrasonic waves through the use of altered injection nozzles or an inert gas can be used. Once the particles are nucleated, the particles then need to be injected and suspended into a solvent. To prevent aggregation, oxidation and further growth of the nanoparticles, the ligand precursors are normally also present in the solvent and react to functionalize the particles. Once the ligand coat is formed, further growth of the nanoparticles is stopped and aggregation is prevented. With proper and stable functionalization, the particle oxidation can be halted or at least slowed.

Gas phase synthesis presents a plausible method to create nanocrystals starting from individual gaseous atoms. With the large body of knowledge of gas pressure and vacuum vessels, especially from the semiconductor industry where there are processes such as atomic layer deposition where atomically thick layers can be controllably deposited one layer at a time, many controls can be instituted to ensure proper and highly crystalline growth of the nanocrystals. One of these set-ups can be seen in Figure 3.1. It is often stated that one of the greatest advantages of this method is the fact that the particles are synthesized without any ligand coat and thus many different functionalizations could possibly be attached or another material coat (i.e. shell) before ligands need to be considered. Also, in some cases, the high reactivity of the particles need to be maintained so no ligand coat is required. The main disadvantage to the method lies in the quenching of the nanoparticles into the suspension solvent. In order to ensure that the solvent is not denatured, evaporated or reacting with the particles themselves, the temperature of the particles and carrier gas needs to be brought well below the boiling point of the suspension solvent. Furthermore,

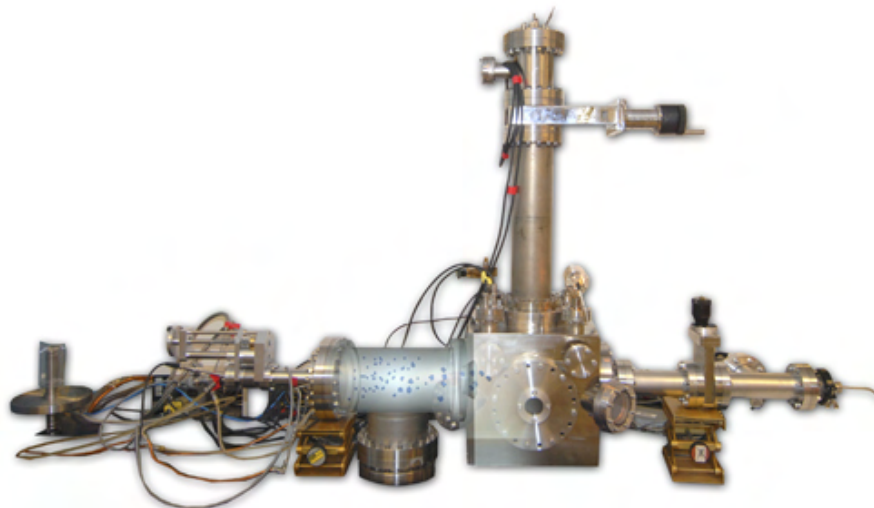


Figure 3.1: Gas phase synthesis setup employed by DRDC Suffield group in Canada [5].

the temperature of the particles also needs to be at the correct temperature for any further ligand functionalization reactions. The cooling required and control over the temperature of the carrier gas and nanoparticles upon injection is very difficult making choice of the suspension solvent crucial and very tricky. Also, by inducing high cooling into the set-up, there is a risk of introducing moisture which, due to the high oxidation potential of nanoparticles, can be problematic and thus require more complexity in the synthesis set-up.

3.1.2 Chemical Synthesis

Chemical, also known as liquid phase, synthesis is the oldest known and most widely applied nanoparticle synthesis method. The first known chemical synthesis of nanoparticles was for generation of gold colloids by the reduction of $[\text{AuCl}_4]^-$ by citric acid in water and was performed by Michael Faraday in the mid-nineteenth century [40]. Chemical synthesis occurs in five stages. These stages are:

1. Reduction
2. Nucleation
3. Growth
4. Stabilization



Figure 3.2: A typical Schlenk line and flask setup for chemical synthesis of nanoparticles under inert conditions [6].

5. Precipitation, Cleaning and Resuspension

The first stage is the reduction of the primary reactant. The primary reactant is often a metal complex such as copper acetate. Once the complexes are reduced into atomic ions, the second stage of nucleation begins. Often raised temperature is required to provide the required energy for either the full reduction to occur and/or nucleation to occur. Other reactions may instead require a catalyst such as platinum or electric potential to either lower or provide the energy for the reaction. During nucleation atoms of the same or complimentary nature bond together to form clusters of the element or compound (e.g. Si, Ge and CdSe). Once nucleation is completed the reaction progresses to the growth stage where the clusters are increased in size by merging of clusters or addition of more of the elemental atoms and compound to the original seed cluster. The additional energy provided for the reduction and nucleation stages can either be kept at the same level for this stage or lowered. The seed clusters often act as pseudocatalysts lowering the energy needed for further growth.

The fourth stage is stabilization of the nanoparticles. This stage includes both ending the reaction and stabilizing the nanoparticles so they are protected against oxidation and do not agglomerate. As many reactions require an increase in temperature to provide the needed energy, by lowering the temperature to ambient (normally around 25°C), further nanoparticle growth is stopped. However, normally the large surface area to volume ratio of the nanoparticles makes them highly prone to oxidation and agglomeration. Sometimes the surfaces of the nanoparticles are reactive enough that further growth will continue, even though the temperature has been lowered to ambient. Therefore ligands are utilized to place a coat around the nanoparticles to both limit the growth of the nanoparticles (self-limiting reaction), prevent oxidation and agglomeration. In many cases, these ligand coats are necessary to halt the reaction such that a very tight distribution of nanoparticle sizes occur. The final and fifth stage is the precipitation, cleaning and suspension of the particles. To induce precipitation of the nanoparticle from the reaction solvent, an alcohol such as methanol or ethanol is used. Acetone is also often used to precipitate the particles as well. These chemicals - ethanol, methanol and/or acetone - also act to dissolve unwanted reaction byproducts or even the reaction solvent. Then the particles are filtered and/or centrifuged to remove all unwanted contaminants leaving just the nanoparticles behind. The particles can then be resuspended into a solvent of choice such as acetonitrile, hexane or toluene. Once the final nanoparticle colloid is created, the particles are ready for use.

Chemical phase synthesis is amongst the most flexible synthesis methods with a large body of knowledge about the reaction kinetics. The reactants are in the easily manipulated forms of solid and liquid. The reactions can occur in both ambient and inert environments depending on the nature of the nanoparticles being formed and whether oxygen is a necessary reaction component. The apparatus necessary for chemical phase synthesis is simplest amongst all three synthesis methods and easiest to maintain. For functionalization of the particles and to limit their size for tighter size distributions and appropriate geometry, many different ligand coating techniques are available from micelles and reverse micelles to thiolation and hydrofunctionalization (such as hydrosilation and hydrogermylation). However, even with such a large body of knowledge around this synthesis method, due to interactions between the different stages used in synthesis and the need to understand each stage in its entirety to truly be able to optimize these reactions, chemical phase synthesis can also be considered to be the most complex amongst all the synthesis methods to understand. Other methods trade off complexity in the synthesis equipment for more control over the individual stages of nanoparticle formation and to make the reactions easier to understand and optimize. Gas phase synthesis uses vacuum equipment and several different chambers to isolate each stage of the nanoparticle formation. Supercritical fluid methods use supercritical fluids to increase the range of useability of reactants and eliminate the need to carefully choose and match the right reaction

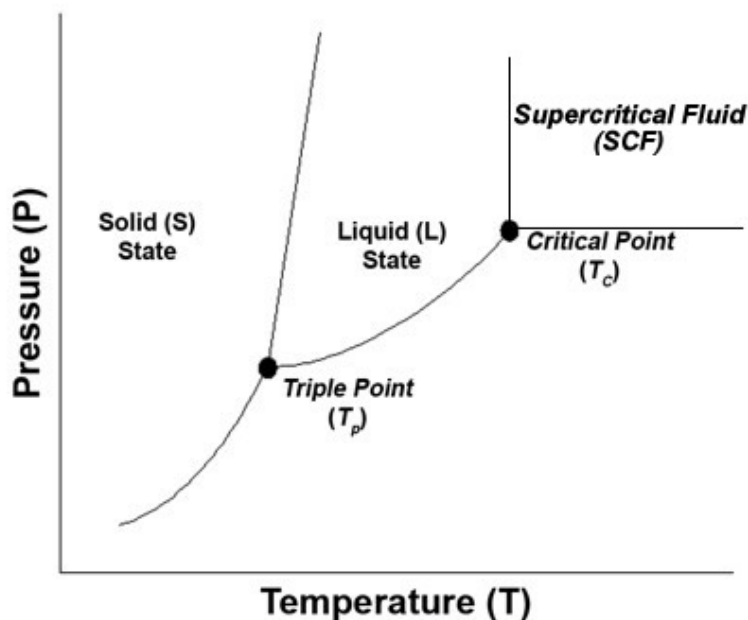


Figure 3.3: Phase diagram showing the supercritical fluid (SCF) region [7].

solvent to the reactants and ligands to be used. Still, due to the infrastructure needed to accomplish the other synthesis methods, chemical phase synthesis still would be considered to be the best method for manufacturing of nanoparticles if feasible.

3.1.3 Supercritical Fluid Synthesis

When a substance reaches both a temperature and pressure above the critical point, it becomes a supercritical fluid embodying both characteristics common to both a liquid and gas. The “fluid” becomes much more compressible than the gas and denser than the liquid. By manipulating the temperature and the pressure in the SCF region as can be seen in Figure 3.3, it is possible to tailor the properties of the supercritical fluid towards a gas or liquid. Near the critical point, small changes in pressure or temperature also result in large changes in density. These special properties are important as they can promote the dissolution of reactants which may otherwise be incompatible with the same solvent. The supercritical fluid is the reaction solvent and can also be tailored closer to a gas or liquid to allow the reaction to progress faster or slower for better control over the reaction. Therefore the need for often expensive or highly toxic organic solvents for the reactions can be eliminated.

The better control which a supercritical fluid can offer over the reaction kinetics such as faster dilution and depressurization with respect to a normal liquid can result in the nucleation of nanoparticles with tighter size distributions. Often supercritical

nanoparticle synthesis methods employ high pressure nozzles like in gas phase synthesis and use the quick vaporization of the fluid to form the nanoparticles, where nucleation had already occurred in the supercritical fluid (like in chemical synthesis). The most widely used gas for supercritical fluids application is carbon dioxide because of its moderate critical constants ($T_C = 31.1^\circ\text{C}$, $P_C = 72.8$ atm, $\rho_C = 0.47$ g/cm³), non-toxic nature, low cost and availability [41]. The problem with supercritical CO₂ is the insolubility of metal ions in it because of the charge neutralization requirement and the weak solute-solvent interactions. However this problem can be overcome by bonding the metal ions with organic ligands [41]. The methods used to produce nanoparticles with supercritical fluids can be divided in two main groups - physical and chemical. Physical procedures exploit variations in the physical parameters like temperature, pressure and volume, while chemical procedures make use of chemical reactions. The main disadvantage of this procedure is the more complex apparatus. Also there are a limited number of easily used and accessible supercritical fluid solvents when compared to the number of solvents which are available for chemical phase synthesis [41].

3.2 Germanium Nanoparticle Synthesis

There had been a large interest in the synthesis of germanium nanoparticles for the last decade. These papers have covered various different methods for synthesizing germanium nanoparticles from gas phase methods to chemical synthesis [8, 42–48]. Much of the original interest in germanium nanoparticles has shifted to other nanoparticle types such as PbSe and nanowires. The interest has been waning due to the difficulty in synthesis of viable and stable germanium nanoparticles with tight size distribution. Also the relative ease and increased ability of manipulation of germanium nanowires has steered a larger portion of interest toward these 1D structures [49, 50]. Devices such as thin-film transistors with germanium nanowires have been demonstrated with one of the chief problems with germanium, oxidation, dealt with by utilizing hydrochloric acid and hydrofluoric acid treatments prior to final functionalization of the wires and testing. Also, the nanowires can be in situ doped with boron during growth in the reaction furnace resulting in much higher conductivity and better mobilities. Such manipulations are very difficult to attempt with germanium nanoparticles and in many cases, has yet to be reported in literature due to this reason. Still, much interest in germanium nanoparticle production still exists due to their possible uses in communications and biological labels. Innovalight, a photovoltaic company based in Sunnyvale, CA, has also been experimenting with germanium nanoparticles for solar cells, though based on their technical reports, patents and media releases, is now solely focused on generation of silicon nanoparticles and stable colloidal inks utilizing them [51]. Innovalight's process is based on gas phase synthesis.

One of the chief challenges in the development of the PNTFT for this dissertation research lies with the synthesis of the germanium nanoparticles. As mentioned earlier in the introduction, a nanoparticle system would likely be the most sensitive and tunable for detection of the fluorescence from biological tags or functionalization for electromechanical detection of target analytes. Germanium is an ideal system due to the very high intrinsic mobility of the material - $1900 \frac{cm^2}{V \cdot s}$ for holes and $3900 \frac{cm^2}{V \cdot s}$ for electrons - and the well matched spectrum of germanium for absorption of visible and near-infrared wavelengths used in fluorescence imaging. The very large exciton Bohr radius of ~ 25 nm of germanium also greatly enhances the ability for carriers to tunnel between closely packed germanium nanoparticles [2]. Given all the advantages which make germanium nanoparticles an ideal system, there are two critical disadvantages as well.

The first is their rapid rate of oxidation, enhanced further by the fact that nanoparticles have such a high surface-to-volume ratio. Incomplete passivation results in the particles becoming mostly oxide. Germanium monoxide is unstable enough that it can sublime in ambient while germanium dioxide can be etched by moisture in the atmosphere. As the oxides are removed, more germanium oxidizes resulting in a cycle which causes the nanoparticle to be destroyed over time [52, 53]. Also germanium oxides generate many surface states which traps charges and prevent the carriers from tunneling from nanoparticle to nanoparticle [54, 55]. This is one the reasons germanium has not been the semiconductor of choice for transistors. The second is the relatively high temperatures needed for highly crystalline synthesis of germanium nanocrystals. While these temperatures, normally in excess of 270°C but less than 600°C , are below those necessary to deposit monocrystalline germanium layers on wafers in furnaces, they are still sufficiently high to be problematic for proper passivation of the germanium nanoparticles. Another problem which has been partially addressed is getting a tight size distribution ($\leq \pm 10\%$) over the synthesized germanium nanocrystals. These issues will be discussed and addressed in the research performed for this dissertation below.

3.2.1 Synthesis Method I - Gas Phase Synthesis

In order to develop nanoparticle transistors and devices, a collaboration was set-up originally between the Pisano group at University of California, Berkeley and the Stoldt Group at University of Colorado. This collaboration was set-up so the focus of this dissertation would be on development of the transistor devices rather than the synthesis of the nanoparticles needed for the active layer of the TFT. Germanium nanoparticles 10 nm in diameter were synthesized by ultrasonic aerosol pyrolysis by the Stoldt group [8]. Tetrapropylgermane and toluene was nebulized by a 1.7 MHz ultrasonic transducer. This gaseous mixture was then transported by the carrier gas, argon, through a three zone furnace (700°C , 700°C and 350°C) where the nanocryst-

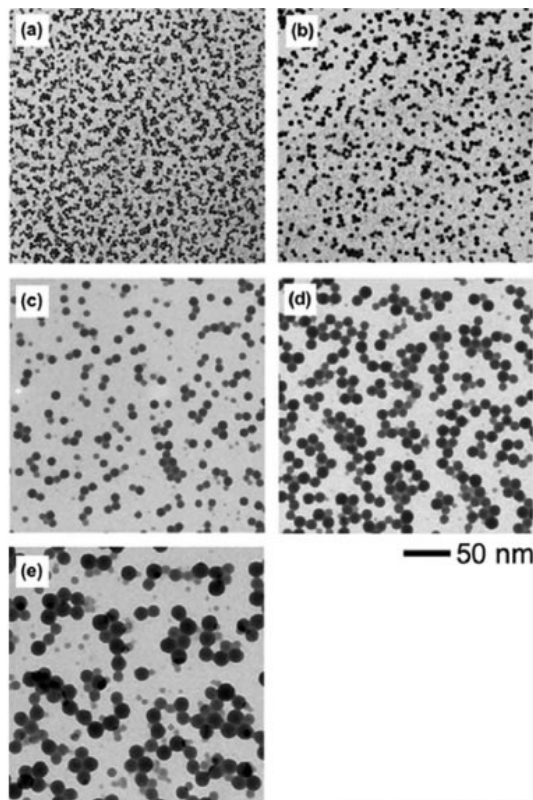


Figure 3.4: Representative TEM images of Ge NCs with mean diameters of a) 3.1 ± 0.4 nm, b) 4.0 ± 0.6 nm, c) 7.0 ± 1.6 nm, d) 9.7 ± 2.0 nm, and e) 11.1 ± 3.6 nm synthesized at 700°C from 25, 35, 45, 55, and $65 \mu\text{L}$ of tetrapropylgermane per 100 mL of toluene, respectively. [8]

tals were formed and then cooled. The resulting nanoparticles were then carried into a bubbler and suspended primarily into trichloroethylene. The process leads to diamond cubic germanium nanoparticles which can also be collected in various other anhydrous solvents such as tetrahydrofuran, toluene and chloroform. The germanium nanoparticles to be used in the transistor devices were collected in a toluene solvent at a concentration of approximately 1 M. This stock solution was the starting point for the nanocomposite synthesis performed at UC Berkeley.

One of the greatest difficulties working with semiconductor nanoparticles which are not metal oxides are their increased propensity for oxidation. This is due to their large surface-to-volume ratio which, combined with their oxidized form being their most stable state in ambient environments, can result in oxidation of the particles within a matter of seconds to minutes upon exposure to oxygen or water. This effect has been observed with multiple nanoparticles in the past [56, 57]. While the germanium nanoparticles can develop an oxide shell to protect them against further

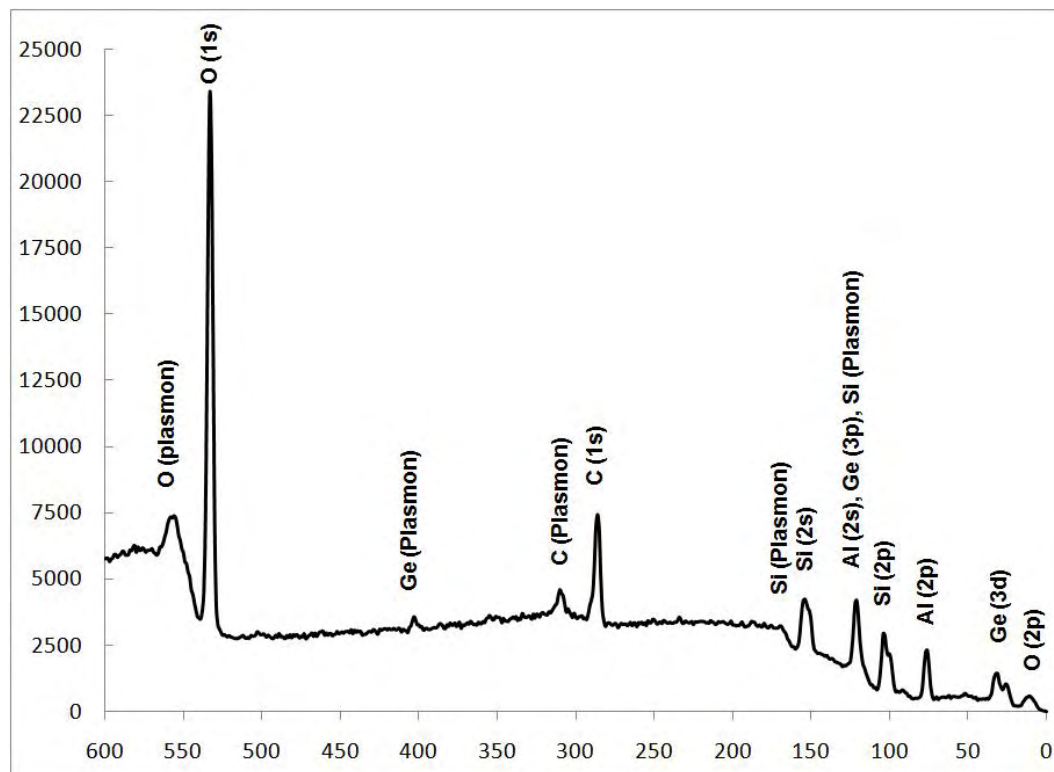


Figure 3.5: X-ray photoelectron spectroscopy (XPS) spectrum of the 10 nm germanium nanoparticles provided by University of Colorado, deposited onto a test die with silicon and aluminum on the surface. Oxygen plasma was used to etch away the carbon contaminant on the nanoparticles. As can be seen from the spectrum, the germanium 3d peak was split into two with the larger intensity peak at higher binding energy. A high resolution scan of the 3d peak showed that the crystals were 65 % germanium dioxide and 35 % germanium.

oxidation, the oxide itself is permeable to moisture such that in a highly oxidizing environment like buffered acetic acid or other aqueous solvents used in biology, the oxide shell is consumed by the water allowing the full erosion of the particle [58]. Therefore passivation and adequate protection of the germanium particle surface is very important. Even a second shell of a more stable element may not be sufficient as shown in Franzl *et al.* with CdTe and ZnS [56]. To address this problem, often hydrophobic acids are utilized such as oleic acid. Such chemistries are not often stable, which can lead to stripping of the oleic acid from the particle surface and allowing the particle to oxidize. Ligands such as oleic acid and trioctylphosphine oxide (TOPO) can also eventually break down due to oxidation.

Thiolation of particles has proven to be a good method to passivate the surface of the nanoparticles. This is due to the stable, covalent bonding of the sulfur to the par-

ticle element (in this case germanium). There have been demonstrations of relatively successful thiolation of germanium nanowires where oxide formation was suppressed for a full day [49]. Unfortunately, even thiolation is often not adequately stable resulting in incomplete passivation or loss of the ligand coat over time. This has been determined in literature where thiolation was used to passivate germanium surfaces for microelectromechanical devices [59]. Unlike germanium nanowire passivation, the ligands are necessary during the formation of the nanoparticles as well which requires the bonding and the ligand itself to be robust against the synthesis temperatures and solvents. This is likely the reason why there has yet to be a successful demonstration in literature of thiolated, highly crystalline germanium nanoparticles where oxidation has been largely to totally suppressed for more than several minutes in an ambient environment. While a hydrogel polymer may present a good scaffold and capping layer for the nanoparticles, the majority of these polymers are moderately to very polar thus making them insoluble in anhydrous, nonpolar solvents. For robustness and biocompatibility, a hydrogel polymer such as chitosan would be an ideal candidate. However, due to the insolubility of the chitosan in anhydrous, nonpolar solvents and the high oxidation rate of germanium nanoparticles in water and buffered acids, a compromise is necessary in order to achieve stable capping of the germanium nanoparticles.

A process was developed to convert chitosan into a slightly more nonpolar form so it could be dissolved in anhydrous, slightly nonpolar solutions for capping the nanoparticles. Chitosan was functionalized with deoxycholic acid by reacting both in the presence of L-Cysteine methyl ester hydrochloride. The deoxycholic acid group is much more hydrophobic resulting in a molecule which can be dissolved in anhydrous methanol. The solubility however was not great as dissolution of the chitosan was only 0.1 % w/v at best. Unfortunately, even methanol was too polar to be a solvent for the germanium nanoparticles, which were not supposed to have any organic coating. Additionally, methanol is often used to precipitate nanoparticles from solvents and depending on the bonding between the ligands and nanoparticles, sufficient to strip the ligands from the nanoparticles. Thus this process was deemed unusable. Dimethyl formaldehyde (DMF), a polar organic solvent, was also considered towards the end of the dissertation research, however there was insufficient time to investigate the usage of this solvent for the functionalization of chitosan onto germanium nanoparticles. Also, alternatives to chitosan were already available such that this research path was left for possible future investigation.

As was mentioned earlier, germanium nanoparticles are highly reactive. Additionally, these particles were being formed in gaseous form at high temperatures, cooled in a 350°C zone prior to being bubbled into an organic solvent for storage. Organic solvents can denature at fairly low temperatures due to their low melting and boiling points. By transferring hot particles into the solvent we surmised that the solvent around the particles was denatured. Toluene has a boiling point of 110°C while

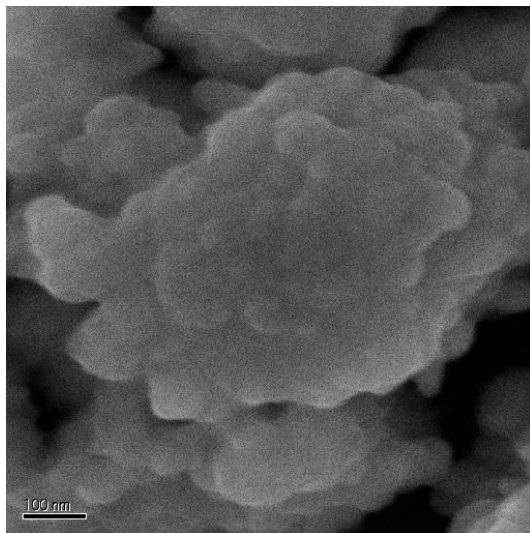


Figure 3.6: Germanium nanoparticles from University of Colorado agglomerated and embedded in a carbon coating.

trichloroethylene, the solvent of choice for this method, has a boiling point of 86°C . While the particles observed in Figure 3.4 were seemingly free of contamination and monodisperse, this was not the case with particles that were acquired for the device research. The particles received for the device research were agglomerated, embedded and coated with a thick coat of carbon. After partial oxygen plasma etching the particles can be observed using SEM as can be seen in Figure 3.6.

The only viable method for removing the carbon contamination was oxygen plasma. This was problematic as it would oxidize the particles as was seen in Figure 3.5. Also, the carbon contamination was extensive enough such that oxygen plasma was insufficient to remove all the carbon without completely eroding the particles. The fact that without oxygen plasma etching, the carbon contamination was sufficient to suppress all of the germanium signal in the XPS scans taken showed that the carbon coating the nanoparticles was thicker than 10 nm. The particles, when bubbled into the organic solvent, did not yet have a passivation layer. During transfer of the particles, as soon as the solvent was exposed to some oxygen, the particles would oxidize. As the transfer was several days after the synthesis of the particles and the transfer itself took at least a day, there was ample time for oxygen to diffuse into the solvent and oxidize the nanoparticles. The theory behind the carbon contamination was based on both the high reactivity of the unpassified germanium nanoparticles and the fact that denatured solvent had an opportunity to accumulate around the particles. Since the particles themselves had no ligand coat, while initially after synthesis they might be monodisperse, after an hour or more the particles likely would have started to agglomerate in an effort to lower the energy of the system due to the large amount

of nanocrystal surface exposed. Finally, the carbon contamination, which was much more apparent at higher particle concentrations, prevented any further passivation of the particle surfaces and also prevented transduction of carriers in a semiconductor device.

Though it was verified that the particles, at least originally, were germanium and had a relatively tight size distribution, the oxidation, carbon build-up and lack of passivation problems no longer made the procured particles viable for semiconductor devices. It was also viewed later in the TEM images that the size distributions were actually larger than the ones reported as can be seen in Figure 3.4. Due to these factors, a decision was made to perform synthesis of the nanoparticles in the lab at Berkeley. Therefore the next step was to determine which synthesis methods would be most conducive to producing viable particles and setting up a nanoparticle synthesis laboratory to perform the required chemistry and reactions.

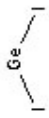
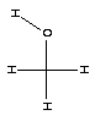
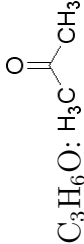
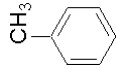
3.2.2 Synthesis Method II - Batch Chemical Synthesis

After much investigation of different methods, chemical synthesis was chosen. This was due to a combination of known chemicals and proper solvents available for synthesis of germanium nanoparticles and reduced complexity around the infrastructure required. The eventual goal of the dissertation research was to produce a nanoparticle transistor sensor that would have high sensitivity and selectivity, but would still lend itself to bulk manufacturing methods and be of lower costs to match the requirements of the IPSMS system. Therefore chemical synthesis methods were still the most logical route.

Germanium nanoparticles are highly reactive so solution synthesis methods are quite complex and must be performed in an inert atmosphere or vacuum. Once out of the inert atmosphere, due to incomplete or weak functionalization, the particles quickly oxidize. Commonly used ligands such as R-amines (where R is normally a carbon chain which could have additional functionalizations), TOPO and oleic acid do not provide proper passivation or no passivation at all for germanium nanoparticles. To achieve stronger bonding, two covalent bonding surface passivations were explored: 1) Thiolation and 2) Alkyl-functionalization.

There is a large body of knowledge around thiolation of nanoparticles, due mostly to its use for passivation of widely produced and utilized gold and silver nanoparticles. Thiol chemistries often have great success though it has been suggested multiple times in literature that the Ge-S bond may be weaker than the Ge-C bond [59, 60]. There are also published accounts of thiols providing better passivation and even one published account that suggested the Ge-S bond has a bonding energy of 534 kJ/mole while the Ge-C bond only has a bonding energy of 460 kJ/mole [49, 61]. Therefore it is currently unknown which functionalization may be stronger. However, regardless of which bonding may be stronger, there have also been published accounts of thiols

Table 3.1: Chemical Properties of Synthesis Precursors and Solvents [9]

Chemical	Molecular Weight (g/mol)	Density (g/mL @ 25°C)	Boiling Point (°C)	Melting Point (°C)	Vapor Density/Pressure	Structure
GeI₂ (≥ 99.9 %) (Germanium diiodide)	326.45	5.37	-	-	-	
Hexadecylamine (HDA) (98 %)	241.46	-	330	43-45	< 1 mmHg (20°C)	C ₁₆ H ₃₅ N: 
N-Butyllithium (Butyllithium solution in 1.6 M hexane solution)	64.055	0.68	-	-	-	C ₄ H ₉ Li: 
1-octadecene	252.48	0.789	179 @ 15°C	14-16	0.71 (vs air)	C ₁₈ H ₃₆ : 
Methanol	32.04	0.791	64.7	-98	1.11 (vs air)/410 mmHg (50°C), 97.68 mmHg (20°C)	CH ₄ O: 
Acetone (99.5 %)	58.0791	0.791	56 @ 76 mmHg	94	2 (vs air)/184 mmHg (20°C)	C ₃ H ₆ O: 
Toluene	92.14	0.865	110-111	-93	3.2 (vs air)/22 mmHg (20°C), 26 mmHg (25°C)	C ₇ H ₈ : 

undergoing photocatalytic oxidation to disulfides [62, 63]. This may explain why the Ge-S bond may have been observed to be stronger in some cases, but weaker in others. Since one of the applications is for the nanoparticles to be part of the photodetection mechanism of the PNTFT, this weakness of thiol ligands makes them unsuitable, even if the thiols can impart equivalent or even better passivation than other ligands during and directly preceding the synthesis. Therefore focus was placed on finding a suitable alkyl-functionalization and method.

There have been multiple published accounts of alkyl functionalization of germanium [43, 44, 49, 50, 63]. The two most effective methods for alkyl functionalization are Grignard reactions and hydrogermylation. Grignard reactions attach alkyl groups to chloride-terminated surfaces while hydrogermylation attaches alkyl groups to hydride-terminated surfaces. A recently published method by Lee *et al.* from Los Alamos National Laboratories provided insights to creating ambient stable germanium nanoparticles. By using a combination of reduction and hydrogermylation they managed to synthesize crystalline germanium nanoparticles with long term ambient stability [64]. This method served as a starting point for the synthesis methods employed for the dissertation research.

3.2.3 Initial Synthesis Protocol

The first stage was to create nanoparticles 10 nm or less in diameter using the method explained in the paper by Lee *et al.* The materials used in the synthesis and their properties are listed in Table 3.1. To synthesize the first batch of nanoparticles (~4 nm according to the paper by Lee *et al.*), the protocol developed by Lee *et al.* was utilized with minor changes to the apparatus and procedure was used:

1. Purge the glovebox down to < 1 ppm O₂ and < 1 ppm of H₂O. The oxygen levels and moisture levels should be kept below 5 ppm during entire run, preferably below 1 ppm. Dry all glassware, stir bars, etc.
2. Place 3 g of hexadecylamine (HDA) into a 25 mL beaker and heat to 200°C on a digital hotplate. Ensure that the fume extractor is in place on top of the beaker to draw away the HDA fumes. Otherwise the HDA will condense on the walls of the glovebox chamber.
3. Add in 0.2 g of GeI₂. Wait for it to dissolve. The solution should first turn a pale yellow and then turn gray. Swirl beaker to help stir and dissolve the GeI₂. The GeI₂ will not dissolve in the HDA below 200°C.
4. Dilute N-Butyllithium (0.8 mL of a 1.6 M hexane solution)(BuLi) with 3 mL of 1-octadecene (ODE) in a 10 mL beaker. Using a glass pipette, inject the N-Butyllithium/ODE mixture into the HDA/GeI₂ solution. Swirl and keep at

200°C for five minutes to allow dissolution. Then further heat to 300°C. Once at 300°C, allow to heat for one hour. The grayish solution should start to give off lots of white vapor and turn black.

5. Turn off the hotplate and allow the solution to cool to 100°C. Add an equal volume of methanol to precipitate the nanocrystals. The solution should turn into a grayish sludge. Transfer the sludge into several centrifuge tubes. Remove the centrifuge tubes from the glovebox and place into centrifuge in ambient. Centrifuge to separate out particles from supernatant. Draw away as much supernatant as possible.
6. Redissolve the precipitate into toluene. Add an equal volume of 50 % acetone/50 % methanol. Allow nanocrystals to precipitate. Centrifuge solution to separate out particles from supernatant. The particles should precipitate as a black powder to the bottom of the centrifuge tube. The supernatant should be clear to a pale yellow hue. Draw away as much supernatant as possible. Dry if possible. Repeat 3 more times. This procedure removes the residual HDA, unreacted reactants and contaminant byproducts.
7. For the final colloid, redissolve the precipitate into toluene. Aim for at least a 1 % solution. Store the final nanoparticle colloid in the glovebox.

Also a synthesis run to get ~ 6.5 nm nanocrystals in diameter was also attempted. In order to get particles of this size, the amount of the initial precursor GeI_2 used was increased by 5 times. The amount of HDA utilized was doubled (as HDA was the solvent) and the amount of ODE and BuLi was kept the same.

GeI_2 was soluble in HDA once temperatures of 200°C were reached. Germanium compounds have limited solubility in other organic solvents (trioctylamine, dioxane, ODE, and trioctylphosphine (TOP)) which was part of the reason behind poor synthesis of germanium nanocrystals using those solvents [64]. This list of large, bulky solvents encompasses the limited list capable of dissolution of the reactants needed for germanium synthesis and taking the high temperatures used in the synthesis. The other special characteristic of this reaction was the use of BuLi. Other strong reducing agents needed for the germanium synthesis reaction had been attempted in prior literature. The poorly soluble reducing agent LiAlH_4 , which has been utilized with closely-related reducing agents in other germanium nanocrystal synthesis methods resulted in low-quality nanocrystals (NCs) with poor solubility [43, 64]. The higher solubility of BuLi is due to its organometallic nature and higher reactivity since once the ligands are stripped, it is highly reactive lithium rather than a lithium compound. Lee *et al.* also found that the use of ODE as a ligand, rather than as a solvent, resulted in much higher quality NCs with better passivation, especially in ambient conditions. By adding ODE at 200°C, the photoluminescence (PL) quantum yield of the NCs was improved greatly relative to other capping ligands such as TOP-capped NCs [43, 64].

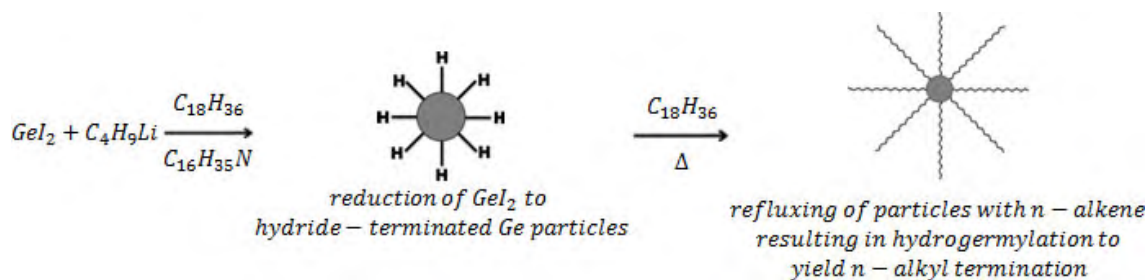


Figure 3.7: Reaction kinetics of germanium nanoparticle synthesis

The germanium particles were covalently bonded to the octadecyl ligands via a Ge-C bond. This strong bonding combined with very good functionalization of the surface with the fairly stable octadecyl ligands resulted in good resistance of the particles to oxidation. While some of the reaction kinetics were known in the paper by Lee *et al.*, size control and surface chemistry were not understood yet. What was known was the higher temperature (300°C) used during the synthesis ensured highly crystalline, cubic germanium nanocrystals were formed. The known reaction kinetics have been depicted in Figure 3.7. The 18 carbon chain, being so long, also assisted the stability of the particles in solution and helped to monodisperse them. The long chain also provided higher resistance to solvents like acetone and methanol, which were used in precipitation and wash. Theoretically, based on C-C bond length of 154 pm and assuming that the bond angles were around 109.5°, then a rough overall ligand length could be calculated to be about 2.138 nm. Therefore the interparticle spacing should be under 5 nm, which was far below the exciton Bohr radius of germanium. This factor combined with little to no oxidation would in theory allow conduction of the carriers between the particles as in the paper by Talapin *et al.* [2]. In order to understand the reaction kinetics and characterize the nanoparticles, the particles were then characterized by an ensemble of methods from electron microscopy to x-ray techniques. The paper by Lee *et al.* only presented initial results with little to no characterization of the oxidation of the particles synthesized and a cursory explanation of the reaction kinetics. In order to produce germanium nanocrystals of quality sufficient for electronic devices, a wide range of experiments to determine the details behind the reaction kinetics and a new, improved hydrogermylation protocol needed to be created.

3.2.3.1 Characterization of the Initial Synthesized Nanoparticles

Multiple characteristics of the particles needed to be determined prior to using them in the transistors. These characteristics were size, composition, crystallinity and level of passivation. Transmission electron microscopy (TEM) utilizes highly focused electron beams and measure their scatter and transmission through a fairly

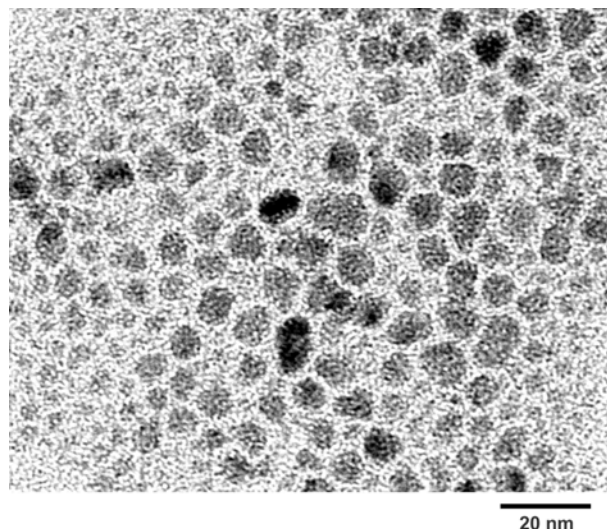


Figure 3.8: TEM image of the 7 nm germanium nanoparticles synthesized.

sparse, thin layer of the sample usually less than 50 to 100 nm thick. TEM provides mainly size information for nanoparticles and has been used for this purpose in regards to the dissertation research. TEM can be also used for selected area diffraction to determine the base composition and crystallinity of the nanoparticles. Due to the availability of wide-angle x-ray scattering (WAXS), this function of the TEM was not used. Images of both initial batches of the nanoparticles were taken. Due to the availability of small-angle x-ray scattering (SAXS), the TEM images were mainly used to determine the dispersity of the particles in the films and the length of the ligands. A TEM image of the 7 nm germanium nanoparticles synthesized in the initial batch can be seen in Figure 3.8. From this and several other TEM images of the 7 nm and 3 nm germanium nanoparticles, the ODE ligand length was determined to be 7.85 \AA . Also, the image shows the high monodispersity of the nanoparticles. There was definitely a moderately large size distribution, much larger for the 7 nm particles, around $\pm 2 \text{ nm}$ in diameter. For the 3 nm particles, the size distribution was much smaller around 5 \AA . The particles were spherical in nature with a close packed structure. SAXS measurements were used instead of counting a large quantity of nanoparticles to more accurately determine the size distribution of the nanoparticles.

To determine the size distribution of the particles, SAXS was used. SAXS is a technique which utilizes a focused beam of high energy x-rays from a synchrotron source and measures the scatter of the x-rays as they pass through a sample. The SAXS setup utilized was located at Beamline 7.3.3 at Advanced Light Source (ALS), Lawrence Berkeley National Laboratory (LBNL). The samples were deposited through drop-casting on 100 nm thick mica films which are amorphous and highly transparent to the x-rays. These samples were placed in the path of the beam in front of tube (left



Figure 3.9: SAXS setup at Beamline 7.3.3, ALS, LBNL.

side in image) before the detector which can be seen in Figure 3.9. The scatter was measured using a high resolution 2D detector which can be seen at the end of the tube (right side of image). SAXS can be used to determine the hydrodynamic diameter of particles or the diameter of the particles and capping ligand combined. Also, due to the beam size, a much larger area can be scanned and thousands of nanoparticles can be scanned at the same time resulting in a much quicker and often more accurate particle size measurement than TEM.

SAXS scans were taken of the nanoparticles synthesized. Figure 3.10 shows the original SAXS spectrum, the peak fit and the final adjusted size distribution for the 3 nm particles synthesized taking into account the ligand length. The hydrodynamic diameter (ligand + particle) of the 3 nm particles was 4.32 nm. The actual diameter was $4.32 \text{ nm} - 1.57 \text{ nm} = 2.75 \text{ nm}$. The hydrodynamic range was 3.74 nm (small side) and 5.12 nm (large side). Therefore the particles were $2.75 \pm 0.69 \text{ nm}$. There also existed a small percentage of larger particles as well. These larger particles had a hydrodynamic diameter of 9.92 nm. Therefore the particles were actually 8.35 nm in diameter. The hydrodynamic range was 8.49 nm to 11.95 nm. Therefore these larger particles were $8.35 \pm 1.73 \text{ nm}$. Using a peak fit (Lorentzian), the ratio of the peaks was found to be 27.8 : 1. Therefore 96.5 % of particles were $2.75 \pm 0.69 \text{ nm}$ in diameter and 3.5 % were $8.35 \pm 1.73 \text{ nm}$ in diameter.

A larger batch of nanoparticles was synthesized as well. Figure 3.11 shows the original SAXS spectrum, the peak fit and the final adjusted size distribution taking into account the ligand length for the 7 nm nanoparticles synthesized. The hydrodynamic diameter (ligand + particle) of the 7 nm particles was 8.54 nm. Thus the actual diameter was $8.54 \text{ nm} - 1.57 \text{ nm} = 6.97 \text{ nm}$. The hydrodynamic range was 7.00 nm (small side) and 10.95 nm (large side). Therefore the particles were $6.97 \pm 1.98 \text{ nm}$. There also existed a smaller percentage of larger particles as well. These smaller particles had a hydrodynamic diameter of 5.23 nm. Therefore the particles were actually

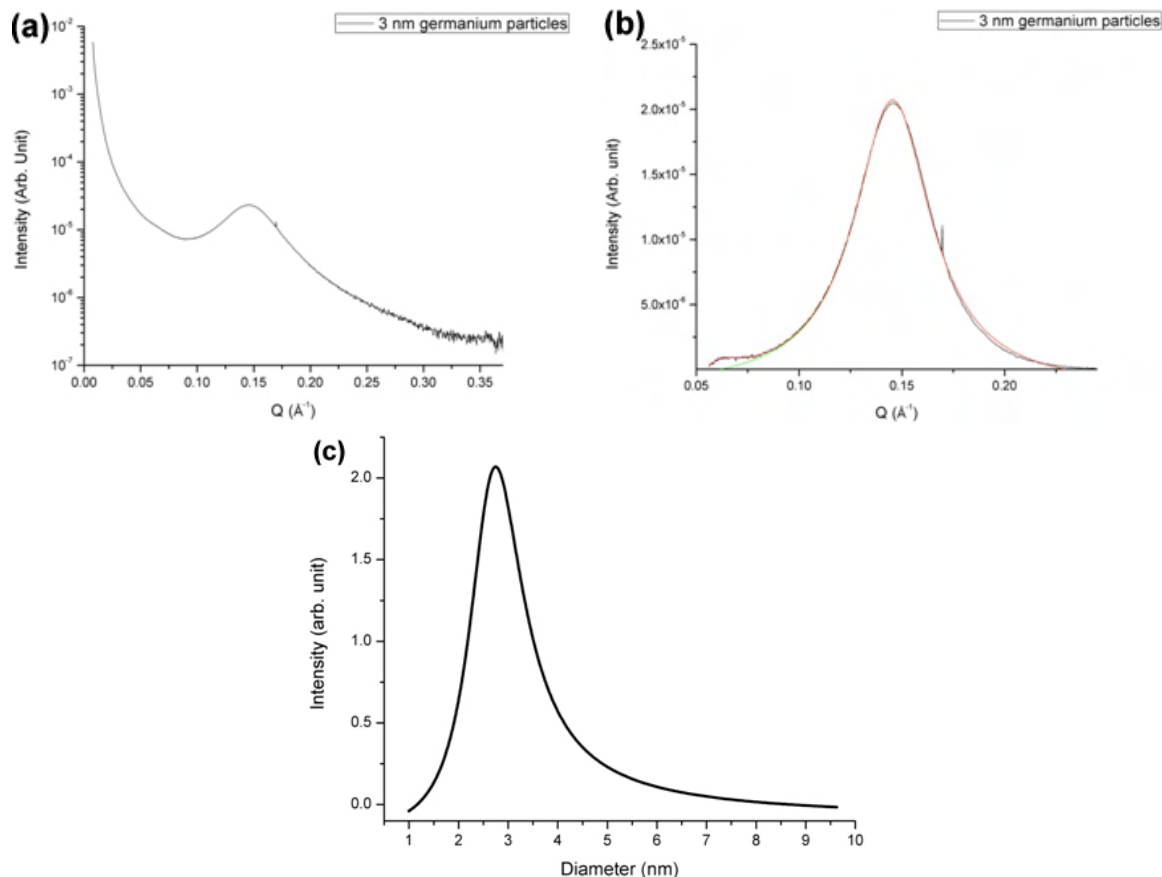


Figure 3.10: a) SAXS spectrum of the 3 nm germanium nanoparticles b) Peak fit for the 3 nm germanium nanoparticles c) Size distribution of the 3 nm germanium nanoparticles

3.66 nm in diameter. The hydrodynamic range was 4.31 nm to 6.65 nm. Therefore these smaller particles were 3.66 ± 1.17 nm. Using a peak fit (Gaussian), the ratio of the peaks was found to be 1.43 : 1. Therefore 58.8 % of these larger batch of particles were 6.97 ± 1.98 nm in diameter and 41.1 % were 3.66 ± 1.17 nm in diameter according to the SAXS plots. SAXS can also be utilized to determine the geometry of the nanoparticles. However, TEM was used to determine geometry of the particles and so the SAXS plots were not further interpreted for geometry information.

In order to determine crystallinity of the nanocrystals and confirm the type of nanoparticles, wide-angle x-ray scattering was used (WAXS). Since the Q range observed was relatively high, the WAXS spectrum plotted could be classified as x-ray diffraction. However, due to the high energy x-rays and focused beam, nanocrystals with diameter below 10 nm can be seen much more clearly than with a benchtop system. Very similar to a SAXS measurement, the main difference is the placement

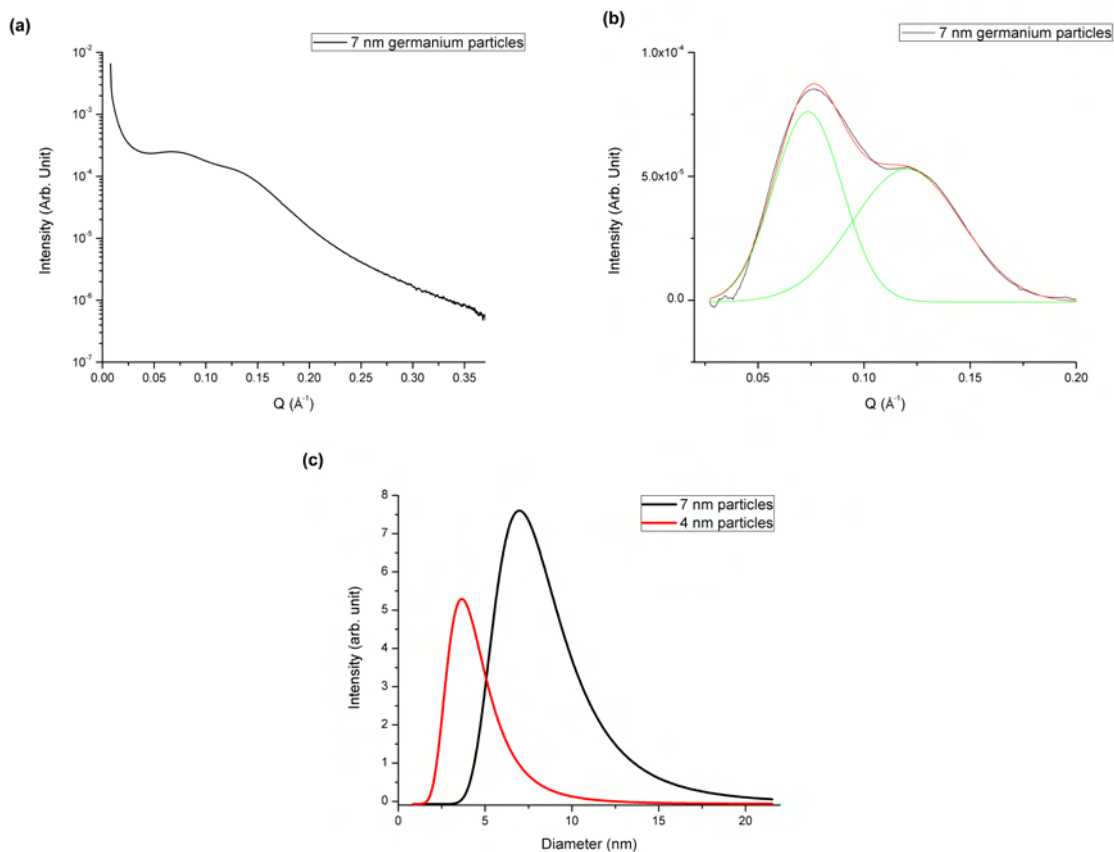


Figure 3.11: a) SAXS spectrum of the 7 nm germanium nanoparticles b) Peak fit for the 7 nm germanium nanoparticles c) Size distribution of the 7 nm germanium nanoparticles

of the detector right above the sample, as can be seen in Figure 3.12, allowing much higher Q values to be observed. This 2D plot, due to its symmetry, can be made into a 1D spectrum which shows peaks corresponding to specific elements. Germanium has several specific crystalline peaks according to its crystalline indexes used for its identification. These peaks can be found in Table 3.2. From these peaks, the crystalline structure can be determined as well as the size of the nanoparticles from the full width half maximum of the peaks.

WAXS spectrums of the 7 and 4 nm particles were taken 6 and 22 days after synthesis. A WAXS spectrum of the particles can be seen in Figure 3.13. A WAXS spectrum of oxidized particles can also be seen in the figure. The oxidized particles have many more peaks due to the oxide formed. The Q -range recorded only encompassed the $\langle 111 \rangle$, $\langle 220 \rangle$, $\langle 113 \rangle$ and $\langle 400 \rangle$ peaks. However this was sufficient to determine the germanium nanocrystals were indeed crystalline and cubic in struc-

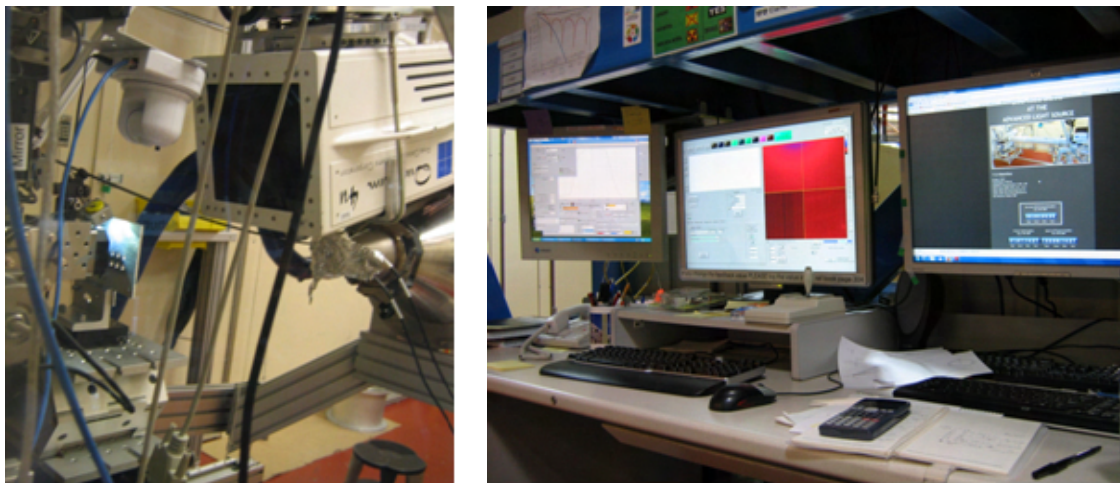


Figure 3.12: WAXS setup at Beamline 7.3.3, ALS, LBNL. The detector situated right above the sample can be seen above right, while the computer set-up used for data collection and interpretation of the raw data can be seen in the image above right.

Table 3.2: Germanium WAXS peaks

Index	$\langle hkl \rangle$	d (Å)	Q (Å ⁻¹)	Intensity (%)
111		3.2663	1.924	100
220		2.0002	3.141	73.8
113		1.7058	3.683	44.1
400		1.4143	4.443	11.5
331		1.2979	4.841	17.0

ture. Since size had already been determined utilizing SAXS and TEM, it was not measured from the WAXS spectrum. With size, type and crystallinity determined, a very sensitive measurement of the composition was still needed.

To determine the composition of the nanoparticles, x-ray photoelectron spectroscopy (XPS) was utilized. This technique utilizes an x-ray beam and measures the photoelectrons generated due to exposure of the material to the x-rays. The photoelectrons are generated by x-rays colliding and as a result, ejecting electrons from the orbitals of the elements being probed. The higher the orbital, the lower the binding energy of the electron. Unlike SAXS and WAXS, XPS is a soft x-ray technique using soft x-rays about 1500 eV. The intensity of the x-rays also do not need to be as high since they do not need to penetrate through the sample. It is a very sensitive surface technique as the escape depth of the photoelectrons is normally very shallow on the order of 10 nm or less. This works very well for the nanoparticles since they are also in this size range. Due to the very specific binding energies of different substances, very accurate measurements of the composition of the material

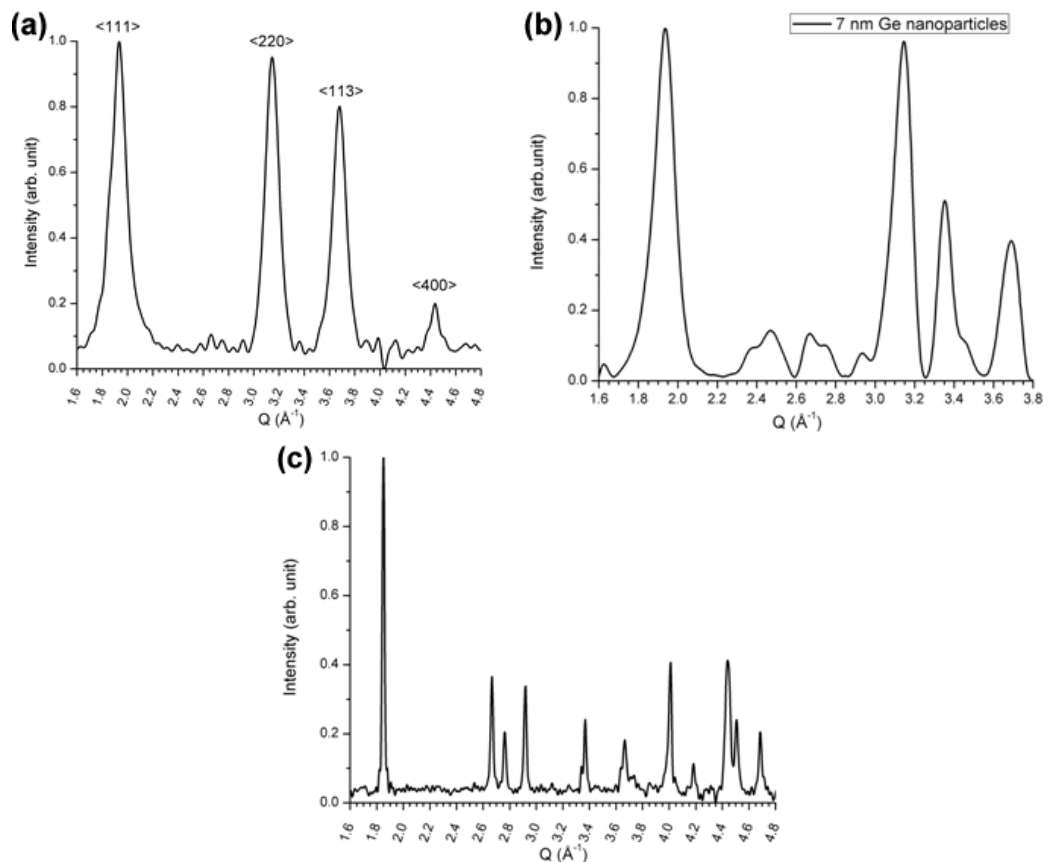


Figure 3.13: WAXS (more specifically x-ray diffraction) spectrum of the 7 nm germanium nanoparticles after a) 6 days in ambient and b) after 22 days in ambient. c) WAXS spectrum of oxidized 3 nm germanium nanocrystals. These nanocrystals were kept 22 days in ambient before being oxidized by removal of their ligand coats by ion bombardment (from an ion gun) and oxygen plasma treatment.

and the chemical state of the elements in it can be made without destroying the sample, unlike mass spectroscopy. The technique also requires that the substrate on which the sample has been deposited be at least a poor conductor. Therefore p-type silicon was used as the substrate as opposed to alumina or glass.

To determine the elements present in the sample, a wide range survey spectrum was taken of the germanium nanoparticle samples. The survey spectrum for the 7 nm germanium nanoparticles can be seen in Figure 3.14. Germanium, carbon, silicon and oxygen were present in the sample. Due to charging of the substrate and sample, the baseline was not flat. Two XPS machines were utilized for the XPS scans. The first was an older SSI S-Probe Monochromatized XPS Spectrometer, which uses Al(K_α) radiation (1486.6 eV) as a probe. The second was a PHI Quantum 2000

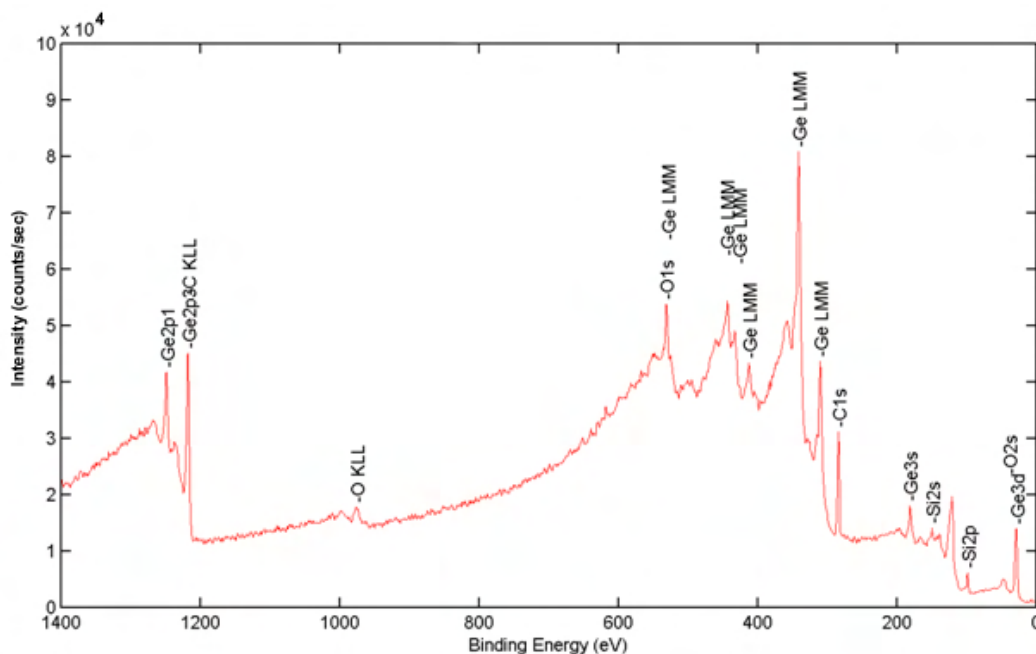


Figure 3.14: XPS survey spectrum of the 7 nm germanium nanoparticles.

scanning microprobe spectrometer, which uses $\text{Al}(K_\alpha)$ line radiation as well. The PHI machine has much higher sensitivity than the SSI machine, however, due to higher accessibility of the SSI, it was utilized for several scans when such high sensitivity was not necessary. For the majority of the germanium nanoparticle scans, the PHI machine was utilized as the ligand coat often completely suppressed the germanium signal.

To determine the chemical state of the germanium and especially determine if any oxides had formed on the surface of the nanoparticle, high resolution scans around the two principle germanium XPS peaks - $3d$ and $2p^{3/2}$ - were taken. The $3d$ peak, due to the low binding energy around 29 eV, gave a better determination of the composition of the bulk of the nanoparticle. The $2p^{3/2}$ peak, due to the high binding energy around 1218 eV, gave a much more surface sensitive composition. This allowed determination of very small amounts of oxide and even different forms of oxides formed on germanium (germanium dioxide and germanium monoxide) which the $3d$ peak scan may not show. Furthermore, the ion sputtering function of the PHI XPS machine was utilized to determine the depth profile of the nanoparticles. This gave the approximate thickness of the germanium oxides and ligand layer on the surface for the germanium nanoparticles. In order to perform a proper sputter profile, a monolayer of the germanium nanoparticles from a very dilute solution (<0.1 mM) were drop-casted onto the substrate and allowed to dry. The sample was then loaded

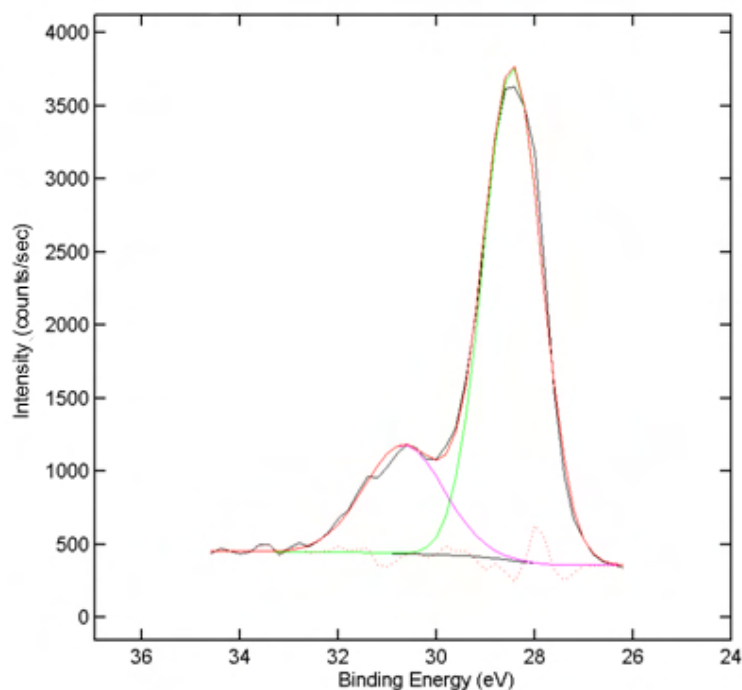


Figure 3.15: High resolution spectrum of the 3d peak of the 7 nm germanium nanoparticles.

into the XPS machine. Short sputtering bursts of six seconds were used to sputter the exposed upper surface of the particles away. Between sputtering bursts, the XPS machine recorded the spectrum around the two principle germanium XPS peaks. The sputter profile of the 7 nm germanium nanoparticles is shown in Figure 3.16.

The 3d peak of germanium was tracked during the sputtering due to the better escape depth of the photons compared (want more bulk sensitivity than surface sensitivity and thus the $2p_{3/2}$ peak was not used). The left plot shows the peak energies for both Ge and GeO_2 during the sputtering to show the peaks did not shift and thus the sputter profile could be trusted. An energy of 0 eV represented a loss of signal for either molecule. To make the thickness estimate, the average particle size was used and assumed to linearly etch with time as assumed with sputter etch profiles during XPS measurements. The right plot depicts the area intensity of the molecules plotted against particle diameter to give an estimate for the thickness of the germanium dioxide formed on the surface of the nanoparticles. The first measurement showed much higher oxide concentration than the average across the sample. It was possible this section of the sample was much more oxidized to begin with or the ligands managed to sufficiently reduce the signal sufficiently to shadow the germanium signal. The latter was more likely to be true since the second reading showed a much higher con-

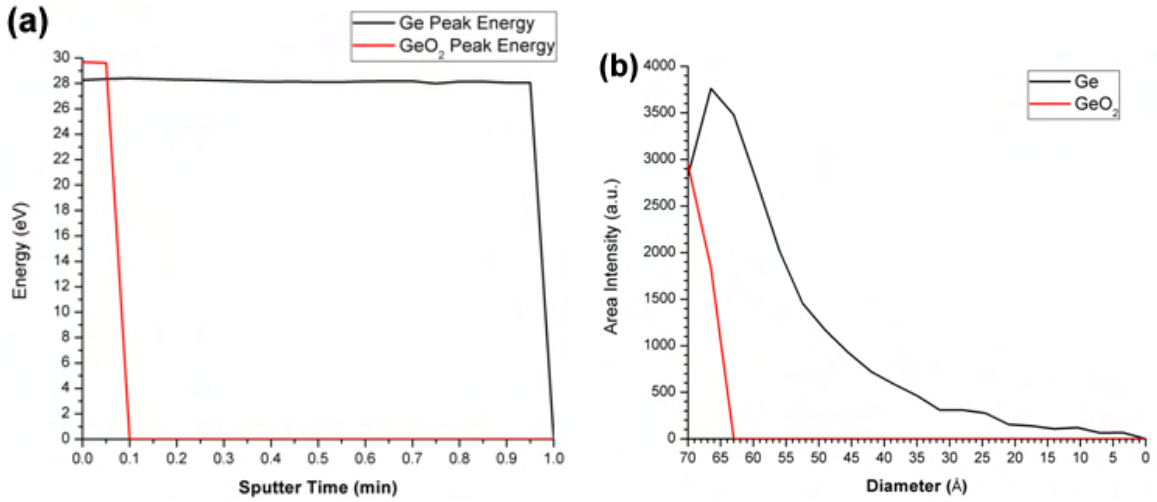


Figure 3.16: Sputter profile of the 7 nm germanium nanoparticles to determine the thickness of the germanium dioxide shell.

centration of germanium, which actually increased in overall area intensity meaning more germanium was present (it had been determined that the penetration depth of the x-rays was sufficient to penetrate into the silicon (50-100 nm) and the photons generated can escape the entire nanoparticle layer (escape depth was estimated to be around 12 nm). Since there was only a monolayer of germanium nanocrystals present, the ligands probably absorbed the escaping photons or shielded the crystal sufficiently to decrease sensitivity. Once the ligands were sputtered off, the germanium signal thus increased. This, however, did not compromise the oxide thickness measurement. Loss of germanium dioxide signal occurred around a particle diameter of 63 Å which suggested the oxide probably was 7 Å in thickness. The germanium monolayer was further sputtered until the germanium signal was lost meaning the monolayer had been fully sputtered away. Considering the intensity fell exponentially for the germanium signal, the sputtering was thus probably fairly linear as sensitivity for XPS drops exponentially as the layer gets atomically thin. The signal from a buried layer of atoms under a thickness τ is attenuated by $e^{-\tau/\lambda}$ where λ is the mean escape depth of the electrons generated by the x-rays. The escape depth λ can be defined as:

$$\lambda = \frac{\hbar\nu^2}{\omega_p e^2 l n \frac{2m\nu^2}{\hbar\omega_p}} \quad (3.2)$$

where ν is the velocity of the electron, m is the electron mass, $\omega_p = (\frac{4\pi e^2 n}{m})^{1/2}$ is the plasmon frequency and n is the electron density. Therefore the escape depth, being a function of electron energy and density, is relatively independent of the sample composition. Therefore the linear approximation was sufficient in the above mea-

Table 3.3: Chemical Properties of 1-Pentene [9]

Chemical	Molecular Weight (g/mol)	Density (g/mL @ 25°C)	Boiling Point (°C)	Vapor Density	Structure
1-pentene	70.13	0.641	29.9 - 30.1	2.4	C ₅ H ₁₀ 

surements. As the oxide is an impediment to the transduction of the electrons, the oxide layer needed to be reduced further in thickness. At 7 Å, considering the atomic radius of germanium is about 125 pm, the oxide layer is about 6 atoms thick. Overall, the composition of the nanoparticles was on average 77% Ge and 23% GeO₂. There was a small fraction of germanium monoxide, though this fraction became negligible, especially in samples older than twenty-four hours.

Through synthesis of the 3 nm germanium nanoparticles utilizing the initial protocol, it could be seen that the nanoparticles synthesized were indeed oxidation resistant. However, the SAXS measurements showed that the size distribution was not as tight as that mentioned by Lee *et al.* - ± 7 Å rather than ± 4 Å for a 2.75 nm in diameter particle - and there was still oxide formation [64]. From the formation of the 7 nm diameter particles, it was determined that the size distribution was mostly determined by the amount of initial germanium precursor rather than the amount of ODE. Since there was likely an insufficient amount of ODE added, the particles were divided into two different sizes - 6.97 and 3.66 nm particles. In Lee *et al.*, they mentioned the synthesis of one size of particle with larger size distribution through addition of 5 times the initial amount of GeI₂, BuLi and ODE precursors. As was seen in the experiments, complete passivation did not occur in the synthesis run. With the levels of oxidation observed, conduction between particles was unlikely though tests were still conducted to determine the properties of the nanocomposite film. These will be discussed in the following chapter.

3.2.4 1-Pentene Protocol

Some information about the reaction kinetics was determined from utilizing the protocol from Lee *et al.* However, in order to achieve carrier transport, oxidation needed to be reduced or eliminated, particle size and distribution needed to be better and passivation needed to improve. The next step to determining the reaction kinetics so a new hydrogermylation protocol could be developed was to utilize a shorter ligand from the same family as ODE. Regarding the use of hydrazine to improve conduction between PbSe nanoparticles, it was postulated by Talapin *et al.* that the interparticle spacing should be made less than 1 nm if possible [2]. In order to achieve such a small spacing, 1-pentene was chosen as the reaction precursor so the particles would gain a pentyl ligand coat.

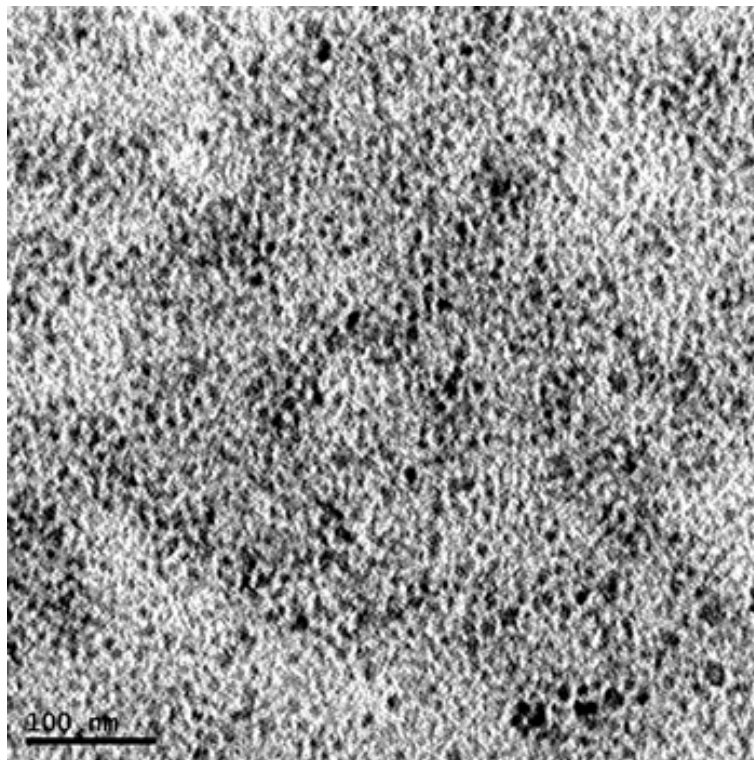


Figure 3.17: TEM image of 8 nm germanium nanoparticles synthesized using 1-pentene.

The reaction protocol was first run at lower temperatures due to 1-pentene's much lower boiling point of $\sim 30^{\circ}\text{C}$ as can be seen in Table 3.3. The first limitation to lowering the reaction temperatures was the dissolution limit of the GeI_2 . The temperature at which GeI_2 would dissolve into HDA was 180°C . However dissolution was much better at 200°C . The second had to do with the crystallinity of the germanium nanoparticles. Running the reaction at temperatures approaching or greater than 300°C increased the crystalline quality of the germanium nanoparticles as was determined in initial runs of this protocol and was supported by previous work performed in literature [42, 43, 47, 64]. Therefore dissolution of the GeI_2 and injection of the 1-pentene and BuLi was performed at 200°C . The solution was then raised to 300°C for an hour to react. The solution was then cooled and a 50/50 methanol/acetone wash was used to precipitate the nanoparticles and remove unwanted byproducts of the reaction (including the HDA solvent). The nanoparticles were then resuspended into toluene.

This synthesis method using shorter ligands such as pentene was to bring the particles closer together. The additional aim was to achieve better passivation of the surfaces due to less shadowing from longer ligand chains and thus less oxide

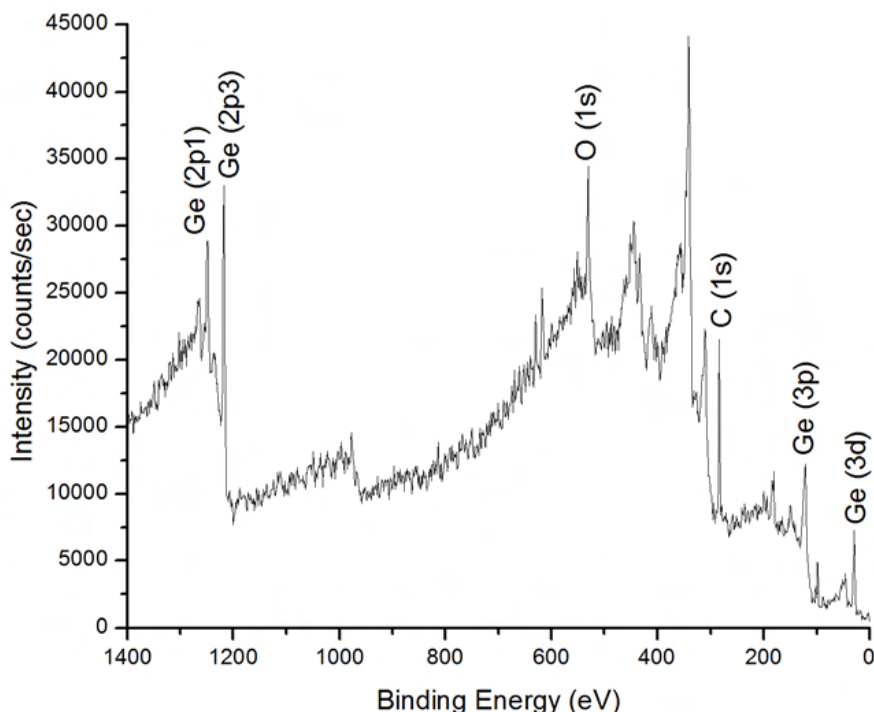


Figure 3.18: XPS spectrum of 8 nm germanium nanoparticles synthesized using 1-pentene.

generation. The synthesized particles were first observed using TEM. An image of the particles formed can be seen in Figure 3.17. The nanocrystals were still spherical in nature and were around 8 nm in diameter with 1.0 g of GeI_2 used. The particles were able to form monodisperse films though the films did seem more granular and agglomerated than the films formed by the ODE-coated nanoparticles.

With a rough estimate of the size of the nanoparticles, XPS scans were performed to determine the composition of the nanoparticles. The survey spectrum can be seen in Figure 3.18 while the high resolution XPS spectrum around the 3d peak of germanium can be seen in Figure 3.19. It was determined in these scans that while germanium nanoparticles were still being formed as in the initial protocol, the amount of oxidation also had gone up as well. For particles twelve hours after synthesis, their composition was 69.3% Ge and 30.7% GeO_2 . The particles remained relatively stable around this point even two days after synthesis.

It was obvious from the XPS scans and TEM images that the particles were not as high quality as the initial protocol batches. Unfortunately, pentene is less stable than octadecene (ODE). Pentene has a boiling point of 30°C while octadecene has a boiling point of 316°C , which is 10.5 times higher. The ligand precursor, 1-

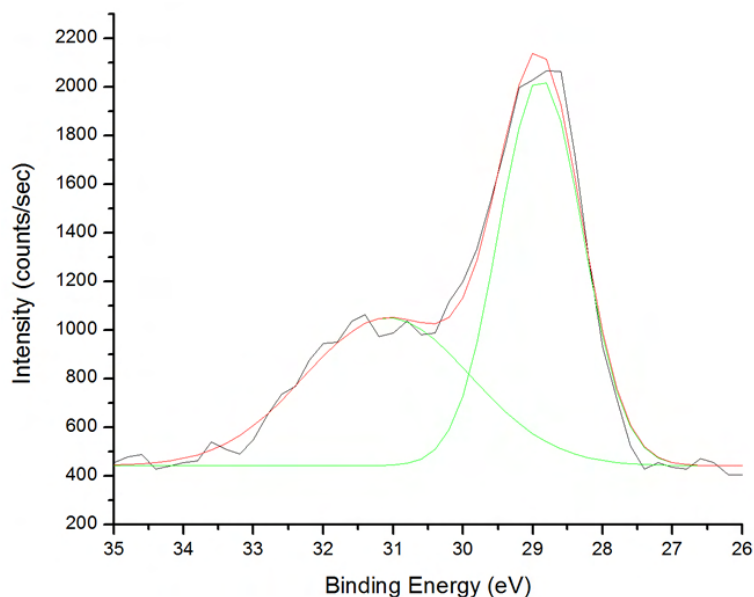


Figure 3.19: High resolution XPS spectrum of the 3d peak of 8 nm germanium nanoparticles synthesized using 1-pentene.

pentene, is a liquid at room temperature, but was seen to accumulate in the condenser connected to the fume extractor in the glovebox during the reaction. There was a very high likelihood that most of the 1-pentene had boiled away during the reaction and had not coated the nanoparticles. A reaction run with just HDA had also been performed and nanoparticles had been formed in the 5-10 nm range in this case. However, oxidation levels were much higher with over 50% of the particle oxidized after twenty-four hours according to XPS scans. Therefore, some hydrogermylation had occurred prior to the majority of the 1-pentene being boiled away. However, the much larger levels of oxidation also suggested that HDA had worked to form the nanoparticles. During the nanoparticle wash, HDA, which is miscible in acetone, is mostly to completely removed. Amine-bonding to germanium is very weak and it is known that thiol bonding and hydrogermylation will dominate the reaction [60]. However, due to the lack of 1-pentene during the reaction, HDA and 1-pentene both worked to coat the particle. Oxidation levels were still too high to deem the particles useful for the active layer of the transistor however.

3.2.5 ODE post-functionalization protocol

With all the results from the previous two reaction protocols, several facts were determined about the reaction kinetics. These were:

1. Size of the nanoparticle was determined by the amount of GeI_2 used in the reaction. Should there be insufficient ligands added, then a small portion of the nanoparticles may become smaller. However, given enough time for the reaction, as was tried as secondary experiments to augment both the initial and 1-pentene protocol, it was seen that all the particles will become the same size with same size distribution. The initial lack of ligands results in a longer reaction time being necessary (the secondary experiments were run for one hour and thirty minutes at the 300°C reaction temperature with the remainder of the protocols the same as the initial protocol and 1-pentene protocol) to fully complete the nanoparticle growth. The size of the particles in general do increase a little, but not substantially.
2. Based on the facts 1) the amount of GeI_2 added primarily controlled the size of the particle rather than the amount of ODE or 1-pentene added and 2) HDA alone (no ODE or 1-pentene added) produced nanoparticles of similar size and shape as the ODE and 1-pentene particles, HDA also participates in the reaction to limit the size and growth of the nanoparticles. This can be ascribed to the factor that both HDA and ODE have very similar boiling points. HDA has a boiling point of 330°C which is only about 10°C higher than ODE. Also, depending on the pressure (the glovebox chamber pressure was kept between 2.5-3 bar or about three times ambient pressure), the HDA and ODE could have boiling temperatures within 10°C of each other. During the 1-pentene reaction, due to a large majority of the 1-pentene injected being boiled away, HDA was sure to participate in the nanoparticle formation here as well.
3. It was found by Lee *et al.* that higher quality germanium nanocrystals were formed with the ODE and BuLi being injected at 200°C as opposed to a lower temperature [64]. This fact was also observed in several other papers [43, 49, 60]. These papers combined with the experiments performed during the initial protocol and 1-pentene protocol showed that alkyl functionalization, either through hydrogermylation or Grignard reactions requires higher temperatures for proper passivation. Even with a low boiling point ligand like 1-pentene, it still managed to partially passivate the particle and the Ge-C bond was strong enough to keep it bonded to the particle through the reaction.
4. The amount of oxidation of the nanoparticles - between 20-30% - showed that incomplete passivation was occurring. The methanol/acetone wash, while relatively harsh to remove the HDA and other byproducts, should in general not strip that many ligands from the nanoparticles. Furthermore, the fact the particles remain stable at that level of oxidation for prolonged periods of time demonstrate the strength of the Ge-C bond and the ligand's resistance to oxidation.

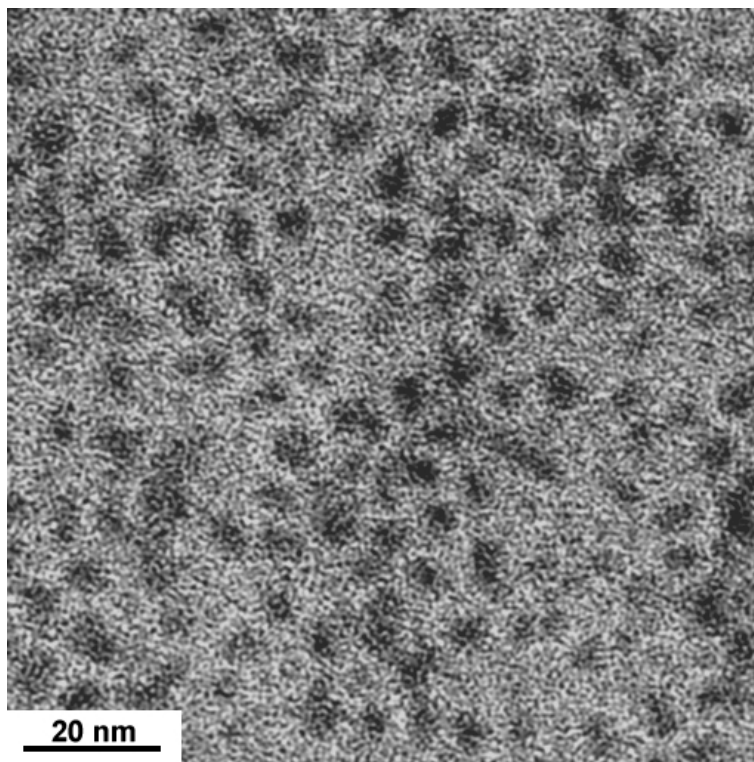


Figure 3.20: TEM image of the 5 nm germanium nanoparticles with ODE ligand coat synthesized through new hydrogermylation protocol stored under ambient conditions twelve hours after synthesis.

5. Germanium is a borderline element when carbon bonding is concerned. Homolytic dissociation can often occur at temperatures $>200^{\circ}\text{C}$. This coincides with the reported Ge-C bond strength of 460 kJ/mole which in general suggests a required temperature of 230°C to break the bond.

From the above facts, it can be determined that part, if not the majority, of the incomplete passivation was due to the high temperatures during the germanium nanoparticle synthesis reaction. While some of the germanium-carbon bonding can resist the 300°C temperatures as was observed with the 1-pentene protocol, it can be theorized that a majority of the bonds could not. While ODE is stable up to 316°C , it can begin to sublime below these temperatures and the Ge-C bond is not stable. Thus, it is quite possible that the ODE helps to contain the nanoparticle size through formation of Ge-C bonds with the nanoparticle. However, it is also very likely that these octadecyl ligand groups continuously dissociate from the nanoparticle as well. Therefore it is most likely that the majority of the passivation occurs during the cool down phase, especially as the temperature drops below 230°C if we assume the 460 kJ/mole Ge-C bond strength is correct. Also, best size and shape control would

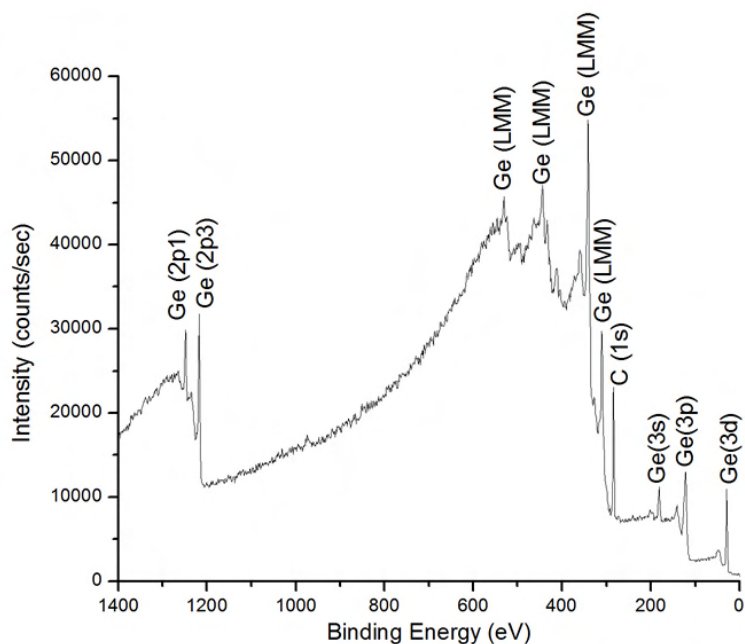


Figure 3.21: XPS survey spectrum of 5 nm germanium nanoparticles with ODE ligand coat synthesized through new hydrogermylation protocol stored under N_2 twelve hours after synthesis.

occur if this cool down phase was properly controlled. These facts also explain why so much ODE - 3 mL - in proportion to the GeI_2 - 0.2 g - was required for proper passivation of the nanoparticles in the protocol of Lee *et al.* However, since the ODE is continuously being reacted, functionalized onto the nanoparticle and then dissociating to octadecane ligands, towards the end of the reaction and during the cool down phase it is questionable whether there is sufficient ODE to passivate the surface. Also, due to the quick cool-down of the solution, there is also a question of whether there is sufficient time at the elevated temperatures for the functionalization to occur properly.

Therefore a new protocol was developed based on these facts about hydrogermylation of nanoparticles. This protocol is as follows:

1. Purge the glovebox down to <1 ppm O_2 and <1 ppm of H_2O . The oxygen levels and moisture levels should be kept below 5 ppm during entire run, preferably below 1 ppm. Dry all glassware, stir bars, etc. Also bubble N_2 through all solvents to be utilized, anhydrous or not. Ensure this bubbling occurs under the fume extractor so it can draw away any residual oxygen still present in the solvents. Perform this for one to two hours. Dry all powder reactants as well.

2. Place 3 g of hexadecylamine (HDA) into a 25 mL beaker and heat to 200°C on a digital hotplate. Ensure that the fume extractor is in place on top of the beaker to draw away the HDA fumes. Otherwise the HDA will condense on the walls of the glovebox chamber.
3. Add 0.15 g of GeI₂. Wait for it to dissolve. The solution should first turn a pale yellow and then turn gray. Swirl beaker to help stir and dissolve the GeI₂. The GeI₂ will not dissolve well in the HDA below 200°C and not at all below 180°C.
4. Dilute N-Butyllithium (0.8 mL of a 1.6 M hexane solution)(BuLi) with 2.4 mL of 1-octadecene (ODE) in a 10 mL beaker. Using a glass pipette, inject the N-Butyllithium/ODE mixture into the HDA/GeI₂ solution. Swirl and keep at 200°C for five minutes to allow dissolution. The solution should start to give off a large amount of white fumes. Then further heat to 300°C. Once at 300°C, allow to heat for one hour. The grayish solution should start to give off lots of white vapor and turn black.
5. Turn down the hotplate to 190°C. Once the solution cools to this temperature, add 0.5 mL of ODE. Allow this reaction to run for five minutes.
6. Turn down the hotplate and allow the solution to cool to 100°C. Add an equal volume of methanol to precipitate the nanocrystals. The solution should turn into a grayish sludge. Transfer the sludge into several anaerobic centrifuge tubes. Seal the centrifuge tubes prior to removing them from the glovebox.
7. Centrifuge the tubes at 4000 rpm for ten minutes. Once done, transfer the tubes back into the glovebox. Draw away as much supernatant as possible.
8. Redissolve the precipitate into toluene. Add an equal volume of 50 % acetone/ 50 % methanol. Repeat from step 7 for three more times to clean away any reaction byproducts. The particles should be precipitated as a black powder to the bottom of the centrifuge tube.
9. For the final colloid, redissolve the precipitate into toluene. Aim for at least a 1 % solution. Store the final nanoparticle colloid in the glovebox.

Germanium nanoparticles were synthesized according to the aforementioned synthesis method. TEM images were taken of the nanoparticles and can be seen in Figure 3.20. To determine the size distribution, several images of the nanoparticles from across the grid were taken and the size of the nanoparticles measured. SAXS would have been preferable, however, due to time constraints and the necessity to wait for beamtime in order to perform SAXS, TEM counting was utilized instead. The nanoparticles were 5 nm ± 0.5nm (n = 550). Due to contrast issues in the TEM images and the need to adjust filter setting on the images in order to distinguish the

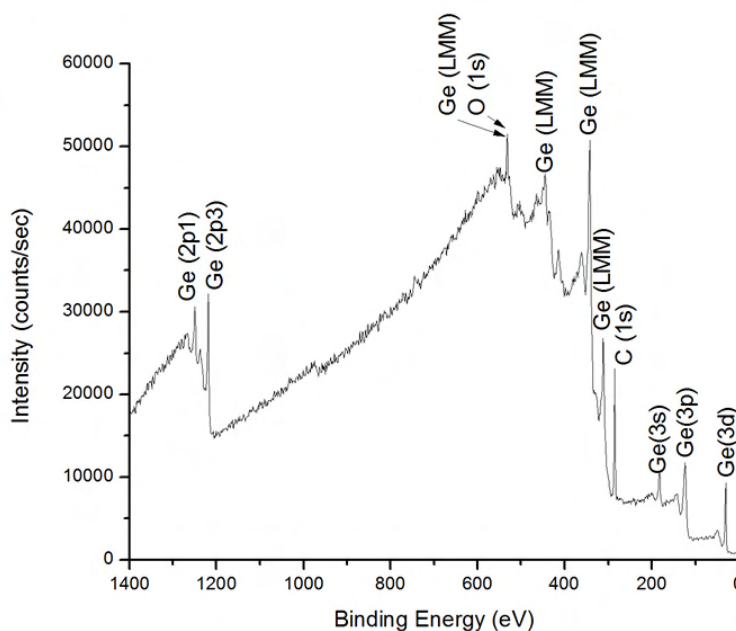


Figure 3.22: XPS spectrum of 5 nm germanium nanoparticles with ODE ligand coat synthesized through new hydrogermylation protocol stored under ambient conditions twelve hours after synthesis.

edges of the nanoparticles, the size distribution was rounded up to be ± 5 Å. However, just based on direct observation of the particles without consideration of the fuzzy edges, the size distribution did seem to be less, nearer to ± 3 Å. A future SAXS measurement combined with a WAXS measurement would be able to better determine the size distribution of a larger number of nanoparticles. However, in general, the TEM images showed that the nanoparticles formed were of spherical geometry, tightly distributed in size and very monodisperse. The drop-casted solution was relatively concentrated (~ 50 mM), yet the particles still formed a close-packed film and did not agglomerate. The average spacing between particles was 1.6 nm which corresponded with the measurements taken for the initial protocol. The overall quality of these nanoparticle based on size, distribution and geometry of these nanoparticles were better than that of the nanoparticles synthesized using the initial protocol.

Since the crystallinity of the nanoparticles, based on the method and temperatures used in synthesis and results from previous synthesis runs, was given, the main factor that needed to be characterized was the composition of the nanoparticles. To determine the composition, XPS scans were performed on the nanoparticle samples. One vial of nanoparticles was kept in the ambient while the other was kept in the glovebox. The O_2 levels never exceeded 10 ppm during this storage and the H_2O levels we kept < 0.1 ppm. During the nanoparticle cleaning stage, glovebox levels of

Table 3.4: Photoelectron lines for Ge and chemical shifts due to bonding with other elements [10]

Element/Compound	3d peak position or shift (eV)	2p ^{3/2} peak position or shift (eV)
Ge	29.4	1217.35
GeC	31.2	1218.9
GeO	-	1221.5
GeO ₂	32.5	1220.4

O₂ never exceeded 10 ppm either. The stock solutions for these nanoparticles were filtered through a 0.2 μm PTFE (polytetrafluoroethylene also known as Teflon) membrane filter. The filter was held in place in a stainless steel filter holder connected to a 10 mL chemically inert glass syringe made of glass, stainless steel and PTFE. Then the solutions were 10x diluted to approximately 50 mM and drop-casted onto silicon die. Once dried, the die with nanoparticles which were deposited in the inert environment were sealed in a glass vial with teflon cap for an air-tight seal. The die deposited in ambient was placed into a die holder. At approximately twelve hours after synthesis, the samples were transferred into the XPS machine, which is operated in vacuum (10^{-9} torr), for characterization. Figure 3.21 shows the XPS survey spectrum for the sample which was kept under inert conditions while Figure 3.22 shows the XPS survey spectrum for the sample kept under ambient conditions. Both survey spectrums boasted clear germanium peaks with a sharp carbon peak reflecting the octadecyl ligands. The sample kept under ambient conditions showed a larger peak at 530 eV due to the presence of oxygen in addition to the germanium auger peak (labelled Ge LMM). These plots showed no other elements contaminating the sample.

The next step was to collect high resolution XPS spectra of the germanium 3d and 2p^{3/2} peaks. The high resolution spectra of the sample kept under inert conditions (sample S1) can be seen in Figure 3.23. The high resolution spectra of the sample kept under ambient conditions (sample S2) can be seen in Figure 3.24. Photoelectron lines for germanium peaks and the relevant chemical shifts are listed in the NIST XPS database and shown in Table 3.4. As can be seen in the spectra of sample S1, there was no oxide formed. Once the peaks were adjusted to the baseline photoelectron line data from the database and compared, it was determined that 83.5% of the particles was germanium and 16.5% was Ge-C bonds from the ligands bonding to the surface of the nanoparticles. The spectra of sample S2 did show the presence of germanium dioxide. 70.3% of the nanoparticles was germanium, 13% Ge-C bonds and 16.8% germanium dioxide. There were no peaks showing the formation of germanium monoxide, even in the 2p^{3/2} high resolution spectra.

To determine the thickness of the oxide formed on the nanoparticles and to get a rough estimation of the thickness of the ligands, a sputter profile of the nanoparticles

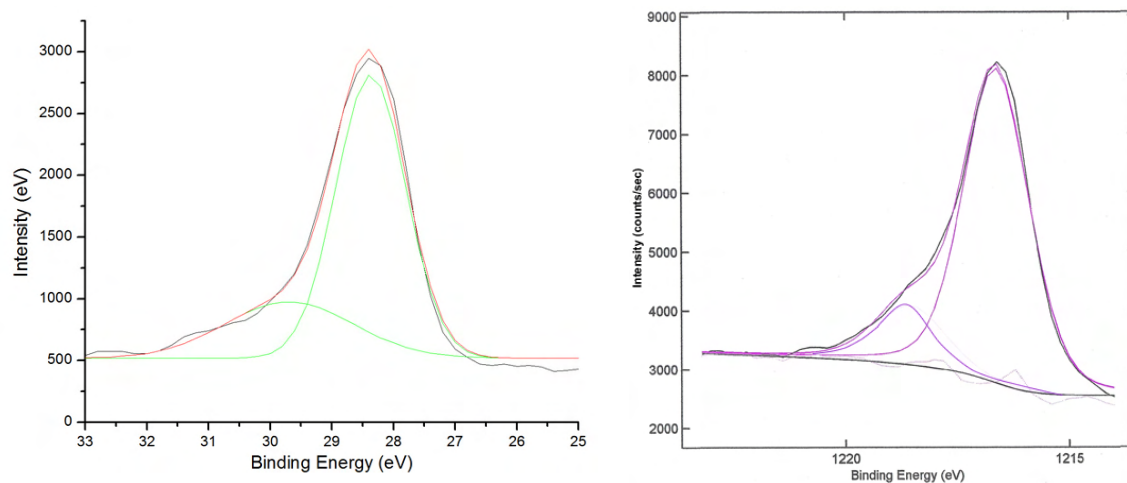


Figure 3.23: High resolution XPS spectrum of the 3d (above left) and $2p_{3/2}$ (above right) peaks of the 5 nm germanium nanoparticles with ODE ligand coat stored under N_2 twelve hours after synthesis.

was performed in the XPS machine. This sputter profile can be seen in Figure 3.24. The high resolution scan was performed about the $2p_{3/2}$ peak due to the higher surface sensitivity of peaks with higher binding energy. From the sputter profile, it can be seen the germanium dioxide peak is removed after the first sputter interval. Based on the previous sputtering performed with the XPS machine, it was known that approximately 3 \AA was removed per six second sputtering interval. Therefore the oxide thickness was $\leq 3 \text{ \AA}$. Also, the Ge-C peak disappeared after thirty seconds of sputtering. Taking into account the slower sputtering (estimated to be 50% slower than that of germanium and germanium dioxide) of carbon by the ion gun, the ligand coat was approximately 8 \AA thick. This coincided with the ligand coat thicknesses measured from the TEM images.

3.3 Discussion and Conclusion

Several different hydrogermylation protocols were developed for synthesis of germanium nanoparticles between 3 - 8 nm in diameter. Each synthesis protocol provided the necessary results to determine the reaction kinetics behind the hydrogermylation reaction and in turn develop a new, optimized hydrogermylation protocol for the synthesis of better passivated germanium nanoparticles. While problems of crystallinity of the germanium nanoparticles had been previously worked out (resulting in infrared photoluminescence for the nanoparticles), the new protocols developed improved the size distribution and passivation of the nanoparticles. These two components were of utmost importance for development of a semiconductor nanocomposite from the or-

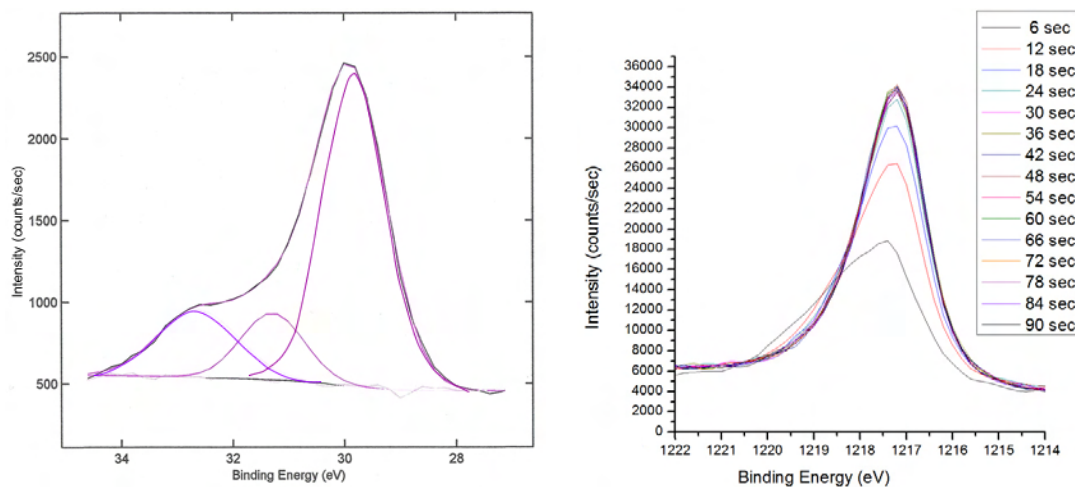


Figure 3.24: High resolution XPS spectrum of the 3d (above left) peak of the 5 nm germanium nanoparticles with ODE ligand coat stored under ambient conditions twelve hours after synthesis. The sputter profile of the nanoparticles for determination of the oxide and ligand coat thickness (above right).

organics and nanoparticles being utilized. ODE and other alkyl groups can be found in nature and the human body and thus are for the most part biocompatible. This was a necessary component for eventual use of these transistors in lab-on-a-chip platforms where the active layer could be in direct contact with the target specimen.

While the 1-pentene protocol resulted in more oxide formation, the ODE post-functionalization protocol resulted in better size distribution, shape and passivation than those formed utilizing the initial protocol. The size distribution was $\pm 2\text{\AA}$ tighter than those reported by Lee *et al.* and the particles exposed to ambient conditions had 5-10% less oxide formation. The quality of the nanoparticles formed were also higher such that the Ge-C and oxide peaks were clearly distinguishable using the same XPS system. Of greater interest were the particles synthesized and kept under inert conditions. These particles had no oxidation which plays a dominant factor in the transport of carriers between nanoparticles. Based on work from Talapin *et al.* and confirming studies performed at UC Berkeley, even the slightest bit of oxidation of the PbSe nanoparticles ended transistor performance. It could be theorized that due to the large exciton Bohr radius of both PbSe and germanium nanoparticles, the interparticle spacing would be less important than the oxidation on the particles. The oxides have a much larger band gap and introduce many trap states which prevents tunneling of carriers. Reducing the interparticle distance was accomplished by Talapin *et al.* by stripping the oleic acid ligands and partially replacing them with very short hydrazine ligands. This had a substantial impact on tunneling, however, tunneling

should still be able to occur so long as there is sufficient overlap between the exciton Bohr radii from the germanium in the nanoparticles.

These particles with no oxidation held the largest promise of forming a semiconductor nanocomposite for the active layer for the PNTFT. However, there are additional issues with the unpassified, exposed germanium sites on the nanoparticles (which was the reason the nanoparticles synthesized using the post-functionalization protocol still oxidized). These issues will be discussed in the following chapter. A short post-functionalization step was included in the third synthesis method. Due to time constraints, further modification of this synthesis protocol was not performed and tested. However, a longer post-functionalization step at possibly a slightly lower temperature of 170°C would result in high quality and better overall passivation of the germanium nanoparticles. Another possibility offered by this post-functionalization step is the use and proper passivation of the nanoparticles with shorter alkyl ligands which would help reduce the interparticle spacing. Overall, adding in the post-functionalization step and understanding the role of HDA in the particle synthesis increases the flexibility of hydrogermylation as a route to highly crystalline and monodisperse germanium nanoparticle synthesis. While the dissertation research primarily focuses on semiconductor research for the use of the film in transistors and sensors, these nanoparticles hold much promise as fluorescent labels due to their high photoluminescence in the near IR range, for optical communication devices and as a highly crystalline, well oriented platform for growth of other germanium 1D and 2D structures without the use of a furnace.

Chapter 4

Polymer Nanocomposite Thin-Film Transistor (PNTFT)

4.1 Background

The use of transistors as both circuit and sensing elements is commonplace. Transistors are used in everyday circuitry in processors in computers and cell phones while phototransistors are used as very sensitive optoelectronic sensors in televisions and cameras. There has been a large push towards flexible electronics and the fabrication of these devices on alternative substrates such as plastics to minimize cost and complexity through direct integration rather than in a separate chip. The IPSMS is a novel platform utilizing separation and microfluidic channels on the surface of the lab-on-a-chip platform. Like other lab-on-a-chip platforms, it needs a compact and truly mobile detection stage. The majority of lab-on-a-chip platforms still utilize very complex optics and detection mechanisms such as laser-induced fluorescence (LIF) to make very sensitive measurements. Other methods have been suggested such as tagless methods like Surface-Enhanced Raman Spectroscopy (SERS) and impedance spectroscopy. Prototypes of such detection platforms have been implemented, however there are still many issues with sensitivity and more importantly, in order to utilize these systems, biological signatures would need to be recorded of hundreds of thousands to millions of different entities which already exist for current optical techniques due to the decades of research and usage of these methods. Also, the relative ease with which we can determine biological signatures for unknown entities due to the existing infrastructure and those with knowledge of required techniques in medicine and biology is another large obstacle for methods which are not backwards compatible with current methods. The reticence of the medical and pharmaceutical industry (which stems in part from patient liability claims and the large body of strict, regulating bodies like the Food and Drug Administration) to implement novel techniques when there exists working methods, albeit often very tedious and slow,

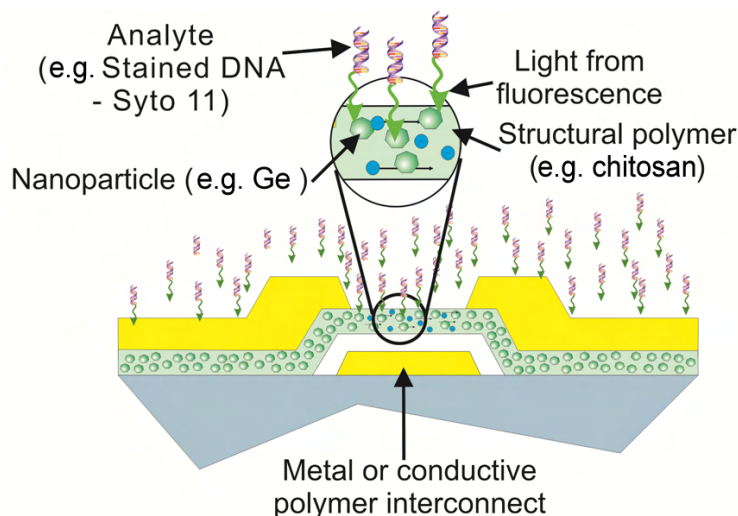


Figure 4.1: The PNTFT operating as a highly sensitive phototransistor.

obstructs application of completely novel methods. For this reason, even with many novel techniques, devices and methods being discovered in research over the past several decades, the industry still depends on what could be considered antiquated techniques such as bulk gel electrophoresis and fluorescent tagging of biomolecules.

The IPSMS platform and the PNTFT were developed to address the previous issues, offering a novel method for detection of unknown and known entities such as viruses and DNA, but being backwards compatible with the optical methods in use so the large body of knowledge collected from previous research would still be applicable and could be used for identification of these entities. The focus of this dissertation research was to enable the development of a sensor from a thin-film transistor platform which could be implemented on a large variety of substrates, but still retain high sensitivity and specificity to target analytes if needed.

4.2 Operation of the PNTFT

Two types of PNTFTs have been envisioned in this research. The first type was an optically sensitive PNTFT through direct usage of the special characteristics of the quantum dots (germanium nanoparticles) and their tailorable sensitivity to light in the near-infrared to visible range. Quantum confinement allows for longer periods prior to recombination (5-40 ns) allowing for impact ionization to occur (several excitons per photon). This increases the possible carriers for transport and thus current generation. This is similar to the avalanche mechanism used in current phototransistors to increase their sensitivity to photons. The main difference is the printability of the PNTFT structure. Since the entire transistor could be printed using nanoparticle



Figure 4.2: Model of the optical setup for the PNTFT sensor integrated into the IPSMS.

colloids (“inks”), the structure could be printed onto a large range of substrates including flexible plastic substrates. The entire fabrication process, should issues with the passivation of the nanoparticles used for the active layer (germanium nanoparticles) be resolved, can be performed in ambient conditions and with large scale printing processes, be compatible with bulk manufacturing.

The optically sensitive PNTFT (OS-PNTFT) has a metallic or conductive polymer gate, source, and drain; and a silicon dioxide, amorphous silicon carbide or polymer dielectric layer (note: high-K dielectric materials could also be utilized). One configuration of these transistors can be observed in Figure 4.1. Semiconducting nanoparticles (ligand-coated germanium nanoparticles) which can be further bonded into another polymeric matrix (e.g. chitosan) for additional stability, will be used as the TFT active layer. This active layer, when irradiated with low-intensity fluorescent light, will gain additional photogenerated current which can be used to determine the presence and amount of the tagged or fluorescing molecules.

To induce the optical fluorescence while minimizing background to maximize the signal, a unique setup was utilized. Three LEDs (light-emitting diodes) are placed 30° to the normal of the plane of the IPSMS chip below the transparent substrate

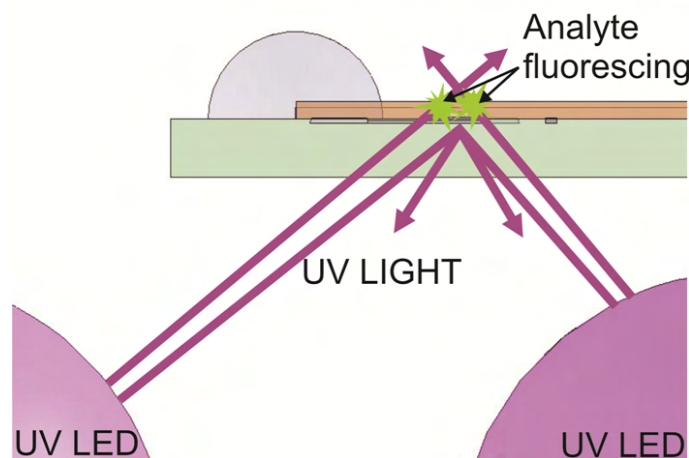


Figure 4.3: A larger view of how the optical detection mechanism is to operate.

of the IPSMS chip. This setup can be seen in Figure 4.2. When the LEDs are on, they illuminate the channel directly above the transistor due to the angle they are placed and their own small cone of illumination. The transistor gate, being a thick enough metal layer, reflects and blocks light from the LEDs from reaching the active layer of the PNTFT as seen in Figure 4.3. When molecules, excited by the light from the LEDs, fluoresce in the channel above the transistor, they emit light in all directions. Due to the very short path length between the fluorescing molecules and active layer of the PNTFT ($<50\ \mu\text{m}$), this greatly increases the amount of fluorescent light irradiating the active layer of the PNTFT which then translates into an increased current in the PNTFT. Due to the light from the LEDs being blocked, so long as the channel on top is appropriately shielded, there will be very low background light interference.

The second type is the electromechanically sensitive PNTFT (EMS-PNTFT). The EMS-PNTFT uses enzymes embedded into the polymeric active layer alongside semi-conducting nanoparticles. Thus, the transistor becomes sensitive to the changes in conformation of the proteins embedded in the matrix. As a result, the transistor should be sensitive to the protein activity level, or the analyte concentration (based on Michalsen-Menton enzyme kinetics). Figure 4.4 shows a schematic of one possible configuration of the EMS-PNTFT. In this approach, when the proteins bind a target molecule, its conformation changes inducing stress into the film. This in turn will displace the position of the nanoparticles surrounding the protein. Since the current through the transistor is an exponential function of the tunneling distance between the nanoparticles, small changes to this interparticle distance will greatly affect the output current. These changes will be detected as increases in current as the interparticle distances around the protein will likely drop as the particles are squeezed

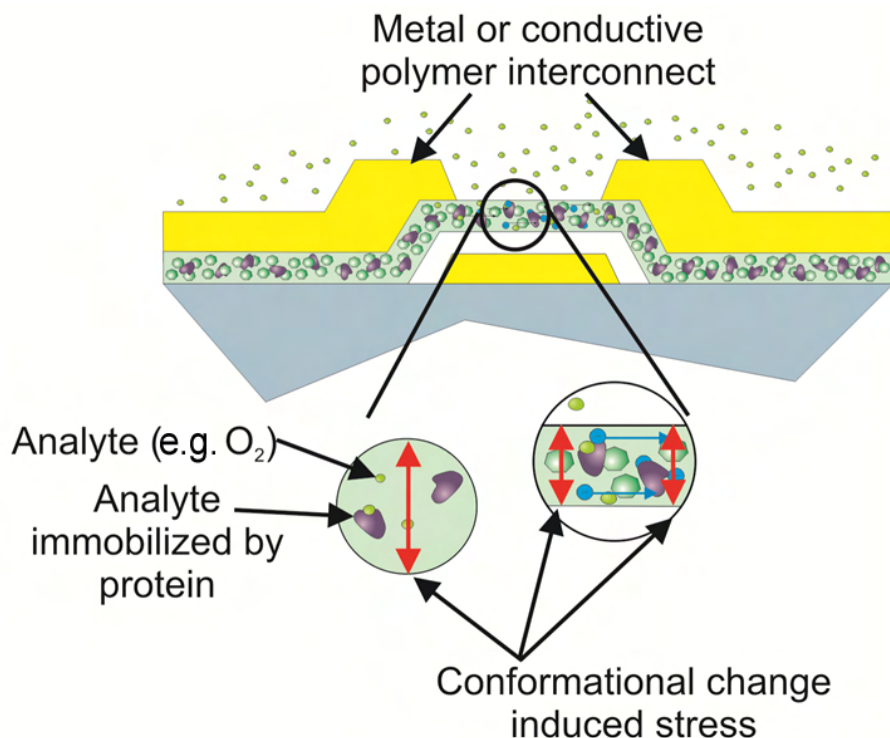


Figure 4.4: The PNTFT operating in an electromechanical mode for highly sensitive detection of specific analytes.

closer together to accommodate the additional bound target molecule. This method does not require external optics and is highly sensitive. Proteins such as antibodies developed for ELISA can be utilized in these films resulting in a backward compatible system for detection with the possibility of much higher sensitivity than the ELISA technique itself.

For this dissertation research, focus was placed on developing a proper semiconductor nanocomposite for the active layer of the PNTFT. Preliminary experimentation was performed on developing novel thin-film transistor bases and testing the nanocomposite film on them to detect whether there was viable transistor operation. The experiments performed and their results are presented below.

4.3 Thin-Film Transistor Base

The first step for development of a thin-film transistor base for testing the synthesized nanocomposites and to act as a base for future PNTFT fabrication was to fabricate standard TFT bases, but on a pyrex wafer. Pyrex wafers were used since they would still be able to take high temperatures up to 450°C should higher tem-

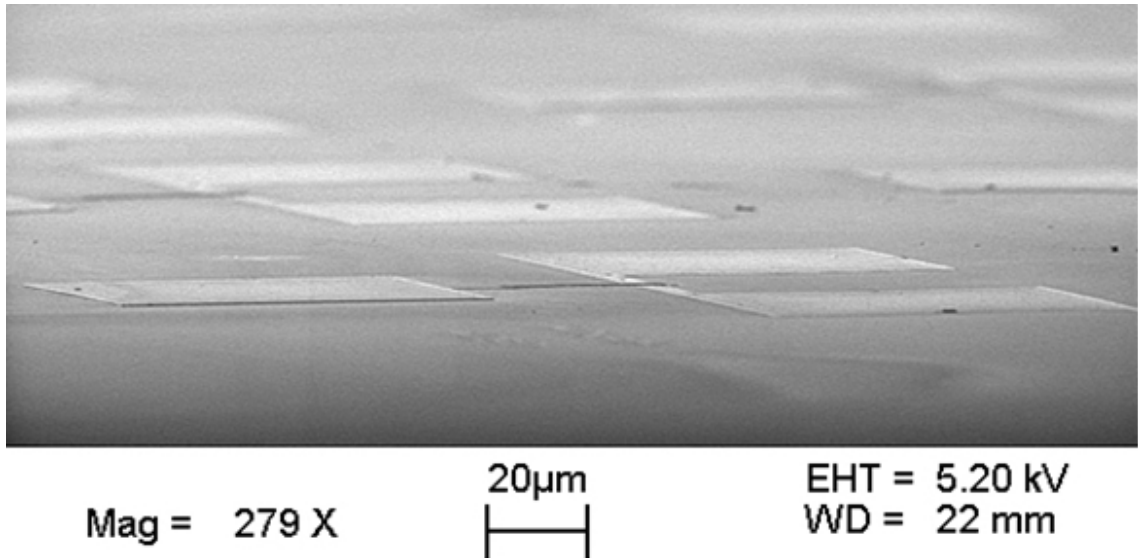


Figure 4.5: Fabricated TFT base with aluminum source, drain and gate and a silicon carbide dielectric.

perature anneals need to be performed. The source, drain and gate were sputtered aluminum from the CPA 9900 sputtering tool in the Berkeley microlaboratory. A 300 nm film was used for the gate and source/drain layer. The film thickness was measured using an Alpha-Step IQ (ASIQ) surface profilometer (KLA-Tencor). Deposition of aluminum was performed with the standard aluminum deposition recipe for the CPA tool with a plasma power of 4.5 kW. Track speed was adjusted based on reported process monitor values. OCG 835 35CS G-Line positive photoresist was patterned to form the etch masks for the electrodes. The aluminum was etched using the LAM3 aluminum etcher (Lam Reserach) using Cl_2 and BCl_3 gases.

The gate dielectric was deposited on top of the gate electrode and prior to the deposition of the source and drain electrodes. Two main dielectric materials were utilized. The first was PECVD silicon dioxide (SiO_2) deposited using the P5000 TEOS PECVD system (Applied Materials). The 500 nm thick films were formed through reactions with TEOS precursor gases at 400°C . The second was 100 nm thick amorphous silicon carbide ($\alpha\text{-SiC}$) deposited using an ion-beam assisted deposition system at temperatures no higher than 100°C . For the $\alpha\text{-SiC}$ films, the ion-beam was also used to compact the films more to minimize the number of defects. $\alpha\text{-SiC}$ was tested as a dielectric material due to the possible low temperatures it could be deposited at, its high-K value of ~ 10 , and its high chemical resistance, especially to diffusion of salts such as potassium found in buffer solutions used in biology. Due to the PNTFT's use in the IPSMS system, such resistance would be necessary, especially for the EMS-PNTFT.

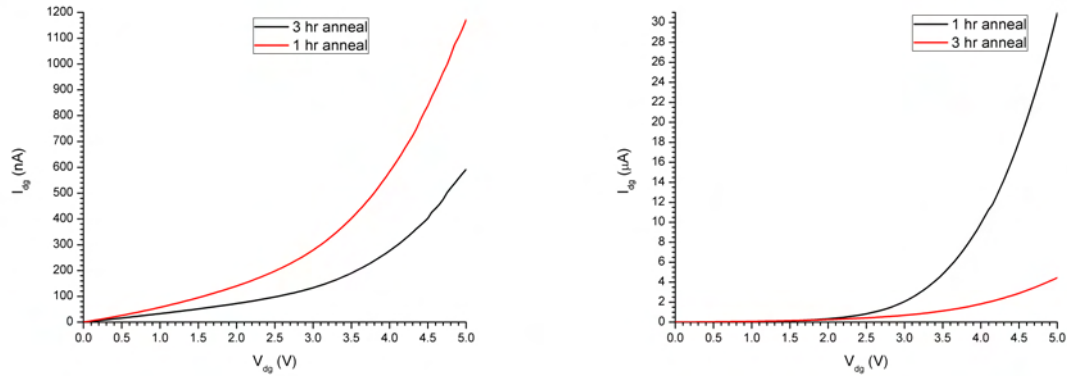


Figure 4.6: Drain current vs Gate bias curves to test just the amorphous silicon carbide dielectric films and the the effect of hydrogen anneals. The leakage up to a 0.5 V bias and 5 V bias was ascertained utilizing transistor bases with source and drain electrodes $64 \mu\text{m}$ long. The gate length for these tests was $4 \mu\text{m}$.

Current leakage was tested by using $4 \mu\text{m}$ wide and $64 \mu\text{m}$ wide transistor bases. Both transistor bases had $4 \mu\text{m}$ channel lengths. The current leakage values were scaled to a transistor of $1 \mu\text{m}$ width and $1 \mu\text{m}$ length ($n=5$). There was no active layer deposited. The drain current was recorded as the gate was biased up to 5 V. For a thin-film transistor with a thermally grown oxide, the leakage current is normally on the order of 1 or less pA at a gate bias of 5 V. The PECVD SiO_2 was found to have a leakage current of 1.25 nA at a gate bias of 5 V. This was about one thousand times higher than the thermally grown oxide. Unfortunately this was still too large for testing the nanocomposite performance. The α -SiC films were tested next and found to have leakage currents of $\sim 6 \mu\text{A}$ at a gate bias of 5 V. This was substantially higher than the PECVD SiO_2 . To reduce the leakage, hydrogen anneals using forming gas were used. The transistor bases were annealed in a 100 W hydrogen plasma at 300°C for one or two hours. The results of the anneals are shown in Figure 4.6. After a one hour hydrogen plasma anneal, the leakage was reduced to $1.9 \mu\text{A}$ at a gate bias of 5 V. After a two hour anneal, the leakage was reduced to 281 nA. Based on these results, a four to five hour anneal would be necessary to acheive the same leakage as PECVD SiO_2 should the reduction in leakage scale linearly. If this linear scaling holds, an eight to nine hour anneal would be necessary to reduce the leakage to levels close to thermally grown oxide. Therefore it would be far better for the α -SiC to be deposited in a forming gas environment for insitu annealing of defects. Also deposition at raised temperatures would likely reduce the defects and thus leakage in the film.

However, due to much higher temperatures either platform required for fabrication, neither platform would be easily adaptable to a low temperature fabrication method. Also, a much more robust platform with lower leakage was necessary for

determining the characteristics of the semiconductor nanocomposite films. Therefore new test transistor dies were fabricated. Degenerately doped silicon (arsenic n^+ type) was used as the bottom gate, 100 nm thick thermally grown SiO_2 in the microlab furnaces, and evaporated gold electrodes (~ 50 nm) on a 10 \AA chrome adhesion layer. The gold electrodes were patterned by lift-off. Gold was used due to germanium nanocomposite likely being a p-type semiconductor film so there would be better valence band matching at the electrodes. Also aluminum normally forms a very thin oxide film which could impede conduction of electrons between the electrodes and the nanocomposite film. One wafer of dies were fabricated and diced. Sixty dies were prepared, each being $10.89 \text{ mm} \times 10.89 \text{ mm}$.

4.4 Active layer Deposition and Treatment

Using the germanium nanoparticles synthesized, active layers for the TFT were formed. Since the procedure was performed in the glovebox, drop-casting was used to apply the germanium nanoparticles onto the substrate. The first step was to determine whether a hexamethyldisilazane (HMDS) layer was necessary in order to drop-cast a uniform, monodisperse film of nanoparticles onto the test dies. Talapin *et al.* used HMDS to aid in drop-casting uniform, monodisperse films of PbSe onto their test dies. To test this, ~ 50 mM solutions of ODE-coated germanium nanoparticles were drop-casted onto silicon dies with and without HMDS treatment. The HMDS treatment was performed in the HMDS deposition tank at sink 4 of the Berkeley microfabrication laboratory. Three of these die with and without the HMDS treatment were not covered with a petri dish and allowed to dry in the glovebox. Three die with and without the HMDS treatment were covered with a pyrex petri dish and allowed to dry in the glovebox. The uncovered die normally dried in a matter of five or less minutes. The covered die took about twenty minutes to dry. The overall quality of the film through visual inspection and the coverage of the die with the nanoparticles was much better and more uniform for the covered dies. The particles on the uncovered dies had a tendency to concentrate toward the point where the final droplet of solvent evaporated. The covered particles were much better dispersed across the entire die. Differences between the HMDS and plain dies were not visible. TEM images of the particles drop-casted onto the TEM grids were also very monodisperse so HMDS was not applied prior to drop-casting the germanium nanoparticles.

Once films on the the test die were deposited, these test die were taken to the probe station set-up in the Subramanian lab which is located inside a nitrogen glovebox to be tested under an inert environment. The inert environment was not as good as the glovebox used for synthesis of the nanoparticles and was suspected of having oxygen levels in the 10s of ppm. Transistors on the die were tested using a 2 probe (source and drain) and stage (gate) characterization set-up. I_{ds} vs. V_{gs} curves were recorded for each of these nanocomposite films. None of the films deposited using

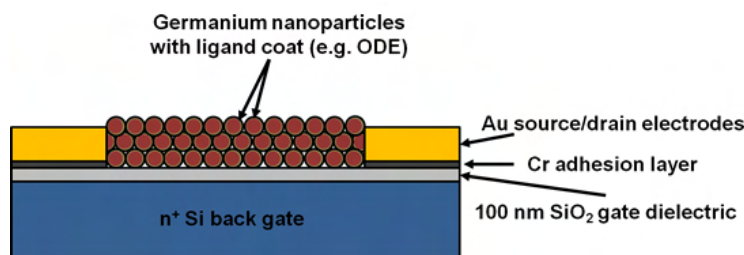


Figure 4.7: Schematic of TFT test platform with encapsulated germanium nanoparticles deposited as the active layer.

nanoparticles synthesized from each of the three different protocols discussed in the previous chapter showed transistor function. Even the nanoparticles films utilizing germanium nanoparticles synthesized using the post-functionalization protocol which showed no oxidation did not demonstrate transistor function. The reasons behind this are likely due to unpassivated surface states which could trap charge where the ligands did not coat or had been stripped. Also, the interface between the nanoparticles and dielectric also probably had a number of trap states which needed to be passivated.

Three different treatments were therefore performed to achieve viable transistor function from these devices. The first treatment attempted was exposure of the films to 1 M solutions of ethylene diamine (EDA) and hydrazine in acetonitrile. Once the films were deposited onto the test dies and dried in the glovebox for one hour at ambient temperatures, the dies were dipped into either the EDA and hydrazine solutions for two hours. The dies were then removed from the solutions, washed with acetonitrile and dried for one hour in the glovebox at ambient temperatures. Some areas of the die may have lost particles and others may have formed cracks in the nanocomposite film. Solutions with ~ 5 mM of germanium nanoparticles were drop-casted onto the treated dies and dried for one hour. The treatment with EDA and hydrazine was again performed. This procedure was repeated three times to ensure a complete coat of treated germanium nanoparticles were deposited onto the transistors. These treatments were applied to particles synthesized using the initial and 1-pentene protocols, but were not applied to the particles with post-functionalization. The hydrazine treatment was found to reduce and remove the oxides formed on the PbSe nanoparticles synthesized by Talapin *et al.* [2]. Hydrazine is also an acceptor and donor molecule so it could be used to dope the nanoparticles. EDA was also utilized since it has been suggested in literature that it may also have the ability to reduce germanium oxides and thus remove contaminating oxides from the surface of the particles [65]. Unfortunately these treatments were not found to work either when the transistors were tested.

The second treatment attempted was a general anneal of the nanoparticles on the dies in the glovebox. These anneals occurred at 120°C and 270°C for two hours on a

hotplate. The films annealed were formed from germanium nanoparticles synthesized utilizing the post-functionalization method and kept under inert conditions. The ODE did not seem to be removed after the 120°C anneal from the visual appearance of the film (film was glassy). However, after the 270°C anneal, the majority of the ODE seemed to have sublimated away. These films also did not show transistor performance following the anneal.

The third treatment was a 100 W hydrogen plasma anneal performed at 50°C and 100°C for two hours. The films annealed were formed from germanium nanoparticles synthesized utilizing the post-functionalization method and kept under inert conditions. Unfortunately, to transfer the dies to the vacuum chamber of the plasma machine, the dies had to be brought into ambient conditions. Though the time the dies were exposed to ambient was kept short (around ten minutes prior to reaching the probe station), this was likely sufficient time to oxidize the particles. Also, the raised temperature in the chamber due to the plasma (50°C was the lowest temperature the chamber could be due to heating from the plasma) combined with the vacuum (50 mTorr) resulted in the evaporation of the ODE and in turn, resulted in the loss of a large majority of the germanium nanoparticles deposited. Therefore a successful treatment had yet to be found.

4.5 Discussion and Conclusion

Some initial testing of prototype PNTFTs was accomplished, though viable transistor performance has yet to be observed. Transistor base work with α -SiC holds promise should the defect level be reduced and methods for depositing α -SiC in ambient can be worked out. One possible method of depositing α -SiC would be through a nanoparticle colloid ink like the electrodes and active layer. An anneal could be used to sinter the particles together or chemical treatment performed to bond together the ligands coating the α -SiC particles to form a low leakage, robust, printable dielectric layer.

Of the treatments performed, the anneal in forming gas holds the most promise to achieving a working device. Trap states which would be passivated by the anneal would hopefully allow for transport of carriers. Also, a hydrazine or EDA treatment of the post-functionalization nanoparticles may also help to achieve a working device. Due to time constraints, a larger variety of treatment conditions were not explored. Many possible combinations still can be performed. Also, improved passivation of the nanoparticles would also aid in achieving a working device. Using an optimized post-functionalization protocol, there would be higher possibility of success. The research performed on the PNTFT prototypes provides a platform for future experimentation which holds possibility of achieving a functional PNTFT.

Chapter 5

Future Work

While the work in developing the PNTFT has been quite extensive, there are many components left to develop. The main basis of this dissertation research has been to put together the tools and synthesize the materials necessary to perform the PNTFT research. This has encompassed:

1. Setting up a nanoparticle synthesis laboratory,
2. Development of nanoparticle synthesis protocols and synthesis of oxide-free germanium nanoparticles,
3. Microfabrication of thin-film transistor bases which can be used for testing the nanocomposite films,
4. Testing of dielectric materials which may be needed to provide the transistor the robustness it requires as a sensor as part of the IPSMS,
5. Developing patterning techniques for chitosan, a polymer which stands as a good candidate as a scaffold polymer to add proteins and other biomolecules to the PNTFT,
6. Patterning of bulk functionalized chitosan films and
7. Testing and characterization of prototype PNTFTs.

The work remaining can be divided into four main categories: 1) Optimization of nanoparticle synthesis protocol, 2) Optimization of the nanocomposite films on the TFT base, 3) Size optimization of the particles and their ligands to tune them to a specific target spectrum and 4) Integration of proteins and biomolecules into the nanocomposite films.

Many of the details of problems still requiring exploration in each of these categories have been mentioned in the previous chapters. The post-functionalization

protocol, even though passivation, size distribution and quality of the germanium nanocrystals were improved, still needs to be optimized such that nearly if not 100 % of the nanocrystal surface is passivated. The post-functionalization protocol also provides a method to utilize shorter ligands which would also reduce interparticle spacing and increase carrier tunneling probability. Higher temperature, forming gas anneals performed in the N₂ environment of the glovebox have also not been attempted yet. This method could provide a shortcut to a working device, even with the passivation of the nanoparticles being incomplete. Exposure of the post-functionalized germanium nanoparticle films to EDA and hydrazine has the possibility of inducing doping to increase transistor performance.

Once the PNTFT achieves satisfactory performance, there will need to be an optimization of the size of the nanoparticles to target specific bands of light for detection of biomolecules. This may also require a different ligand group. There exist other alkyl functionalizations where more functional endgroups are present on the end of the alkyl group. Some of these alkyl functionalizations were performed by Tanke *et al.* resulting in particles with acetal-, hydroxy- and ester-terminated ligand groups [63]. To achieve the EMS-PNTFT, chitosan and proteins will need to be incorporated into the semiconductor nanocomposite film. Since the film will be exposed to the fluid in the microfluidic channel, the film will also have to be made additionally robust against water and oxygen. While the Ge-C bonding mechanism does form relatively strong bonds when compared to other functionalizations, it may be necessary to implement a more inert outer shell on the germanium nanoparticle to protect it against oxidation. Therefore other chemistries and functionalizations may need to be explored prior to achieving a viable EMS-PNTFT.

Bibliography

- [1] *Agilent 7100 Capillary Electrophoresis System*, Agilent Technologies, Inc., 2009.
- [2] D. Talapin and C. Murray, "PbSe Nanocrystal Solids for n-and p-Channel Thin Film Field-Effect Transistors," *Science*, vol. 310, no. 5745, pp. 86–89, 2005.
- [3] R. Raffaele, "Hybrid nanomaterials improve solar cell efficiency," *SPIE Newsroom*, 2006.
- [4] *The flexible detector: Zetalif Discovery*, Picometrics, S.A., 2009. [Online]. Available: http://www.picometrics.com/html/Product_Zetalif_Discovery.htm
- [5] Suffield, "Nanoscience R&D in the Soldier and Systems Protection Group," Defense Research and Development Canada, Tech. Rep., 2008.
- [6] M. K. Denk, "CHM 331: Inorganic Chemistry II (Organometallics)," 2000, part 1: Main Group Elements, Spring 2000.
- [7] H. Mansour and A. Hickey, "Raman characterization and chemical imaging of biocolloidal self-assemblies, drug delivery systems, and pulmonary inhalation aerosols: A review," *AAPS PharmSciTech*, vol. 8, no. 4, pp. 140–155, 2007.
- [8] C. Stoldt, M. Haag, and B. Larsen, "Preparation of freestanding germanium nanocrystals by ultrasonic aerosol pyrolysis," *Applied Physics Letters*, vol. 93, p. 043125, 2008.
- [9] Sigma-Aldrich, *Sigma-Aldrich Catalog*, Sigma-Aldrich, Co, St. Louis, MO. [Online]. Available: <http://www.sigmaaldrich.com/technical-service-home/product-catalog.html>
- [10] C. D. Wagner, A. V. Naumkin, A. Kraut-Vass, J. W. Allison, C. J. Powell, and J. John R. Rumble, *NIST X-ray Photoelectron Spectroscopy Database: NIST Standard Reference Database 20*, 3rd ed., National Institute of Standards and Technology (NIST), August 2007. [Online]. Available: <http://srdata.nist.gov/xps/Default.aspx>

- [11] B. Krajewska, "Application of chitin-and chitosan-based materials for enzyme immobilizations: a review," *Enzyme and Microbial Technology*, vol. 35, no. 2-3, pp. 126–139, 2004.
- [12] I. Park, S. Ko, H. Pan, C. Grigoropoulos, A. Pisano, J. Frchet, E. Lee, and J. Jeong, "Nanoscale Patterning and Electronics on Flexible Substrate by Direct Nanoimprinting of Metallic Nanoparticles," *Advanced Materials*, vol. 20, pp. 489–496, 2008.
- [13] C. Schauer, M. Chen, R. Price, P. Schoen, and F. Ligler, "Colored Thin Films for Specific Metal Ion Detection," *Environmental Science and Technology*, vol. 38, no. 16, pp. 4409–4413, 2004.
- [14] Z. Li and Y. Du, "Biomimic synthesis of CdS nanoparticles with enhanced luminescence," *Materials Letters*, vol. 57, no. 16-17, pp. 2480–2484, 2003.
- [15] P. He, Y. Xu, and Y. Fang, "A Review: Electrochemical DNA Biosensors for Sequence Recognition," *Analytical Letters*, vol. 38, no. 15, pp. 2597–2623, 2005.
- [16] X. Wang, Y. Du, S. Ding, Q. Wang, G. Xiong, M. Xie, X. Shen, and D. Pang, "Preparation and Third-Order Optical Nonlinearity of Self-Assembled Chitosan/CdSe-ZnS Core-Shell Quantum Dots Multilayer Films," *Journal of Physical Chemistry B*, vol. 110, no. 4, p. 1566, 2006.
- [17] M. Ravi Kumar, "A review of chitin and chitosan applications," *Reactive and Functional Polymers*, vol. 46, no. 1, pp. 1–27, 2000.
- [18] B. Hemtanon, C. Thanachayanont, D. Das, and J. Dzutta, "Diode fabricated by layer by layer deposition of semiconductor nanoparticles," *TENCON 2005 2005 IEEE Region 10*, pp. 1–6, 2005.
- [19] W. Evans, "Infrared Radiation Sensors of *Melanophila acuminata* (Coleoptera: Buprestidae): A Thermopneumatic Model," *Annals of the Entomological Society of America*, vol. 98, no. 5, pp. 738–746, 2005.
- [20] H. Bleckmann, H. Schmitz, and G. von der Emde, "Nature as a model for technical sensors," *Journal of Comparative Physiology A: Sensory, Neural, and Behavioral Physiology*, vol. 190, no. 12, pp. 971–981, 2004.
- [21] M. LeMieux, M. McConney, Y. Lin, S. Singamaneni, H. Jiang, T. Bunning, and V. Tsukruk, "Polymeric Nanolayers as Actuators for Ultrasensitive Thermal Bimorphs," *Nano Lett*, vol. 6, no. 4, p. 731, 2006.

- [22] M. Powers, S. Koev, A. Schleunitz, H. Yi, V. Hodzic, W. Bentley, G. Payne, G. Rubloff, and R. Ghodssi, "A fabrication platform for electrically mediated optically active biofunctionalized sites in BioMEMS," *Lab on a Chip*, vol. 5, no. 6, pp. 583–586, 2005.
- [23] S. Koev, M. Powers, H. Yi, L. Wu, W. Bentley, G. Rubloff, G. Payne, and R. Ghodssi, "Mechano-transduction of DNA hybridization and dopamine oxidation through electrodeposited chitosan network," *Lab on a Chip*, vol. 7, no. 1, pp. 103–111, 2007.
- [24] J. Park, X. Luo, H. Yi, T. Valentine, G. Payne, W. Bentley, R. Ghodssi, and G. Rubloff, "Chitosan-mediated in situ biomolecule assembly in completely packaged microfluidic devices," *Lab on a Chip*, vol. 6, no. 10, pp. 1315–1321, 2006.
- [25] L. Wu, M. McDermott, C. Zhu, R. Ghodssi, and G. Payne, "Mimicking Biological Phenol Reaction Cascades to Confer Mechanical Function," *Advanced Functional Materials*, vol. 16, no. 15, p. 1967, 2006.
- [26] H. Yi, L. Wu, W. Bentley, R. Ghodssi, G. Rubloff, J. Culver, and G. Payne, "Biofabrication with Chitosan," *Biomacromolecules*, vol. 6, no. 6, pp. 2881–2894, 2005.
- [27] C. Co, Y. Wang, and C. Ho, "Biocompatible micropatterning of two different cell types," *J. Am. Chem. Soc.*, vol. 127, no. 6, pp. 1598–9, 2005.
- [28] G. EAST and Y. QIN, "Wet spinning of chitosan and the acetylation of chitosan fibers," *Journal of Applied Polymer Science*, vol. 50, no. 10, pp. 1773–1779, 1993.
- [29] I. Park, J. Cheng, A. Pisano, E. Lee, and J. Jeong, "Low temperature, low pressure nanoimprinting of chitosan as a biomaterial for bionanotechnology applications," *Applied Physics Letters*, vol. 90, p. 093902, 2007.
- [30] J. Tien, Y. Xia, and G. Whitesides, "Microcontact Printing of SAMs," *Thin Films*, vol. 24, pp. 228–254, 1998.
- [31] L. Tan, Y. Kong, S. Pang, and A. Yee, "Imprinting of polymer at low temperature and pressure," *Journal of Vacuum Science & Technology B: Microelectronics and Nanometer Structures*, vol. 22, p. 2486, 2004.
- [32] T. Ang, F. Sultana, D. Hutmacher, Y. Wong, J. Fuh, X. Mo, H. Loh, E. Burdet, and S. Teoh, "Fabrication of 3D chitosan–hydroxyapatite scaffolds using a robotic dispensing system," *Materials Science & Engineering C*, vol. 20, no. 1–2, pp. 35–42, 2002.

- [33] L. Wu, A. Gadre, H. Yi, M. Kastantin, G. Rubloff, W. Bentley, G. Payne, and R. Ghodssi, "Voltage-Dependent Assembly of the Polysaccharide Chitosan onto an Electrode Surface," *Langmuir*, vol. 18, no. 22, pp. 8620–8625, 2002.
- [34] J. Karp, Y. Yeo, W. Geng, C. Cannizarro, K. Yan, D. Kohane, G. Vunjak-Novakovic, R. Langer, and M. Radisic, "A photolithographic method to create cellular micropatterns," *Biomaterials*, vol. 27, no. 27, pp. 4755–4764, 2006.
- [35] A. Domard and M. Domard, "Chitosan: Structure–Properties Relationship and Biomedical Applications," *Polymeric Biomaterials*, 2002.
- [36] J. Nunthanid, S. Puttipipatkachorn, K. Yamamoto, and G. Peck, "Physical Properties and Molecular Behavior of Chitosan Films," *Drug Development and Industrial Pharmacy*, vol. 27, no. 2, pp. 143–157, 2001.
- [37] M. Corp, *SU-8 2000 Permanent Epoxy Negative Photoresist: Processing Guidelines for: SU-8 2025, SU-8 2035, SU-8 2050 and SU-8 2075*, MicroChem Corp, Newton, MA.
- [38] J. Cheng, T. Cauley, and A. Pisano, "Lithographic patterning of immobilized enzymes in chitosan thin films for multi-layer, chemical/biological sensors," in *Nanotechnology, 2007. IEEE-NANO 2007. 7th IEEE Conference on*, 2007, pp. 334–337.
- [39] C. Bréchnac, P. Houdy, M. Lahmani, and S. E. M. Research, *Nanomaterials and nanochemistry*. Springer, 2007.
- [40] M. Faraday, "The Bakerian lecture: experimental relations of gold (and other metals) to light," *Philosophical Transactions of the Royal Society of London*, vol. 147, pp. 145–181, 1857.
- [41] C. Wai and H. Ohde, "Synthesizing nanoparticles in supercritical carbon dioxide," *Journal of the Chinese Institute of Chemical Engineers*, vol. 32, no. 3, pp. 253–261, 2001.
- [42] L. J. Hope-Weeks, "Concentration-dependent size control of germanium nanocrystals," *Chemistry Letters*, vol. 34, no. 11, pp. 1526–1527, 2005.
- [43] X. Lu, B. A. Korgel, and K. P. Johnston, "High yield of germanium nanocrystals synthesized from germanium diiodide in solution," *Chemistry of Materials*, vol. 17, no. 25, pp. 6479–6485, 2005.
- [44] X. Ma, F. Wu, and S. M. Kauzlarich, "Alkyl-terminated crystalline ge nanoparticles prepared from nage: Synthesis, functionalization and optical properties," *Journal of Solid State Chemistry*, vol. 181, no. 7, pp. 1628–1633, 2008.

- [45] L. L. Araujo, R. Giulian, D. J. Sprouster, C. S. Schnohr, D. J. Llewellyn, P. Kluth, D. J. Cookson, G. J. Foran, and M. C. Ridgway, "Size-dependent characterization of embedded ge nanocrystals: Structural and thermal properties," *Physical Review B (Condensed Matter and Materials Physics)*, vol. 78, no. 9, pp. 094112–15, 2008.
- [46] D. Gerion, N. Zaitseva, C. Saw, M. F. Casula, S. Fakra, T. Van Buuren, and G. Galli, "Solution synthesis of germanium nanocrystals: Success and open challenges," *Nano Letters*, vol. 4, no. 4, pp. 597–602, 2004.
- [47] J. R. Heath, J. J. Shiang, and A. P. Alivisatos, "Germanium quantum dots: Optical properties and synthesis," *Journal of Chemical Physics*, vol. 101, no. 2, pp. 1607–1615, 1994.
- [48] P. Schittenhelm, C. Engel, F. Findeis, G. Abstreiter, A. A. Darhuber, G. Bauer, A. O. Kosogov, and P. Werner, "Self-assembled ge dots: Growth, characterization, ordering, and applications," in *Papers from the conference on silicon heterostructures: from physics to devices*, vol. 16. Barga, Tuscany (Italy): AVS, 1998, pp. 1575–1581.
- [49] D. Wang, Y. L. Chang, Z. Liu, and H. Dai, "Oxidation resistant germanium nanowires: Bulk synthesis, long chain alkanethiol functionalization, and langmuir-blodgett assembly," *J. Am. Chem. Soc.*, vol. 127, no. 33, pp. 11 871–11 875, 2005.
- [50] B. Yoo, A. Dodabalapur, D. Lee, T. Hanrath, and B. Korgel, "Germanium nanowire transistors with ethylene glycol treated poly (3, 4-ethylenedioxythiophene): poly (styrene sulfonate) contacts," *Applied Physics Letters*, vol. 90, p. 072106, 2007.
- [51] D. Poplavskyy, H. Antoniadis, D. Jurbergs, M. Kelman, F. Lemmi, and P. Yu, "US Patent App. 11/857,854: Semiconductor devices and methods from group IV nanoparticles materials," *United States Patent and Trademark Office*, 2007.
- [52] I. D. Sharp, Q. Xu, C. W. Yuan, J. W. B. J. W. Ager, III, D. C. Chrzan, and E. E. Haller, "Kinetics of visible light photo-oxidation of ge nanocrystals: Theory and in situ measurement," *Applied Physics Letters*, vol. 90, no. 16, p. 163118, 2007. [Online]. Available: <http://link.aip.org/link/?APL/90/163118/1>
- [53] D. Jishiashvili, Z. Shiolashvili, V. Gobronidze, and I. Nakhutsrishvili, "A study of solid phase reactions at the Ge-GeO₂ interface," in *Advanced Packaging Materials, 2002. Proceedings. 2002 8th International Symposium on*, 2002, pp. 112–115.

- [54] Y. Fukuda, T. Ueno, and S. Hirono, "Electrical behavior of germanium oxide/germanium interface prepared by electron-cyclotron-resonance plasma oxidation in capacitance and conductance measurements," *Japanese Journal of Applied Physics*, vol. 44, no. 11, pp. 7928–7930, 2005.
- [55] D. Schmeisser, R. D. Schnell, A. Bogen, F. J. Himpsel, D. Rieger, G. Landgren, and J. F. Morar, "Surface oxidation states of germanium," *Surface science*, vol. 172, no. 2, pp. 455–465, 1986.
- [56] T. Franzl, D. Koktysh, T. Klar, A. Rogach, J. Feldmann, and N. Gaponik, "Fast energy transfer in layer-by-layer assembled CdTe nanocrystal bilayers," *Applied Physics Letters*, vol. 84, p. 2904, 2004.
- [57] J. Jasinski, V. Leppert, S. Lam, G. Gibson, K. Nauka, C. Yang, and Z. Zhou, "Rapid oxidation of InP nanoparticles in air," *Solid State Communications*, vol. 141, no. 11, pp. 624–627, 2007.
- [58] I. D. Sharp, Q. Xu, C. Y. Liao, D. O. Yi, J. W. Beeman, Z. Liliental-Weber, K. M. Yu, D. N. Zakharov, J. W. Ager, III, D. C. Chrzan, and E. E. Haller, "Stable, freestanding ge nanocrystals," *Journal of Applied Physics*, vol. 97, no. 12, p. 124316, 2005. [Online]. Available: <http://link.aip.org/link/?JAP/97/124316/1>
- [59] S. Han, W. Ashurst, C. Carraro, and R. Maboudian, "Formation of alkanethiol monolayer on Ge (111)," *J. Am. Chem. Soc.*, vol. 123, no. 10, pp. 2422–2425, 2001.
- [60] A. Nilsson, L. Pettersson, and J. Nørskov, *Chemical bonding at surfaces and interfaces*. Elsevier Science, 2008.
- [61] D. Lide, "1996 CRC Handbook of Chemistry and Physics," *Boca Raton, FL: Chemical Rubber Company*, 1996.
- [62] J. Aldana, Y. Wang, and X. Peng, "Photochemical instability of CdSe nanocrystals coated by hydrophilic thiols," *J. Am. Chem. Soc.*, vol. 123, no. 36, pp. 8844–8850, 2001.
- [63] R. S. Tanke, S. M. Kauzlarich, T. E. Patten, K. A. Pettigrew, D. L. Murphy, M. E. Thompson, and H. W. H. Lee, "Synthesis of germanium nanoclusters with irreversibly attached functional groups: Acetals, alcohols, esters, and polymers," *Chemistry of Materials*, vol. 15, no. 8, pp. 1682–1689, 2003.
- [64] D. Lee, J. Pietryga, I. Robel, D. Werder, R. Schaller, and V. Klimov, "Colloidal synthesis of infrared-emitting germanium nanocrystals," *J. Am. Chem. Soc.*, vol. 131, no. 10, pp. 3436–3437, 2009.

-
- [65] J. Cheng and R. Xu, "Syntheses and characterization of two novel germanium dioxide frameworks with occluded ethylenediamine (EDA) and 1, 3-propylenediamine (1, 3-PDA)," *Journal of the Chemical Society, Chemical Communications*, vol. 1991, no. 7, pp. 483–485, 1991.
- [66] K. Williams and R. Muller, "Etch rates for micromachining processing," *Journal of Microelectromechanical Systems*, vol. 5, no. 4, pp. 256–269, 1996.
- [67] J. Sun and S. Simon, "The melting behavior of aluminum nanoparticles," *Thermochimica Acta*, vol. 463, no. 1-2, pp. 32–40, 2007.
- [68] H. Farrell and C. Van Siclen, "Binding energy, vapor pressure, and melting point of semiconductor nanoparticles," *Journal of Vacuum Science & Technology B: Microelectronics and Nanometer Structures*, vol. 25, p. 1441, 2007.

Appendix A

Immobilization of Enzymes in Chitosan

A.1 Introduction

At the micro- and nanoscale, chitosan is a great bioscaffold due to a robust chemical structure with high concentration of primary amino groups ($-\text{NH}_2$) for ionic or covalent bonding binding of biomolecules (e.g. DNA and proteins). Additionally, chitosan is soluble in weak acids and forms a hydrogel, making it an enticing material to work with for microfabrication. By using chitosan and chitin as the main structural material and its hydrogel characteristics and functionalizations, as it is used in nature, a wide variety of biosensors can result.

Table A.1 shows just a few relevant sensors that could be realized using proteins immobilized in patterned chitosan microstructures [11]. The survival of a model enzyme/substrate system in the chitosan matrix during spin casting and lithographic patterning was explored.

Existing methods for patterning hydrogels with possibility of enzyme functionalization include soft lithography, electrodeposition, and photolithography with photocrosslinkable chitosan. Soft lithography methods, such as the nanoimprinting method presented by Cheng *et al.* [29], are inexpensive, simple, and provide excellent resolution; however, the stamps are difficult to align to the substrate [30], require a uniform surface for efficient pattern transfer, and often require addition of a material plasticizer to maintain feature shapes [31]. Electrodeposition of chitosan has been demonstrated by Wu *et al.* [33]; however, it requires either a conductive substrate or a patterned electrode for deposition and can have dramatic uniformity issues due to variations in the electric field near the deposition surface. Finally, Karp *et al.* demonstrated a photocrosslinkable chitosan process for directing growth for cardiac fibroblasts, cardiomyocytes, and osteoblasts (SAOS-2). This process, while simple

Table A.1: Potential biosensor applications and their respective enzyme/substrate combinations [11]

Enzyme	Substrate	Application
Alcohol oxidase	Ethanol	Determination of Ethanol Concentration
Glucose oxidase	Glucose	Determination of Glucose Concentration (food, medical diagnosis)
Creatinine deaminase	Creatine	Determination of Creatinine
Urease	Urea	Determination of Urea
Putriscene oxidase	Putriscene	Determination of Meat Freshness
Xanthine oxidase	Xanthine	Determination of Fish Freshness

and inexpensive, suffers from poor feature resolutions around $100\ \mu\text{m}$ and reduces the number of functional groups available to bind biomolecules into the matrix [34].

As mentioned in Chapter 2, polysaccharide patterning techniques accomplished in solution have poor feature resolution and film uniformity; thus, a dry patterning technique was needed to overcome these limitations. Swelling and contraction due to the movement of solvent as well as the increased film thicknesses during optical lithography contribute dramatically to the reduction in feature resolution. Photolithographic patterning of dried polysaccharide films, such as chitosan, overcomes these issues by eliminating the solvent during the patterning step. A method for retaining bulk enzyme functionalization while patterning was also required. In addition, dry patterning of polysaccharide thin films enables multi-layer devices where each layer can be uniquely formulated and functionalized.

A.2 Experiments

A.2.1 Chitosan solution preparation

Stock solutions of 3.5% w/v medium molecular weight chitosan (Sigma Aldrich, St. Louis, MO) in a 1 : 100 mixture of acetic acid (HAc) and deionized water (DI) are prepared with a final pH ~ 5 . The solutions are then mixed on a hot plate at 95°C for six to eight hours and triple filtered using air actuated syringes at 550 kPa (80 psi) with $25\ \mu\text{m}$, $10\ \mu\text{m}$, $5\ \mu\text{m}$, and $2.5\ \mu\text{m}$ Durapore filters (Millipore, Billerica, MA). Air bubbles in the solution are then removed using centrifugation at 27,500 g for twenty minutes.

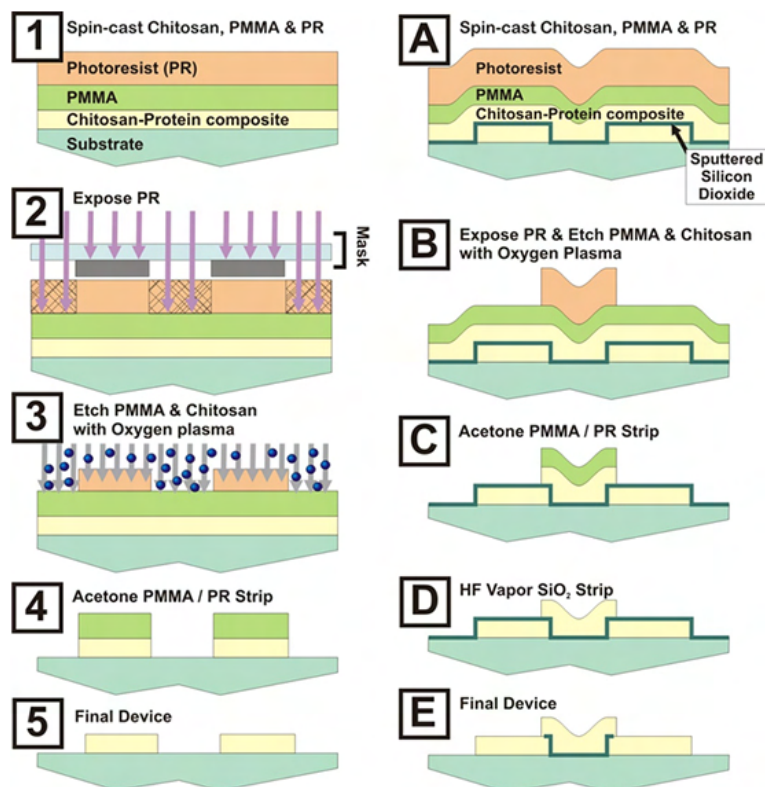


Figure A.1: (A) Single layer chitosan-protein patterning, and (B) Multi-layer chitosan-protein patterning.

A 10 mg/mL stock solution of enzyme is prepared using β -D-galactosidase supplied from Sigma Aldrich. This solution is filtered once using a Whatman 0.22 μ m syringe filter and mixed 1:10 into a stock chitosan solution. The solution is then thoroughly mixed and degassed using an ultrasonic bath and spin cast promptly after mixing.

Fluorescein di- β -D-galactopyranoside (FDG) from Axxora is mixed into a 0.5 mM solution and a droplet of 1 - 10 μ L is applied to the sample using a micro-pipetter. A negative control for fluorescence is performed using a droplet of 0.5 mM FDG on a clean microscope slide and a positive control is performed with a droplet of 0.5 mM FDG mixed with a droplet of the stock enzyme solution.

A.2.2 Single Layer Fabrication Process

Single layer lithography of chitosan-protein composite films, shown in Figure A.1A, starts with spin-casting the viscous solution (\sim 600 cP) onto silicon and pyrex wafer dies at speeds between 2000 - 3000 rpm to achieve thicknesses between 200 nm and 1.5 μ m. A five minute bake at 70°C or 90°C dries the chitosan film. PMMA (950

Table A.2: Selected oxygen plasma etch rates. All etch rates were determined by measuring film thicknesses before and after a 30 sec etch.

Etch Conditions		Etch Rates (nm/sec)		
Power (W)	O ₂ (sccm)	OCG-825 PR	MicoChem C5 PMMA	3.5 % w/v Chitosan
30	50	-	-	168
40	50	-	-	201
50	50	-	-	250
70	50	-	-	330
50	55	111	180	-
70	55	145	311	-
100	55	170	343	-
50	65	117	166	-
70	65	153	231	-
100	65	224	372	-

PMMA C5 Resist from MicroChem, Newton, MA) is then spin-cast on the wafer at 2000 rpm for ten seconds with a 200 rpm/sec ramp rate and is then baked again for five minutes at either 70°C or 90°C. The PMMA layer protects the chitosan-protein composite films from the photoresist developer solution. Next, a 2 μ m OCG-825 G-line Photoresist is spun at 2200 rpm for thirty seconds, baked for sixty seconds at either 70°C or 90°C, patterned using projection printing and developed using OCG-934 2:1 photoresist developer. A hard bake is performed for ten minutes at either 70°C or 90°C. The dies are then etched with oxygen plasma in a PlasmaTherm parallel plate RIE system with an RF power between 50 and 150 W, an oxygen flow rate between 55 and 65 sccm and a base pressure less than 11 mTorr. Etch times are determined based on the thicknesses of the chitosan-protein composite film and the PMMA layer. Table A.2 indicates the measured etch rates for a range of materials and etching conditions. The remaining photoresist and PMMA is stripped using room temperature acetone and is followed by a deionized water rinse. Nitrogen was used to dry the samples.

A minimum line width of 2 μ m and less than 15 % variation in thickness across the wafer are achieved with this process.

A.2.3 Multi- Layer Fabrication Process

Multi-layer chitosan patterning begins by sputtering a 25 to 100 nm silicon dioxide (SiO₂) stopping layer on top of a chitosan film created with the single layer process. SiO₂ is sputtered using a Randex thin film deposition system with 100 W of applied RF power and 44 sccm of 90 % argon / 10 % oxygen. A deposition rate of SiO₂ of 4.2 Å/min is typical. Next, the single layer patterning process is repeated on top of

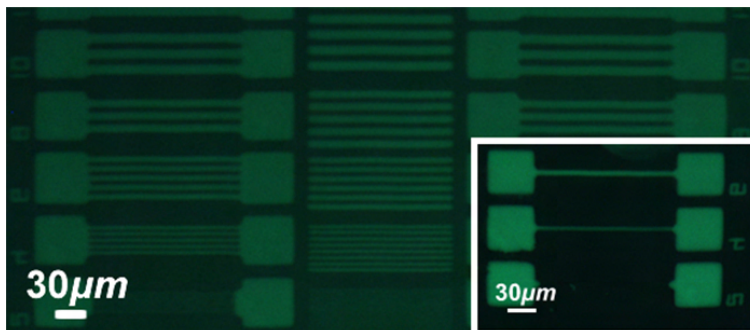


Figure A.2: Patterned chitosan structures with immobilized β -Galactosidase treated with fluorescein di- β -D-Galactosidase (FDG) viewed under a fluorescent microscope.

the SiO₂ stopping layer. A brief thirty to sixty second HF vapor etch is performed to remove the surface SiO₂ layer (100 nm/min) [66]. An overview of the multi-layer fabrication process is given in Figure A.1B.

A.2.4 Sample Imaging and Metrology

Film thicknesses and line widths are characterized using an KLA-Tencor Alpha Step IQ profilometer and a NanoSpec/AFT Model 3000 film thickness measurement system. Activity of the immobilized β -D-Galactosidase is observed qualitatively using a Zeiss AxioImager M1 fluorescence microscope, a FITC filter set and a QImaging 5MP MicroPublisher camera.

A.3 Results and Discussion

A.3.1 Single layer

The viability of enzymes in the chitosan after lithography is determined by an example assay of immobilized β -D-galactosidase and an externally applied solution of fluorescein di- β -D-galactopyranoside (FDG). The hydrogel features swelled taking up the solution and substrate; thus, allowing enzyme activity. In the example assay, β -D-galactosidase cleaves the fluorescein from the FDG increasing its fluorescence signal at a peak of 514nm when excited by 490 nm. Significant fluorescence of the features was observed when using a GFP filter set, as shown in Figure A.2. The chitosan features remained bound to the silicon substrate and did not delaminate when hydrated. All features, including the smallest line features at 2 μ m in width, retained activity.

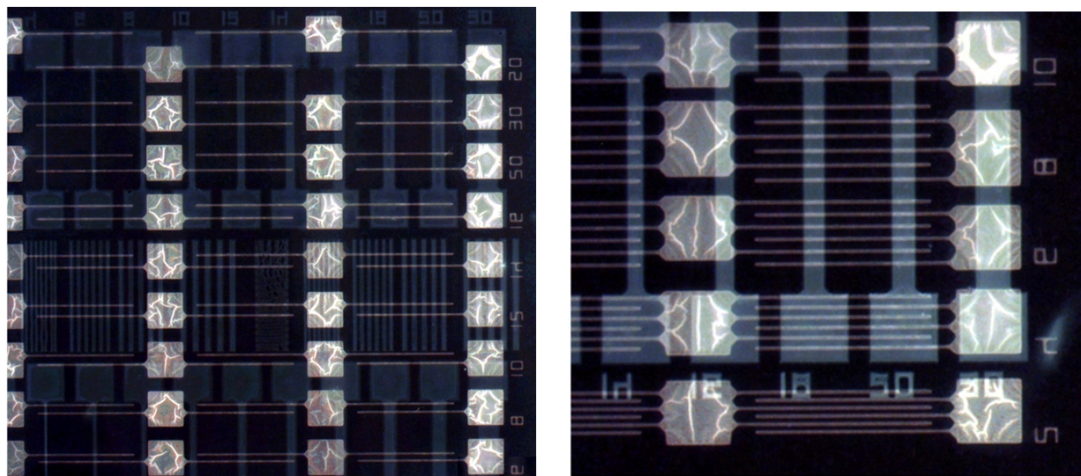


Figure A.3: Multi-layer stack of patterned chitosan with immobilized enzymes in the bottom layer taken at 5x (above left) and closer up at 20x (above right) magnification. Images taken with fluorescent microscope with FITC filter set where bright white fluorescing features are in the bottom layer with immobilized enzymes and the lower intensity, autofluorescing features are in the top layer. Note: Auto-leveling applied to images for purposes of clarity.

A.3.2 Multi-layer

The primary concerns for multi-layer processing are protection of the lower layer and effective adhesion of the top layer. Patterning of the top layer of chitosan requires an over etch to attain high quality feature definition; thus, an etch stop is necessary to protect the underlying layer. The presence of enzymes and polymers requires a very low thermal budget for the etch stop with temperatures below 90°C; thus, sputter deposited silicon dioxide is chosen as the etch stop. In addition, silicon dioxide can be removed using a HF vapor etch. Removing the silicon dioxide etch stop exposes the underlying layer allowing external chemicals like FDG to be applied to it for assays. A ten minute oxygen plasma etch performed at 70 W showed no measureable changes in silicon dioxide thickness and completely protected an underlying layer of chitosan. Thus, a thin layer of sputtered silicon dioxide is used as the etch stop due to its high oxygen plasma resistance and to minimize exposure to HF vapor during the etch stop removal step.

Two layers are patterned to test the multi-layer fabrication process. The first layer is an 800 nm chitosan film with immobilized enzyme on a silicon surface. A 65 nm sputtered silicon dioxide layer is then deposited on top of the first layer of chitosan to serve as the etch stop for second layer. The second layer is a 1.5 μm chitosan film. The same sets of features are patterned for both layers, with the second layer rotated 90°. The resulting multi-layer pattern is shown in Figure A.3.

The viability of the proteins in the first layer is then tested using the same protocol as used for the single layer. The strong fluorescence from the features with immobilized enzymes shown in Figure A.3 (bright white features) showed that the enzymes survive the processing. The chitosan top layer shows some autofluorescence; however, this intensity is noticeably lower than that of the functionalized, 1st layer. The wrinkling shown above the white pads of the features in the 1st layer is believed to be caused by interaction between the swelling hydrogel and residual silicon dioxide from the etch stop.

A.4 Conclusion

The advantages of enzymes immobilized in chitosan thin films are viability for extended periods of time and suspension in a robust, biocompatible matrix. The high-resolution, enzyme-compatible patterning process enabled the creation of multi-layer biologically-active devices. By patterning stacks with each layer distinctly functionalized, unlike surface functionalized structures with only a single functionalization, the process enabled devices capable of multi-stage assays with higher densities of enzymes for analysis. Overall, given that the amount of analyte is limited, this allows greater sensitivity and versatility. Also, these devices can be fabricated from a greater variety of materials. The current silicon dioxide layer, while providing adequate protection during patterning, introduces stress issues. While the wrinkling due to stress shown in Figure A.3 did not affect the viability of the enzymes in the first layer, a more elastic etch stop layer would be preferable to prevent delamination. With the multi-layer process, high density assays can increase throughput as well as enable a novel method to examine protein-protein interactions.

Appendix B

Supplemental Data

B.1 Nanoparticle Data

B.1.1 X-ray Absorption Spectra (XAS)

All samples for XAS imaging were casted on 100 nm thick silicon nitride windows and run at ALS Beamline 6.3.2. Unfortunately ALS was being run on two bunch mode so beampower was about a fifth of normal. Therefore while the basic data was collected and correlated with known literature, data was not as good as other data generated by other soft x-ray techniques such as XPS. Therefore further interpretation of the below data was not performed.

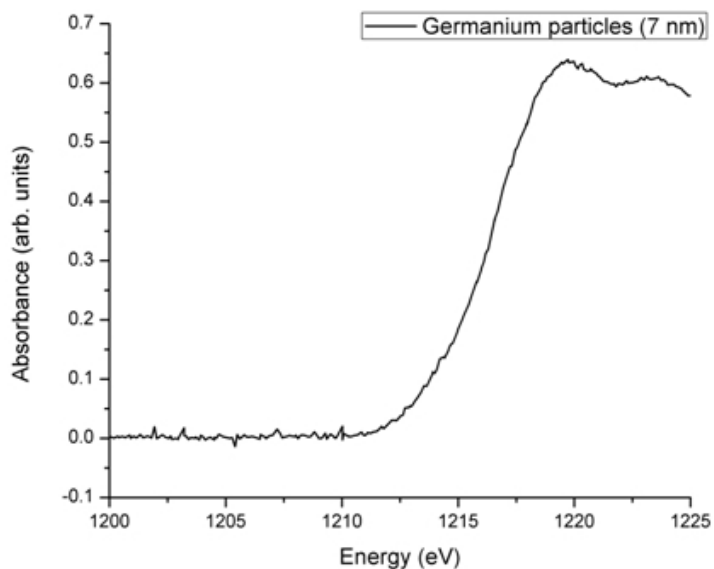


Figure B.1: XAS (pre-edge, XANES, EXAFS regions for 7 nm Ge particles)

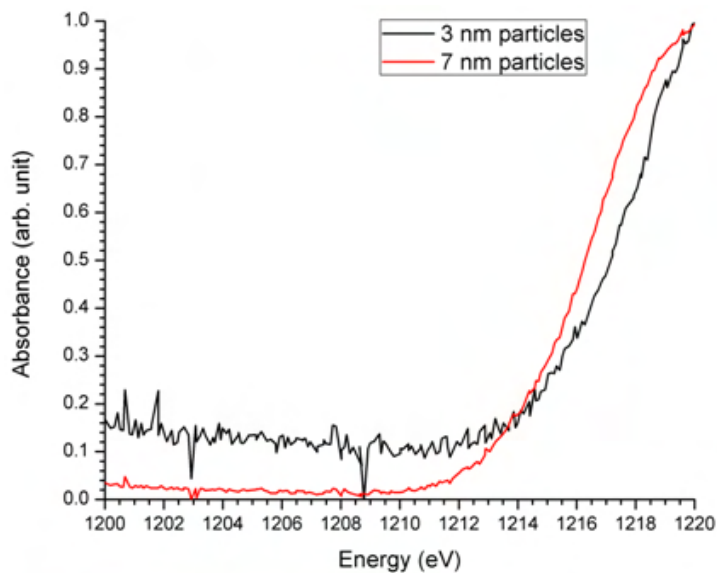


Figure B.2: XANES and pre-edge regions for 3 and 7 nm particles. 3 nm particles blue-shifted in plot.

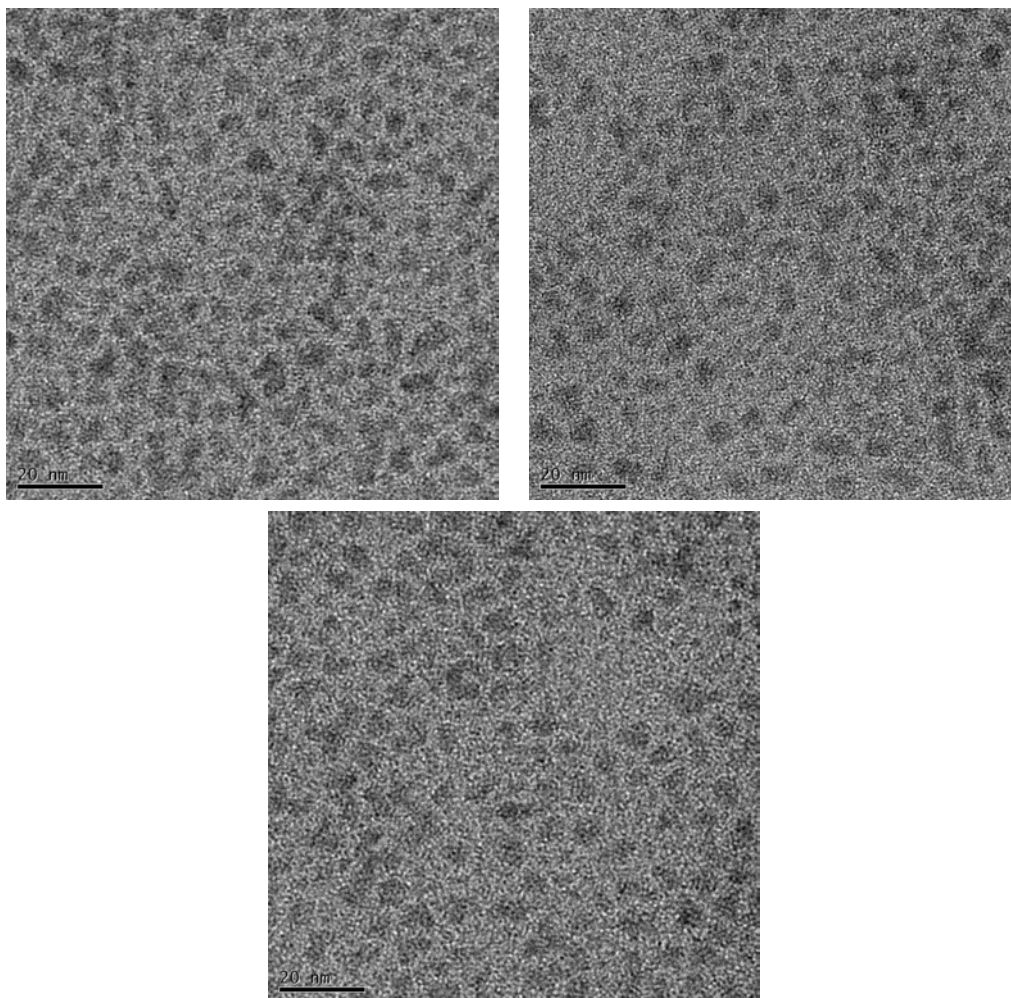


Figure B.3: TEM images of the post-functionalization ODE Ge nanoparticles.

B.1.2 Post-functionalization TEM

Other TEM images of the 5 nm germanium nanoparticles synthesized using the post-functionalization protocol can be seen in Figure B.3. These images combined with the image shown earlier in the Chapter 3 were used to calculate the size and size distribution of the nanoparticles.

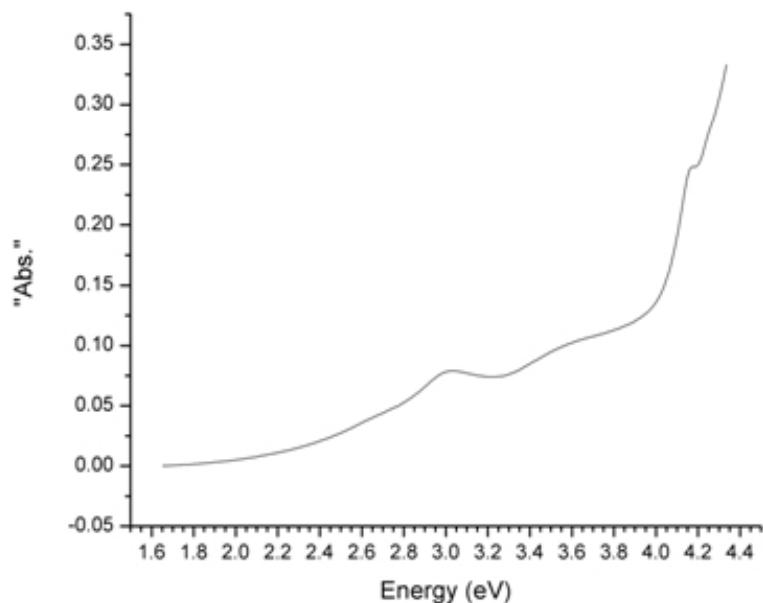


Figure B.4: UV/VIS spectrum of the 7 nm germanium nanoparticles synthesized using the initial protocol.

B.1.3 UV/VIS spectrum

Unfortunately, the visible spectrum is not sufficient to show the strongest of the absorption bands (1Se-1Sh) for the germanium nanoparticles. Germanium's first absorption band should be a little larger than 0.67 eV. A secondary absorption band is seen in Figure B.4.

B.1.4 General properties of nanoparticles

A large majority of quantum effects are due to confinement from the size and surface area to volume ratio. Some of these properties are seen in Table B.1.

Melting point depression for sintering of nanoparticles is an important and highly utilized property of nanoparticles. This property is utilized for metal nanoparticle inks where their low melting temperature is used for low temperature formation of interconnects for circuits. Innovalight, Inc. is utilizing this property as well for their silicon nanoparticle inks. However, as semiconductors have a weaker melting point depression than metal nanoparticles, the melting temperature is still very high. The general relation for the melting point depression of metal nanoparticles has been defined by the Gibbs-Thomson relation:

$$T_M = T_{MB} \left(1 - \frac{4\sigma_{sl}}{H_f \rho_s d} \right) \quad (\text{B.1})$$

Table B.1: General size, area and volume properties of nanoparticles. Assumption of atomic diameter of 5Å.

Particle diameter (nm)	Number of atoms	Fraction at surface (%)	Surface-to-volume ratio
0.5	1	100	6:1
1.0	8	100	3:1
2.0	64	99	1.5:1
5.0	1,000	50	1:1.67
10.0	8,000	25	1:3.33
20.0	64,000	12	1:6.67

where T_M is the melting point of the nanoparticle, T_{MB} is the bulk melting point, σ_{sl} the solid-liquid interface energy, H_f the bulk heat of fusion, ρ_s the density of the solid and d the diameter of the nanoparticle [67]. The general relation for the melting point depression of semiconductor nanoparticles is:

$$T = T_B \left(1 - \left(\frac{\kappa}{d}\right)^2\right) \quad (\text{B.2})$$

where T is the melting point of the nanoparticle, T_B is the bulk melting point of the substance, κ a fitting parameter defined by the substance and d the diameter of the nanoparticle [68]. As can be seen, there is a quadratic relation between the nanoparticle size and its melting temperature for semiconductors which greatly reduces the melting point depression.

B.1.5 Cadmium Sulfide (CdS) Nanoparticles in Chitosan

Early on in the research while searching for methods for synthesizing nanoparticles in a polymer matrix, cadmium sulfide nanoparticle synthesis was performed. These particles were synthesized in chitosan solutions through by first mixing various concentrations of cadmium acetate ($\text{Cd}(\text{Ac})_2$) with 3% w/v chitosan and stirring for fifteen minutes at room temperature. This functionalized the chitosan with Cd^{2+} ions. This chitosan-cadmium solution was then drop-casted onto a substrate such as silicon. Then 1% sodium sulfide (NaS) solution was added and allowed to react for ten seconds 100 mM sodium chloride (NaCl) solution was used to wash the substrate. This removed unreacted NaS and reacted byproducts. The result was CdS nanoparticles between 10-100 nm in diameter depending on the original precursor concentrations. This method demonstrated the feasibility of creating chitosan-nanoparticle nanocomposites. However, due to the formation mechanism, the particle size, distribution and monodispersity was difficult to control. Also, oxidation was another issue which prevented high quality nanocrystals from being formed. Also, due to the small exciton

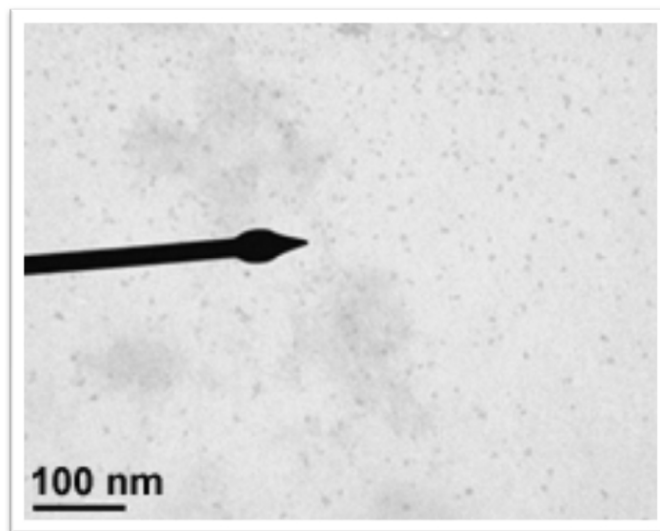


Figure B.5: Approximately 10 nm CdS nanoparticles bonded into a chitosan film.

Bohr radius and larger bandgap of CdS, it was not chosen as the nanoparticle to be used for the PNTFT.